Transition to turbulence in circular expansion pipe flow

Kamal Selvam

Normandie Université

THESE

Pour obtenir le diplôme de doctorat

Spécialité : Dynamique des Fluides et Energétique

Préparée au sein de l'Université du Havre

Transition to turbulence in circular expansion pipe flow

Présentée et soutenue par
Kamal SELVAM

Thèse soutenue publiquement le 07/10/2016 devant le jury composé de		
M. Jean-Christophe ROBINET	Professeur, Art et Métier ParisTech, Paris	Rapporteur
M. Ashley P. WILLIS	Lecturer, University of Sheffield, UK	Rapporteur
M. Dwight BARKLEY	Professor, University of Warwick, UK	Examinateur
M. Innocent MUTABAZI	Professeur, Université du Havre, France	Examinateur
M. Christoph EGBERS	Professor, BTU Cottbus-Senftenberg, Germany	Examinateur
M. Arnaud PRIGENT	MDC, Université du Havre, France	Examinateur
M. Jorge PEIXINHO	CR CNRS, HDR, Université du Havre, France	Directeur de thèse

Thèse dirigée par Jorge PEIXINHO, Laboratoire Ondes Milieux Complexes, CNRS UMR 6294

UNIVERSITÉ LE HAVRE — SPMI ECOLE DOCTORALE — RÉGION NORMANDIE — CRIANN Centre Régional Informatique et d'Applications Numériques de Normandie — cnrs

Doubt everything, find your own light
- Gautama Buddha

Acknowledgements

Foremost, I would like to express my sincere gratitude to my advisor Jorge Peixinho for his continuous support, patience, motivation and enthusiasm during my thesis. His guidance helped me in all the time of research and writing of this thesis. All these years, I have learned a lot from him. I have never seen someone so organized like him and I think I have imparted few of his qualities. Apart from science, he has been well-wisher to me. I would also like to thank Ashley Willis for his down to earth behaviour, wonderful spectral code, fruitful discussions and guidance.

In this moment, I am grateful to Innocent Mutabazi who gave his immense support during my thesis. His great level of charisma has inspired me a lot. My sincere thanks to Jose Eduardo Wesfreid for his scientific question, which helped me to take the thesis forward. I certainly appreciate Arnaud Prigent and Olivier Crumeyrolle for technical discussions.

I thank Paul Fischer for his initial support and his code. I am also greatly thankful to Jean-Christophe Loiseau for his support, advice and also for his very friendly approach towards me. My sincere thanks also goes to Yohann Duguet for his Focus on Fluids paper, which has expanded my research to a new level.

Besides, I also thank Emir Öngüner, Amir Sharirpour, El-Sayed Zanoun and Christoph Egbers for their coordination and collaboration during the experimental campaign at Germany.

I also very thankful to Joanna Eid and Marie-Charlotte Renoult for the level of their personal support and advice they gave me. I thank Changwoo Kang for deep discussions we had about direct numerical simulations.

I thank my fellow lab mates in for the stimulating discussions and for all the fun we have had in the last four years. Also I thank my friends in the following institution Laboratoire Ondes Millieux Complexes. In particular, I would like to mention Abdessammad Talioua, Floriant Colboc for the amount of coffee breaks and experimental discussions we had.

It was people like David Fabre, Jacques Magnaudet, Laurent Joly, Yannick Bury, Olivier Marquet, Joel Tchoufag who motivated me to take up this thesis, I would like to acknowledge them here.

Further, I am much obliged to mention my college professors Manishankar and Senthil Kumar for imparting in me the knowledge of fluid dynamics. I would not forget to remember my high school physics teacher Natesan sir and Vijaya mam for helping me identify the potential inside me and inspiring me.

I am greatly indebted to thank Suganyadevi Samuel, Vijai Balakrishnan, Alexandre Paes De Carvalho, Navnina Bhatia, Vishnu Viswanathan and Joseph Mariannaretty who steered and supported me during the stay in France.

Similarly, I am grateful to Sudharsan Thiruvenkadam, Sridhar Thirnavukarasu, Saravanan Thiruchelvam, Robin Richard Rajan, Sachin Damianose, Sirajudeen Salaludeen.

Along side, I would like to mention my college friends who were always encouraging me for taking fluid dynamics as a subject and constantly making fun of my weirdness: Raiz Ahamed, Ritesh Sharma, Vignesh Gandhiram, Mahesh Kumar Murali, Srikanth Murugesan, Vigneshwara Pandian, Shanmuga Sundaram, Shri Ram, Jerish Anton, Vignesh Kuppuraj, Siva Srinivasan, Pon Karthik, Shanmuka Sai Krishna, Sylvester Amaladoss, Kishore KM, Bala Krishnan and Ester Jemi sandiag

My deepest gratitude to my Aero J college mates and my long time school friends Dinesh Raman, Kaushik Venkatraman, Arvind Vignesh Parthasarathy , Arun sathyanarayanan, Arun Ram Prasad, Ashwin Kumar, Shanmuga Velan for helping me stay strong through thick and thin.

I am ineffably grateful to and fortunate enough to get constant love, support and encouragement from my parents, my uncle Giridharan and my brother Vikram Selvam, without whom all this would not have been possible.

Contents

List of Figures

Chapter 1

Introduction

The science of fluid dynamics has been focus of researcher's worldwide for many years, because of its complex nature. In order to understand the behaviour of fluids, theoretical and experimental studies are conducted but with limitations. Analysis of big systems like waves in ocean or turbulence in atmosphere are very difficult because of its size and complexity. Building experiments or computations are very difficult to scale such huge problems. Solution to this, is to construct simple models that could be easily built inside a laboratory, such that the physics behind it can be well understood. Fluid flow through simple geometries like circular pipe or between two flat plates, exhibit two types of behaviour which depends on velocity and the viscosity of the fluid: laminar flow or turbulent flow. Laminar flow is characterised by streamlines moving parallel to each other and each of which has a constant velocity but is in motion relative to its neighbouring layers. It has high momentum diffusion and low momentum convection, whereas the turbulent regime is characterised by chaotic motion of the fluid particle, along with eddies and high fluctuations. In case of turbulent flow, it exhibits low momentum diffusion and high momentum convection, which helps in mixing.

Passage of fluid from laminar to turbulent regime is called "*Transition to Turbulence*". There are two kinds of flows, ones, which are subjected to volume force such as temperature and gravity, and those, which are dominated by shear. The *Taylor-Couette* (fluid in between two rotating cylinder) is a good example of first kind of flow, as the rotating speed of the cylinder is increased, linear instabilities occur. These instabilities changes the topology of the fluid, but stays very close to base state. The process of moving from one state to another is known as *bifurcation*. When the rotating speed of the cylinder is increased further, successive bifurcations occur inside the flow that makes it more disordered in space and time and finally reaching chaos. Occurrence of successive bifurcations, which moves the fluid system from laminar to turbulent is called *super-critical* transition to turbulence. In case of super-critical transitions, linear stability theory can be used to predict the bifurcation points. Shear dominated flows, such as, *plane Couette flow* or Poisueille flow, bifurcations occurs at much lower values of the control parameter than the linear instability threshold. In case of *pipe Poisueille flow*, there is no linear instability at all. The reason for such earlier transition is due to presence of finite amplitude disturbance that gets amplified due to convective instability mechanism. The other major difference is that, the bifurcated flow is very different from the base flow and has a high level of disorder. Linear stability theory fails to predict this transition with accuracy. These transitions, often called as *sub-critical* transition to turbulence, are major focus here. In sub-critical transition, the coexistence of several locally stable states at a given value of the control parameter is possible and a hysteretic behaviour as the control parameter is varied. One way to understand the process of transition is to look from system dynamics point of view. Consider an equilibrium system in which the flow is time independent and spatially uniform, instabilities drive the flow away from the equilibrium point. The corresponding system then starts behaving in an unexpected manner due to the competition between the stabilising and destabilising forces.

Hydrodynamic stability analysis is a method to study the behaviour of flow subjected to an infinitesimal disturbances. According to linear stability theory, pipe flows are always stable, even at infinite Reynolds number. Whereas, in 1883, *Reynolds* [1] conducted the famous experiment, to study the transition of laminar flow to turbulence in a straight pipe. He interpreted that the transition was due to presence of disturbance in the pipe that aids the flow to move from laminar regime to turbulent regime. The amount of noise in the system has direct effect on the transition of turbulence. He found that, by carefully controlling the experiment, the transition Reynolds number could be delayed. This ambiguity between the theory and experiments has left researcher to invent new theoretical methods

like weakly non-linear analysis, transient growth analysis to study instabilities in depth. These methods are computationally very costly, but with the advent of modern super computational facility, it is easier to perform Direct Numerical Simulation (DNS). Recently, experiments methods like Particle Image Velocimetry has helped researchers to analysis the system more rigorously.

In this chapter, initially the theory behind pipe flow is discussed along with brief summary of numerical and experimental results obtained so far in the literature. Second part of the chapter is dedicated to expansion pipe flows. In the third part, we discuss global stability analysis, transient growth analysis, numerical simulations, experiments and some of the unanswered questions. Finally, the outline of the thesis is given for the convenience of the reader.

1.1 Navier–Stokes Equation

In early 1800's Claude Navier and George Gabriel Stokes derived the partial differential equations that govern the dynamics of fluid known as the famous Navier-Stokes (NS) equations. Using the principle of mass and momentum conservation, the incompressible NS equation can be derived in a non-dimensionalized form as:

$$\begin{aligned} \frac{\partial \mathbf{u}}{\partial t} + \mathbf{u}\cdot\nabla\mathbf{u} &= -\nabla p + \frac{1}{Re}\Delta\mathbf{u} + \mathbf{f}, \\ \nabla\cdot\mathbf{u} &= 0. \end{aligned} \tag{1.1}$$

Where $\mathbf{u}$ is the velocity vector and p is the pressure. The external force is denoted by $\mathbf{f}$. Re is a dimensionless quantity called as Reynolds number. It is defined as $Re = UL/\nu$, where U is the characteristic velocity $[m/s]$ (mean velocity of the fluid), L the characteristic linear dimension $[m]$, and ν the kinematic viscosity $[m^2/s]$. It acts as a control parameter to the system that drives the flow. The parameter Re can be understood as a measure that compares the applied shear that is disturbing the flow to that of viscous dissipation that is stabilising the flow. A viscous time scale can be obtained as $\tau_\nu = L^2/\nu$ and a shear time scale as $\tau_s = L/U$, using both the time scale, Reynolds number can be again redefined as $Re = \tau_\nu/\tau_s$. When ratio between the τ_ν and τ_s is small, the viscous dissipation, damps out small fluctuations in the velocity field and stabilise it. On the other hand, when the ratio is larger, viscosity has less effect on the flow to damp the oscillations due to shear, which ultimately leads to transition.

The NS equations are non-linear equations, which is studied by mathematician and physicist for its wide range of application. It is well known that in two space dimensions, (1.1) has a unique solution for all times under some restrictions on the initial condition. In three space dimensions, there are no solutions, if they do, they are not smooth enough. It is one of the millennium prize problems in mathematics, to prove that solutions of the three dimensional incompressible Navier-Stokes equations always exist.

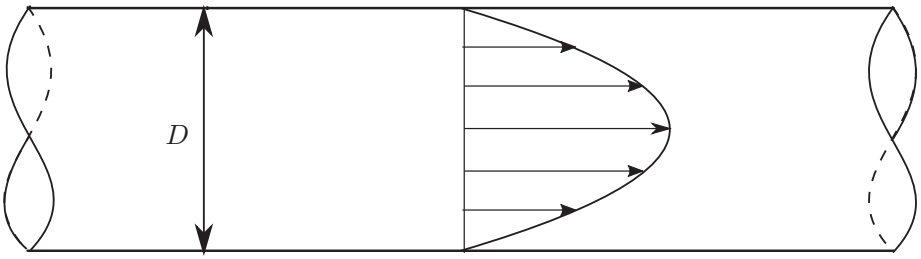

Figure 1.1: Schematic diagram of Hagen-Poiseuille flow in a infinitely long pipe

1.2 Constant diameter pipe flow

Pipe Poiseuille flow also known, as Hagen-Poiseuille flow is one of the classical wall bounded shear flows, to which analytic solutions of the Navier-Stokes equations exists. The flow is driven by a constant non-zero pressure gradient in the axial direction. The stationary solution to an infinite length pipe flow is a parabolic velocity profile, where the velocity only depends on the distance from the wall and the direction of the profile lies towards the negative pressure gradient. The stationary solution for pipe Poiseuille flow is given as:

$$\mathbf{U} = (1 - r^2)\mathbf{e}_z, \tag{1.2}$$

here r is the radius of the pipe. Figure 1.1 shows a schematic diagram of the pipe Poiseuille flow, which is parabolic. The Reynolds number for pipe flow is defined by $Re = UD/\nu$, where D is the pipe diameter U is the mean velocity. The simplest form of the pipe geometry has led researchers to study the flow behaviour extensively. However, there are lot of unknowns about the transition to turbulence due to the effect of perturbations.

1.2.1 Stability

Hydrodynamic stability analysis is a process to check if a flow is stable, when subjected to disturbance. The idea is to take a stationary flow and apply some disturbance to it and check the growth of this applied disturbance. Looking for the critical Re at which the flow becomes unstable, the type of disturbance are some of the questions that can be answered through stability analysis. Consider the flow velocity and pressure $(\mathbf{U}, P)$ that satisfies the equation (1.1), the effect of a disturbance, $\hat{\mathbf{u}}^0$, can be investigated by considering the perturbation equation. Let $(\hat{\mathbf{u}}, p)$ be the small deviation from the baseflow due to the disturbance. The deviated flow can be written as $(\mathbf{U} + \hat{\mathbf{u}}, \mathbf{P} + \hat{p})$ and it satisfies (1.1), subtracting the base flow and the perturbed flow yields the following equation:

$$\hat{\mathbf{u}}_t + (\hat{\mathbf{u}} \cdot \nabla)\hat{\mathbf{u}} + (U \cdot \nabla)\hat{\mathbf{u}} + (\hat{\mathbf{u}} \cdot \nabla)\mathbf{U} = \frac{1}{Re}\Delta\hat{\mathbf{u}} \tag{1.3}$$

$$\nabla \cdot \hat{\mathbf{u}} = 0 \tag{1.4}$$

$$\hat{\mathbf{u}}(\mathbf{x}, 0) = \hat{\mathbf{u}}^0 \tag{1.5}$$

A norm, is defined to measure the size of the perturbation in (1.5), which defines the stability of the base flow. Different kind of norms can be used according to problem. L^2 norm, which measures the kinetic energy of the perturbation is used in general. The baseflow is said to be stable to the disturbance, if the norm of the perturbations tends to zero as time increases. If the flow is stable to all the disturbance then it is called "globally stable". In most cases, the flow is only stable for the disturbance that are small enough, If the disturbance is larger than a critical value the flow becomes unstable. Such kind of stability, which depends on size of the perturbation, is called conditional stability. Re plays a vital role in the stability of the flow. At low Re, the flow might be globally stable but conditionally stable at higher Re. Some flow have a critical Reynolds number Re_c, beyond which the infinitesimal perturbation makes the flow unstable. The search for the Re_c, size, shape and the optimal perturbation is the most fundamental part of hydrodynamic stability. Stability of the flow can be determined by looking at the eigenvalue of the linearised equation of (1.5). The real part of the eigenvalue corresponds to growth rate and the imaginary corresponds to oscillation. If the flow is stable, the real part of the eigenvalue remains negative. Re_c is found when the real part of the eigenvalue becomes positive.

The critical Reynolds number for which plane Poiseuille flow becomes linearly unstable is at $Re_c > 5772$, when the so-called Tollmien Schlichting wave becomes linearly unstable. However, turbulence typically appears at much lower Reynolds numbers in reality. This discrepancy is due to the fact that full spectrum of NS equation (1.1) is not taken into consideration only the linearised equation (1.5) is considered, so finding the subcritical Reynolds number and the amplitude of perturbation is very difficult. The complexity comes when considering the case of pipe Poiseuille flow, which is linearly stable at all Re. However, experiments by Osborne Reynolds have shown that the flow loses its global stability $Re > 2000$, It signifies that any perturbation to the pipe at low Re, will be damped. He found that the perturbation inside the experiments leads to early transition. Laminar pipe flow up till $Re < 10^5$ can be achieved by carefully controlling the external noise in the experiments [2]. In case of pipe Poiseuille flow, where the linear stability analysis (1.5) fails to find an unstable eigenvalue, mathematicians have applied transient growth analysis [3]. According to transient growth analysis, the least stable eigenvalue (the eigenvalue close to zero) still have linear effects that may cause considerable initial growth of a perturbation. This is due to non-orthogonality of the eigenfunctions of the linearised Navier-Stokes operator. In case of pipe flow the non-linear (higher order) terms that are removed due to linearisation (1.5) creates the growth of perturbation that leads to transition to turbulence. One other way to study transition is to solve the full non-linear equation (1.1), which is nothing but DNS. Apart from DNS, many other numerical methods like Large Eddy simulation, in which large scales of the spectrum are solved using NS equation and the smaller scales are simulated using a mathematical model. Another simulation method is to use Reynolds Averaged Navier-Stokes method as it averages the whole spectrum as mentioned in its name, It has less computational cost, when compared to other methods. Using these tools, it is possible to look into the process of transition in a much-detailed way. In the following section, DNS results of pipe flow are discussed.

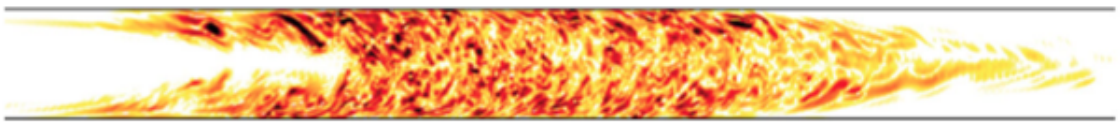

Figure 1.2: Axial vorticity plot showing a numerical puff evolution at Re=3000. Image taken from Duguet *et al.* 2010 [4]

1.2.2 Transition to turbulence

Since steady laminar pipe flow happens to be linearly stable for all Re, to trigger turbulence, it require a finite amplitude perturbation. DNS with edge state perturbation, have shown that there exists a whole range of Re, where the laminar flow and the turbulence can coexists and this regime is termed as transitional regime. Pipe flow in this transitional regime exhibits a quasi-stable localised turbulent "puff" state as well as a globally turbulent "slug" flow, they were detected experimentally [5] and numerically on periodic domains [4, 6–9]. It was shown that the finite amplitude required to trigger "puff" depend critically on its "shape" and "position". Researchers have used random disturbances [4, 6], impulsive perturbation [8] or obstacle disturbance [5] at the inlet of the pipe to study transition. The discovery of exact travelling wave solutions in wall-bounded shear flows, has made researchers speculate that the states lie inside the turbulent attractor and close to laminar-turbulent boundary edge [6]. A turbulent flow trajectory is said to move between these states, which depends upon the unstable direction of the travelling waves in phase space [6].

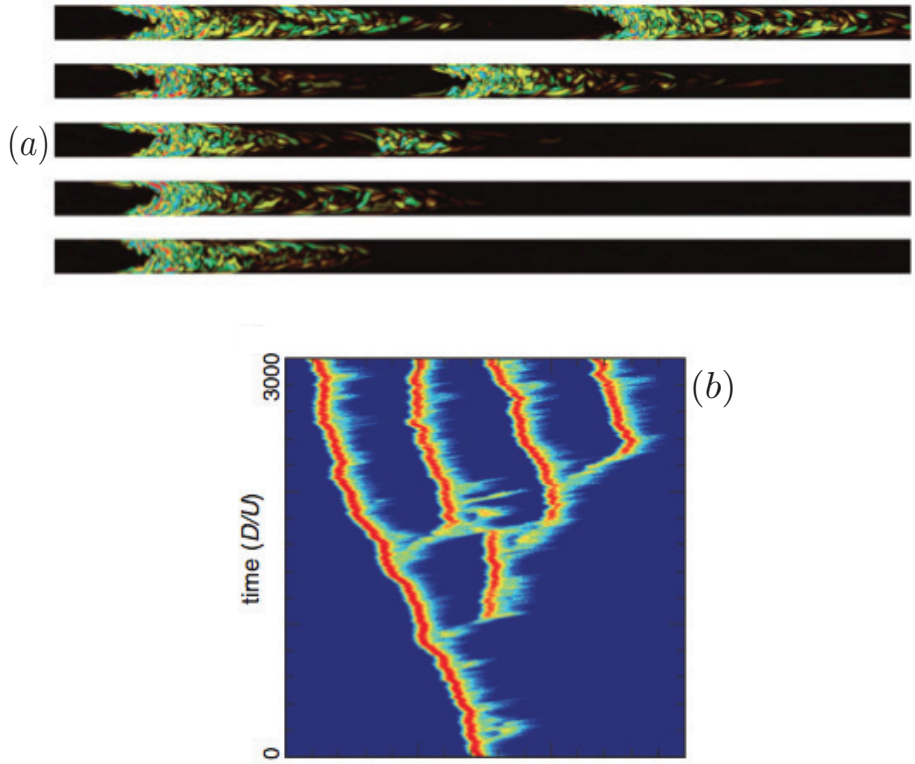

Figure 1.3: (a) Visualisation of puff splitting at Re = 2300 in a cross-sectional (x, y) plane, with red as positive and blue as negative streamwise vorticity on a linear scale and showing $75D$. At t = 0, Re is impulsively changed from 2200 to 2300. Snapshots (from bottom to top) were taken at $t = 500, 990, 1010, 1110$ and 1600. Once the puff extends far enough and the vorticity decays in its central section, a new puff emerges. (b) Spreading of turbulence in a numerical simulation. Space-time diagram was constructed from the center axis of the $150D$ long pipe. Images taken from Avila *et al.* 2010 [8]

The transitional regime, initially occupied by the “puff”, as Re increases, weakly turbulent puffs become growing turbulent slugs filled with small scale turbulence of regularly increasing length tending

to capture the whole pipe. It was shown that the length of the puff is statistically constant, which led to think that they are equilibrium states [5]. Structure of a puff as shown in figure 1.2 has a sharp leading edge and blunt tailing edge. Recent experimental and numerical studies have shown that, puffs might decay back to laminar state within a finite time with some probability function of Re. It was also shown that the life time of isolated puff increases in a super-exponential way as a function of Re [8]. As Re gets higher, the puff splits to form trains of puff that occupy the whole pipe [7, 8] as show in Figure 1.3. Later, these successive puffs spread themselves to form slugs. Figure 1.3 shows how turbulence proliferates starting from a localised puff at $Re = 2200$ as initial condition.

1.2.3 Fully developed turbulence

Once the Re value surpasses the transitional regime $Re \gtrsim 3000$, it enters the turbulent regime. In this regime, finite amplitude perturbation gets amplified and leads to transition of turbulence. Triggered turbulence then develops, as it moves downstream and becomes fully developed turbulence after a critical length, which depends on Re. Experimental investigation to find the critical position of fully developed turbulence, by measuring the velocity fluctuations, showed the critical distance from the inlet decreases as Re increases [10–14]. Recently, DNS on spatially developing pipe flows have been carried out with weakly but finitely perturbed laminar inflow. It was shown that the transition to full developed turbulence at high Re occurs more gradually rather than abruptly due to the presence of helical vortex filaments and large-scale vortices, which grow as they convect downstream and trigger turbulence [15]. Growth of the energy norm of the inlet perturbation was tending to be exponential, rather than algebraic, with axial distance. Figure 1.4 shows the evolution of friction factor $f = \frac{-(dP/dz)D}{1/2\rho U^2}$ and the energy norm $\parallel E \parallel = \int_0^R (u'^2_{x,rms} + u'^2_{y,rms} + u'^2_{z,rms}) r dr/(R^2V^2)$ as a function of the axial distance, z, for $Re = 8000$, where P is the pressure, ρ is the density, U is the bulk velocity and (u'_x, u'_y, u'_z) are the velocity fluctuation components in (x, y, z) directions, respectively. Here, r is defined as $\sqrt{x^2 + y^2}$, $R = D/2$ and V is the volume of the pipe. It can be seen that, during transition the energy norm of such inlet perturbations grow exponentially.

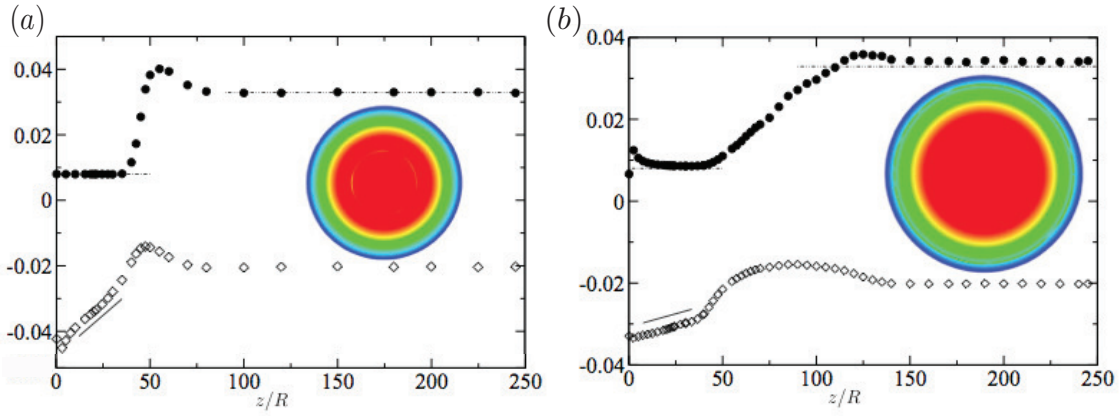

Figure 1.4: Friction factor f (•), and energy norm $10^{-2}\ \log_{10} \parallel E \parallel$ (⋄). Dash-dot-dash: $f = 64/Re$; dash-dot-dot-dash: Moody's correlation. (a) Perturbation as a ring at $0.4 \leq r/R \leq 0.42$, (b) $0.9 \leq r/R \leq 0.915$ for $Re = 8000$ respectively. Image taken from Wu *et al.* 2015 [15]

1.3 Expansion pipe flow

Expansion pipe flows or diverging pipe flows are special cases in which the outlet pipe diameter is larger than the inlet pipe diameter. They have many applications in industries for transferring fluid and also have application in thrust vectoring nozzles. Expansion chamber can also be found in engine exhaust. When blood flows through veins of the human body, they deposit fat, which gets accumulated on the walls there by forming a blockage called as stenosis. This blockage in some way acts like an expansion flow and researchers are looking deeply into it to understand the flow property. Another major application of diverging pipe is in drilling of borehole to extract oil. The following section will deal with the stability and sensitivity of expansion pipe flow and transition to turbulence.

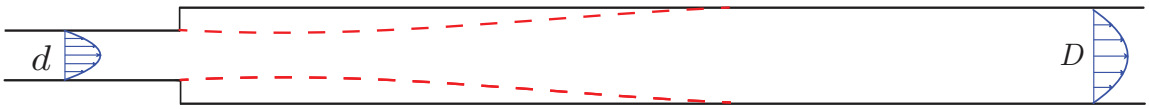

Figure 1.5: Schematic diagram of two dimensional expansion flow

1.3.1 Stability and sensitivity

The geometry of expansion pipe is shown in figure 1.5. It can be seen that the outlet diameter D is larger than the inlet diameter d. A non-dimensional number called expansion ratio $E = D/d$ is defined to measure how much the outlet and inlet diameter varies. One of the major differences between expansion pipe flow and constant diameter pipe flow is the formation of the recirculation region. Hagen-Poiseuille flow at the inlet is recovered close to the outlet, but the velocity at the outlet depends on the expansion ratio. The red dashed line on the figure 1.5 denotes the recirculation region that forms due to flow seperation, when flow move from the inlet and attaches downstream. Length of the recirculation region increases linearly as a function of Re. Note, Re here is based on the inlet diameter d. Early experiments on asymmetric sudden expansion [16, 17], showed the existence of shear layer instability at $Re \gtrsim 1500$ after which oscillations are observed down stream. A symmetric breaking bifurcation was identified by [18] after a critical Re. The initial symmetric flow is replaced by an asymmetric flow, which is steady. The asymmetry was seen through the presence of larger recirculation region on side of the walls. Recently, experiments [19] using magnetic resonance imaging technique, provided results on steady symmetry breaking bifurcation in the flow through a 1:2 sudden axisymmetric expansion as Re is increased. Figure 1.6(a) shows cross section taken downstream of the expansion region. It can be clearly seen that the recirculation region becomes asymmetric as the Re is increased. Centroid of the velocity distribution of is calculated to measure the asymmetry present in the velocity profile, figure 1.6(b) shows the measure of centroid as a function of Re. Initially the symmetric downstream flow evolves smoothly and rapidly into an asymmetric steady state. The critical point of the original supercritical bifurcation was found to be at $Re_c \approx 1139$. This symmetry breaking is the rotational analogue of the steady symmetry breaking observed in the symmetric planar expansion.

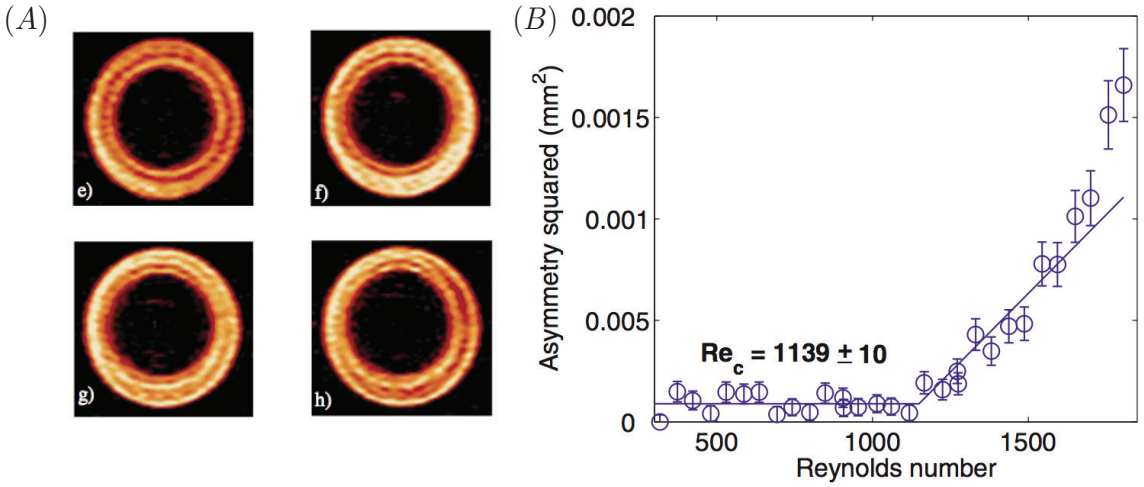

Figure 1.6: (A) Rapid acquisition with relaxation enhancement (Magnetic Resonance Imaging) images taken at $45h$ downstream from the expansion. Each of the velocity profiles used to construct the surfaces were acquired in 20 ms. The values of Re were (e) 946 ± 10, (f) 1234 ± 10, (g) 1478 ± 10 and (h) 1819 ± 10. (B) Graph of the square of a measure of the asymmetry of the flow plotted as a function of Re. The measure used was the centroid of the distribution of the velocity. The lines are least-squares fits of straight lines to the data. The intersection of the lines gives a value of $Re_c = 1139 \pm 10$ for the estimate of the symmetry breaking bifurcation point. Image taken from Mullin *et al.* 2009 [19]

Transient growth analysis [20] has shown that for values of the Re well below any linear instability, infinitesimal perturbation is strongly amplified. It was shown that the linear amplification places a vital role in the instability of the flow. In case of expansion flow, small infinitesimal perturbations are amplified close to the expansion region, where there is existence of shear layer due to flow separation. This amplification of perturbation, along with non-linear effect, causes the flow become unstable. As

discussed earlier, even though the flow may be globally stable, but due to transient growth, instabilities can occur. This kind of amplification of perturbation and decay is known as convective instability. Perturbations can be amplified up to a factor of 10^6 due to transient growth [20]. The initial perturbation that causes maximum amplification is present in the expansion section, i.e., sensitivity region of the pipe. Figure 1.7 shows the amplification of perturbation inside an expansion pipe. It shows how the perturbation at the expansion section grows, as it convect downstream and evolve into packets of waves characterised by a chevron structure. Inflectional instability mechanism helps the perturbation to gain energy as it convects downstream and reaches maximum value near the reattachment point. Once the maximum amplified perturbation crosses the reattachment point, they start to decay down.

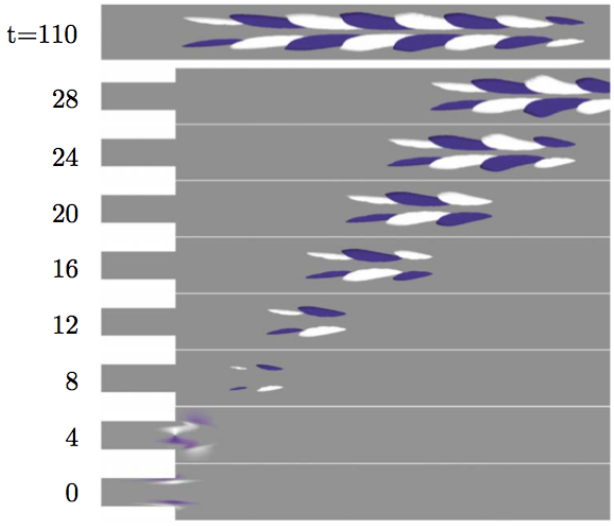

Figure 1.7: Evolution of optimal initial disturbance in the $m = 1$ mode visualised through contours/iso-surfaces of azimuthal velocity at $Re = 1200$ from $t = 0$ (bottom) in time intervals of four units in the spatial range of $-2.5 \leq x \leq 15$. The panel labeled $t = 110$ shows the evolved disturbance at its maximum growth: here the spatial range is $36.5 \leq x \leq 54$ from the expansion and the isosurface levels are two orders of magnitude larger than in the other panels. Image taken from Cantwell *et al.* 2010 [20]

Global stability analysis [21] using a pipe length of $L = 400d$, proved that the base flow which is axisymmetric is stable up to $Re \leq 3273$. It was shown that, once the Re goes beyond the critical value an oscillatory global mode with $m = 1$ and $St = 0.13$ occurs, where $St = \lambda_i/2\pi$ is the Strouhal number with λ_i being the imaginary part of the unstable eigenvalue. The eigenfunction of the corresponding unstable eigenvalue tend to appear slightly upstream of the reattachment point, which was in agreement with maximum growth of perturbation [20]. Experimental investigation [19] and global stability analysis has a critical value of $Re_c \approx 1139$ and $Re_c \approx 3273$ respectively. This discrepancy between the theory and the experiments is due to presence of imperfections in experiments, which gets amplified and leads to early transition.

1.3.2 Transition to turbulence

DNS with a finite amplitude perturbation [22] showed that the symmetry breaking can be achieved at $Re \approx 1500$, which is in good agreement with experiments of [19] for 1:2 asymmetric sudden expansion flow. The perturbation was applied at the inlet of the expansion pipe along with Hagen-Poiseuille flow. Once the critical Reynolds number is crossed, the recirculation region breaks down to form localised turbulence, which stays close to the expansion section. It was shown that the laminar and turbulent state can co-exist for a same value of Re. When the perturbation is removed from the system the asymmetric state goes back to axisymmetric state, whereas in case of disordered flow state, no detectable change in the flow was found. The position of the disordered state tends to remain the same. Figure 1.8 shows the detailed view of the finite amplitude of perturbation δ as a function of Re, required to trigger localised turbulence. Furthermore, experiments on slowly diverging pipe [23], has shown the formation of recirculation region depends upon the diverging angle. Once the Re goes beyond a critical value, a localised turbulence patch is formed close to the expansion section. Figure 1.9 shows a flow visualisation

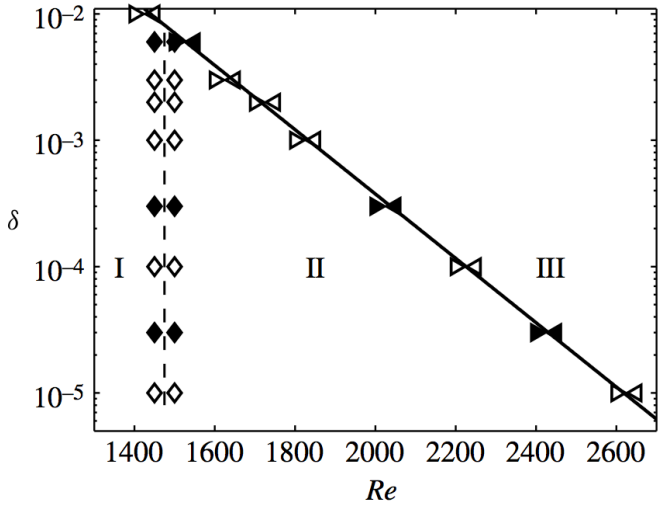

Figure 1.8: Plot of control parameter (δ, Re). Region I contains only steady states, region II only unsteady motion and region III both steady and unsteady flow, which was found by decreasing Re. Pairs of symbol are used to indicate the step size in Re. Plot taken from Sanmiguel-Rojas & Mullin 2012 [22].

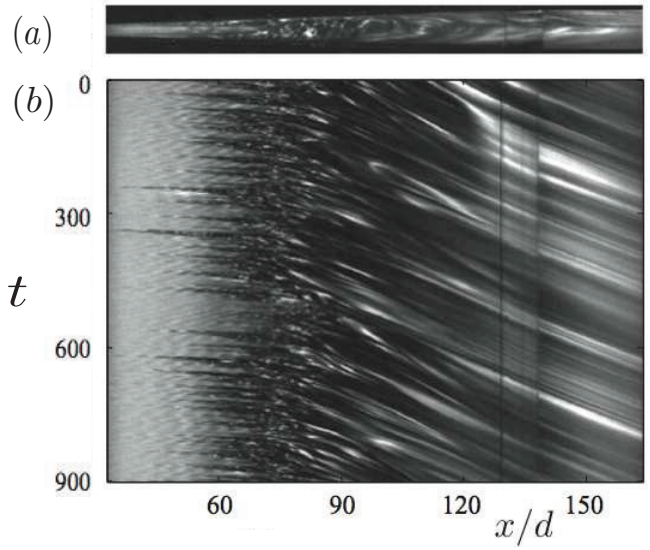

Figure 1.9: (a) Flow visualisation of localised turbulent patch in a diverging pipe (4°, $E = 10$). (b) Space-time diagrams for $Re = 800$ for an diverging pipe of angle 4°. Image taken from Peixinho & Besnard 2013 [23].

and a space diagram of the experiment where the dynamics of the localised turbulence can be seen as function of time.

1.3.3 Query

With the help of discussions from this chapter, certain question can be derived as below. Sensitivity study on 2D sudden expansion helps us to identify the most sensitivity region to trigger flow. To identify this region, is one of the motivation for the initial step. How does this sensitivity get affected by the divergence of the pipe will helps us to understand the effect of domain. Experimental investigation of expansion pipe flow has shown the existence of a super-critical bifurcation that occurs downstream the expansion section. Could a three dimensional numerical simulation helps us to identify the bifurcations and study about the onset of turbulence? was a initial question that we could pose before going in to turbulence. Earlier, numerical simulations have shown the existence of hysteresis in the expansion pipe flow, one motivation is to reanalysis this hysteretic behaviour and study the regime carefully. In order to trigger turbulence, what shape, size and position of perturbations could be built to have a better transition study could be one of the main motive. If so, how does this turbulent patch behave in long time? Do they self-sustain?. How do they decay and where do they get their kinetic energy from is an interesting area to look for. How well does this localized turbulence, resemble to a travelling puff in a straight pipe flow is another important aspect to look for. In terms of fully developed turbulence, most of the literatures on identifying the critical length of developed turbulence are calculated using the velocity fluctuation components. Pressure, which is strongly coupled with velocity, is less explored, we could ask how well does the velocity and pressure correlate along the axial direction of the pipe flow. Is it possible to identify the critical length for fully developed turbulence using pressure fluctuations? How does the pressure fluctuations grow, as functions of axial position of the pipe are some of the interesting areas to observe.

1.3.4 Outline

Queries that are put forth in the previous section are answered through the chapters below. A brief description of each chapter and their content is given below:

1.3.4.1 Chapter 2

Two dimensional sudden expansion flow and gradual diverging flow is investigated via global stability analysis. The direct mode and the adjoint mode are obtained for the unstable eigenvalue. Structural sensitivity of the baseflow is computed to understand the region where the flow sensitivity due to perturbation is studied. Later, explanations about global stability analysis and transient growth analysis are discussed for three-dimensional sudden expansion pipe flow.

1.3.4.2 Chapter 3

Spectral Element Method, which is used for performing DNS of expansion pipe flow, is briefly explained. Domain decomposition, weak formulation of Navier-Stokes equation, discrete form of the equation and time discretisation are explained. Finally, implementation of SEM inside the open-source code NEK5000 is discussed.

1.3.4.3 Chapter 4

Chapter four provides DNS results of flow though gradual expansion pipe with tilt perturbation applied at the inlet along with Hagen-Poiseuille flow. Initially, it looks into the onset and growth of recirculation region in a gradual expansion pipe as discussed in (1.3.2) and compares the result with experimental data in literature. Later, asymmetry growth due to perturbation is measured, which is in good agreement with experiments [19]. The dynamics of the localised turbulence is studied as a function of time at high Re to check if the flow recovers Hagen-Poiseuille flow at the outlet. Relaminarisation of the localised turbulence is done by reducing the value of Re and hystersis property is also studied. Finally, coherent structures of the flow are found and compared with that of the puff as discussed in section (1.2.2). It is shown that the $m = 1$ mode dominates the flow and the flow is more active in the core region.

1.3.4.4 Chapter 5

Here, tilt perturbation is replaced by a vortex perturbation, in order to have perturbation that satisfies continuity boundary at the inlet. Tilt perturbation leads to an abrupt transition, whereas the vortex perturbation gives a less abrupt transition. At low value of vortex strength, optimal perturbation with chevron like structure as discussed in section (1.3.1) is found, which initially occurs in the expansion section. It amplifies, as it moves downstream but breaks due to non-linear effect. This breaking leads to series of turbulent patches that occurs quasi periodically. Once the strength of vortex perturbation reaches a critical value, the turbulent patch, which was moving during low vortex strength, now occupies a constant spatial position like localised turbulence in chapter 3. Finally, Proper Orthogonal Decomposition (POD) is applied to the localised turbulence to find the most energetic modes. The first POD mode lies in the center of the pipe and close to expansion section, there by validating that the localised turbulence patch gains it energy from the inlet flow and validates the coherent structure study from chapter 4.

1.3.4.5 Chapter 6

This chapter is an on going study about behaviour of the vortex perturbation in a straight pipe. Recent DNS on spatially developing flow [15] where weakly turbulent flow was injected into the inlet of laminar pipe flow and showed how this weakly turbulent structures amplify as they advect downstream and trigger turbulence. A large computational domain of size 20 million has been built to understand the onset and growth of the vortex perturbation inside the straight pipe. It is assumed that this will answer us the kind of structures reach the expansion region, when vortex perturbation is used. Secondly, we are also interested in investigating the development pressure in the pipe flow and study how the pressure fluctuations scales with Re.

1.3.4.6 Chapter 7

Studies on developing turbulent pipe flow, as discussed in section (1.2.3) is generally been done on velocity fluctuations to identify the fully developed turbulent regime. The pressure poisson equation which is derived by taking the divergence of the Navier-Stokes equation reveal that the velocity and pressure or strongly coupled. Chapter 7 presents the results of growth of pressure fluctuations along axial direction. It is shown that a self-similarity exists for pressure fluctuation growth and it is very robust to perturbation. In the end, tuft visualisations are presented to show the increase of fluctuation rate when compared to the inlet and in the developed turbulent regime.

1.3.4.7 Conclusion and future perspective

A final conclusion to the thesis is given here with a brief discussion of the results obtained using numerical simulations and experiments. In order to continue the research of expansion pipe flow, certain questions that were are raised during the course of the thesis is put forward in the future perspective section.

Chapter 2

Structural sensitivity of expansion flow

2.1 Introduction

Properties of two dimensional expansion flows, which have smaller inlet and larger outlet section, are well documented in literature. However, before performing three dimensional expansion pipe flows, studying two dimensional cases helps to understand the flow behaviour, onset of the recirculation region, length of domain required, critical Reynolds number and the sensitive regions inside the domain. The reason for choosing a two dimensional expansion flow is because of its less computational cost and to understand the physics in a less complex geometry.

Experimental studies on two dimensional sudden expansion flow with expansion ratio of three [18] have shown the onset of symmetry breaking bifurcation that occurs at $Re_c = 40$. Here, channel half-height was used as the characteristic length to define Re. At higher Re, the flow becomes time dependent, which arises may be due to the presence of three-dimensional effects. Placing a contraction at the end of sudden expansion flow geometry [24] tends to increases the Re at which symmetric bifurcation occurs. It was also shown that there exists an instability that occurs due to the inlet expansion and instability due to outlet contraction. In this case, the length of the expansion section plays a vital role in determining which instability occurs first.

Stability analysis of the expansion flow, helps us to understand the critical Reynolds number at which the flow becomes unstable. It has helped to identify the existence of a symmetry breaking bifurcations [25–27] that lead to asymmetry of recirculation regions inside the domain. Sensitivity analysis of two dimensional cylinder flow [28] has helped to identify the most sensitive region that causes largest shift to unstable eigenvalue behind the cylinder.

Recently, sensitivity analysis [29] were carried out on two dimensional expansion flow with a perturbation that may be produced by realistic passive control. With the aid of the information obtained from the sensitivity parameter a control was designed. A cylinder was introduced in the expansion section, which acts as a passive control to the system. It was shown that by introducing such a passive control, the flow can be maintained steady symmetric for a higher Re.

In global stability analysis, a steady state flow, known as *base flow* is investigated for the its behaviour to an infinitesimal perturbation. These perturbations are governed by linearised Navier-Stokes equation (LN-S). In the context of a non-linear dynamical system, global stability is defined as the system's susceptibility to infinitesimal disturbances from an equilibrium point, which in our case is a steady-state solution to the Navier-Stokes Equations. Given a non-linear system $\dot{\mathbf{u}} = f(\mathbf{u})$ let $\mathbf{u}_0$ be an equilibrium point, such that $f(\mathbf{u})$ is continuously differentiable about a neighbourhood of $\mathbf{u}_0$. Let $Df(\mathbf{u}_0)$ be the Jacobian of f evaluated at $\mathbf{u}_0$ and so $\dot{\mathbf{u}} = Df(\mathbf{u}_0)u$ is the linearisation of $\dot{\mathbf{u}} = f(\mathbf{u})$ about $\mathbf{u}_0$. Then, the point u_0 is asymptotically stable if $Re(\lambda_i) < 0$ for all eigenvalues λ_i of $Df(u_0)$ and the point u_0 is unstable if $Re(\lambda_i) > 0$ for one or more eigenvalues λ_i of $Df(u_0)$.

In this chapter, we present the results of stability and sensitivity analysis of two cases of expansion flows with an expansion ratio of two (i) sudden expansion and (ii) gradual expansion with an angle of divergence 10°.

2.1.1 Global stability analysis

The equations of fluid flow *i.e.,* incompressible Navier-Stokes Equation can be written as:

$$\frac{\partial \mathbf{U}}{\partial t} + \mathbf{U} \cdot \nabla \mathbf{U} = -\nabla P + \frac{1}{Re}\Delta \mathbf{U}, \tag{2.1}$$

$$\nabla \cdot \mathbf{U} = 0. \tag{2.2}$$

where $\mathbf{U}$ is the relative fluid velocity, P is the pressure and $Re = Ud/\nu$ is the Reynolds number, Since the problem is two dimensional we can represent this in terms of state vector Λ such that

$$\Lambda = [\mathbf{U}(x, y, t), P(x, y, t)]. \tag{2.3}$$

The global linear stability analysis is done on the flow vector Λ. It is reasonable to take the vector in the form of

$$\Lambda = \Lambda_0 + \Lambda_1 e^{\lambda t}, \tag{2.4}$$

Where $\Lambda_0 = [\mathbf{U}_0(x, y, t), P_0(x, y, t)]$ is called as the base state or the *baseflow* and the structure of the base flow is steady and symmetric and $\Lambda_1 = [\hat{\mathbf{u}}(x, y), \hat{p}(x, y)]$ is the small perturbation applied to the base flow. The perturbation can be found in the form of an *eigenmode* with a corresponding *eigenvalue*.

$$\lambda = \lambda^r + i\lambda^i \tag{2.5}$$

λ^r corresponds to the growth rate and λ^i corresponds to the oscillating part of the eigenmodes. The oscillating frequency can be used to obtain a non-dimensional parameter called as Strouhal number $St = \lambda^i d/2\pi U_o$, where U_o is the velocity at the inlet of the baseflow.

2.2 Base flow

The base flow is the time independent solution of the system on which a linear stability analysis is carried out. It is obtained from the first right hand term of (2.4) $\Lambda_0 = [\mathbf{U}_0(x, y, t), P_0(x, y, t)]$ which is the steady expansion flow. The corresponding equations to obtain a base flow is given by:

$$\nabla.\mathbf{U_0} = 0 \tag{2.6}$$

$$0 = -\mathbf{U_0}.\nabla\mathbf{U_0} - \nabla P_0 + \frac{1}{Re}\Delta\mathbf{U_0}. \tag{2.7}$$

The boundary conditions are given by

$$\mathbf{U}_0(x, y) = 2(1 - 4y^2) \qquad Inlet\,, \tag{2.8}$$

$$\mathbf{U}_0(x, y) = 0 \qquad walls\,, \tag{2.9}$$

$$P\boldsymbol{n} - \boldsymbol{n} \cdot \nabla\mathbf{U}_0(x, y)/Re = 0 \qquad outlet. \tag{2.10}$$

Boundary condition at the inlet corresponds to parabolic velocity profile. No slip condition in the wall is implement by equation (2.13) and the stress free pressure outlet is implemented (2.14).

2.3 Newton Method

In order to obtain the base flow, an iterative convergence method is used. Laplacian equation is solved to set the initial condition for the iteration.

$$\nabla^2\varphi = 0 \tag{2.11}$$

where φ is the stream function and ∇^2 is the laplace operator. The boundary conditions are given by

$$\varphi = y \qquad Inlet\,, \tag{2.12}$$

$$\varphi = 0 \qquad walls\,, \tag{2.13}$$

$$\varphi = 0 \qquad outlet. \tag{2.14}$$

The momentum equation contains a advection term $(\mathbf{U_0}.\nabla)\mathbf{U_0}$, to solve it an iterative method called the Newton method is used. The approximate solution which is obtained through solving (2.11) can be

used as an initial guess to the newton method. The approximate solution is in a such way that it does not satisfies the boundary conditions (4.3) and it is written as

$$\mathbf{NS}(\mathbf{U_0}, P_0) \neq 0 \tag{2.15}$$

where,

$$\mathbf{NS}(\mathbf{U_0}, P_0) = \begin{pmatrix} \nabla \mathbf{U_0}.\mathbf{U_0} + \nabla P_0 - Re^{-1}\nabla^2 \mathbf{U_0} \\ \nabla.\mathbf{U} \end{pmatrix} \tag{2.16}$$

In the equation (2.16) we intended to add a small value of $(\delta\mathbf{U}, \delta P)$ so that we yield a base flow of the form $(\mathbf{U_0} + \delta\mathbf{U}, P_0 + \delta P)$ which satisfies the boundary conditions (4.3) given a solution of the form

$$\mathbf{NS}(\mathbf{U_0} + \delta\mathbf{U}, P_0 + \delta P) = 0 \tag{2.17}$$

The above equation can be written in the linear form as

$$\mathbf{NS}(\mathbf{U_0}, P_0) + \mathbf{LN} - \mathbf{S}_{(\mathbf{U_0}, P_0)}(\delta\mathbf{U}, \delta P) = 0 \tag{2.18}$$

$$\mathbf{LN} - \mathbf{S}_{(\mathbf{U_0}, P_0)}(\delta\mathbf{U}, \delta P) = -\mathbf{NS}(\mathbf{U_0}, P_0)$$

$$\mathbf{LN} - \mathbf{S}_{(\mathbf{U_0}, P_0)} \begin{pmatrix} \delta\mathbf{U} \\ \delta P \end{pmatrix} = \begin{pmatrix} (\delta\mathbf{U_0}).\delta\mathbf{U} + (\nabla\delta\mathbf{U}).\mathbf{U_0} + \nabla(\delta P) - Re^{-1}\nabla^2(\delta\mathbf{U}) \\ \nabla.\delta\mathbf{U} \end{pmatrix} \tag{2.19}$$

Where **LN-S** is the linear part of Navier-Stokes equation. Solving the above equation (2.19) gives a solution of the form $(\delta\mathbf{U}, \delta P)$ which is added to the $(\mathbf{U}_0, P_0)$ which is again taken into the loop as better approximation.

$$(\mathbf{U}_0, P_0) \leftarrow (\mathbf{U_0} + \delta\mathbf{U}, P_0 + \delta P) \tag{2.20}$$

The loop is iterated until a convergence criteria is reached (i.e)

$$\mathbf{NS}(\mathbf{U_0}, P_0) < tol \tag{2.21}$$

where *tol* is a small value to check convergence. In our case $tol = 0.0000001$.

2.4 Perturbation analysis

The linear stability analysis is done by substituting (2.4) in the governing equations (2.2) and removing the higher order terms, which leads to

$$\nabla \cdot \hat{\mathbf{u}} = 0 \tag{2.22}$$

$$\lambda\hat{\mathbf{u}} + \hat{\mathbf{u}}.\nabla\mathbf{U_0} + \mathbf{U_0}.\nabla\hat{\mathbf{u}} + \nabla\hat{p} - \frac{1}{Re}\nabla^2\hat{\mathbf{u}} = 0 \tag{2.23}$$

The boundary conditions are given by

$$\hat{\mathbf{u}} = 0 \qquad Inlet\,, \tag{2.24}$$

$$\hat{\mathbf{u}} = 0 \qquad walls\,, \tag{2.25}$$

$$\hat{p}\boldsymbol{n} - \boldsymbol{n} \cdot \nabla\hat{\mathbf{u}}/Re = 0 \qquad Outlet. \tag{2.26}$$

The equations from (2.22) can be written in a generalized eigenvalue problem form as

$$\mathcal{A}\Lambda_1 = \lambda\mathcal{B}\Lambda_1 \tag{2.27}$$

Where $\mathcal{A}$ and $\mathcal{B}$ are linear non symmetric operators, solving this gives for $\Lambda_1 \neq 0$ gives us non-trivial solutions which contributes to complex eigenpair (λ, Λ) also known as eigenvalue spectrum. This spectrum helps us to identify the flow is stable are unstable. If growth rate λ_r is positive for any of the eigenvalue, the flow is unstable and the perturbation is amplified in time. When the perturbation velocities cannot be considered small any more, the evolution of the perturbation is no longer predicted by the linear equations, since non-linear effects became important. Nonetheless, the linear approach is important in detecting physical growth mechanism.

2.5 Structural sensitivity analysis

Sensitivity analyses based on adjoint equations are widely used in stability analysis, where they provide information related to the mechanism of disturbances growth. In Giannetti and Luchini [28] it is shown by a perturbation analysis that, for each considered global mode $(\hat{\mathbf{u}}, \hat{p}, \lambda)$, the addition of a perturbation $\delta\hat{\mathbf{f}}$ at the right hand side of the momentum equation (2.22) causes the following variation $\delta\lambda$ of the eigenvalue λ:

$$\delta\lambda = \frac{\langle \hat{\mathbf{u}}^+, \delta\hat{\mathbf{f}} \rangle}{\langle \hat{\mathbf{u}}^+, \hat{\mathbf{u}} \rangle} \tag{2.28}$$

Where $\langle a, b \rangle = \int_\Omega (a^* \cdot b) d\Omega$ is the scalar product between the complex vectors a and b on the flow domain Ω and the asterisk * denotes the conjugate of a complex quantity. The vector field $\hat{\mathbf{u}}^+$ is the velocity field of the mode adjoint. The adjoint operator L^+ of a differential operator L is defined as the unique operator satisfying:

$$\langle Lu, v \rangle = \langle u, L^+ v \rangle \tag{2.29}$$

The equations from (2.29) can be written in a eigenvalue problem form as, which is Hermitian transpose of the direct eigenvalue problem (2.27):

$$\mathcal{A}^H \Lambda_1 = \lambda^+ \mathcal{B}^H \Lambda_1 \tag{2.30}$$

Modes obtained by solving (2.30) are called adjoint modes. Structural sensitivity equation helps to describe the effect of baseflow modification on each global mode. It helps to identify the region inside the computational domain that produces the biggest stability variation in a flow. The most important part of sensitivity analysis is to look for perturbation that generates the maximum variation to the unstable eigenvalue. The equation is constructed using the direct mode and the adjoint mode:

$$S(x,y) = \frac{\| \vec{v}_i(x,y) \| \| \vec{u}_i(x,y) \|}{\left| \int_\Omega \vec{v}_i^* \cdot \vec{u}_i \right|} \tag{2.31}$$

The vectors v_i and u_i represent the adjoint and direct eigenfunction, corresponding to the i^{th} eigenvalue. $S(x,y)$ is the structural sensitivity parameter.

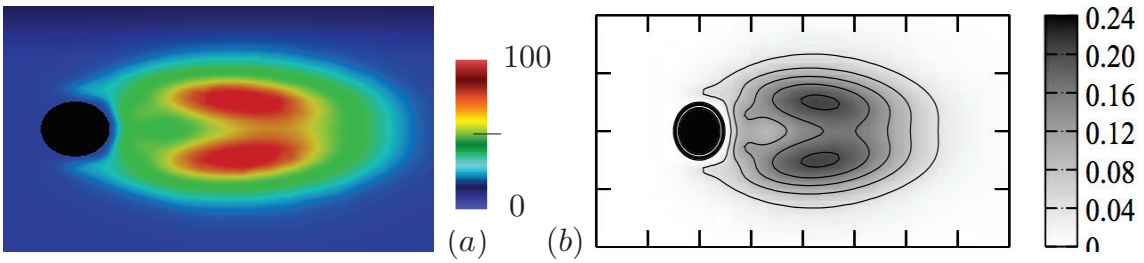

Figure 2.1: Structural sensitivity parameter over a two dimensional cylinder at $Re_c = 45$ (a) Computed using our code (b) Image taken from Giannetti & Luchini 2007 [28], red and blue corresponds to maximum and minimum respectively.

2.6 Validation

In order to validate the method, we used FreeFem++, a finite element solver to create computational domain and to perform the stability analysis. Specifically, flow over a two dimensional cylinder was tested. The first unstable mode was obtained at a critical Reynolds number $Re_c = 45$, which has a Strouhal number of $St = 0.119$. It is called the Von Karman 1 mode because; it is associated with the onset of vortex shedding which leads to classical Von Karman streets. As the Re is increased further a second mode tends to move towards the unstable region, at $Re_c = 110$ the mode becomes critical which has a $St = 0.122$, we call it as the Von Karman 2 mode as it has nearly the same frequency of the Von

Karman 1 [30, 31]. The structural sensitivity parameter was computed using equation (2.31) is shown in figure 2.1, along with the structural sensitivity obtained by Giannetti & Luchini 2007 [28] for $Re_c = 45$. It shows the sensitivity region lies behind the wake of cylinder in the recirculation region formed behind it.

2.7 Computational domain and mesh

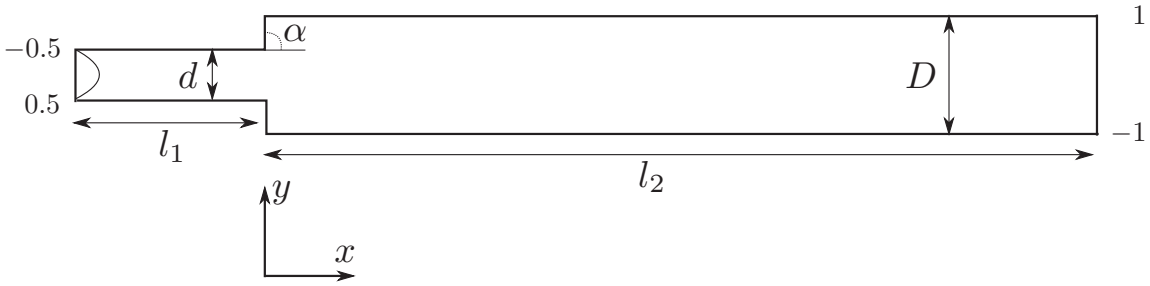

Figure 2.2: Schematic diagram of 2D expansion flow

Schematic diagram of the computational domain is shown in figure 2.2, here the inlet height is defined by d and outlet height by D. Ratio between the inlet and outlet height is called as the expansion ratio $E = D/d$. In the present study $E = 2$. l_1 and l_2 represent the length of inlet and outlet section from the expansion section. The divergence angle is defined by α, if $\alpha = 90°$ it is sudden expansion flow. Output of the mesh convergence study is show in table 2.1. Initially, the study was carried out only by changing the number of mesh triangle N, it was found that Mesh number 4 to predict the drag and the real part of the eigenvalue with a good accuracy. Drag is computed by $\int_\Omega \mathbb{T}_0 \cdot \mathbf{n} dl$, where $\mathbb{T}_0$ is the base flow stress tensor. Later, the effect of the length of the inlet and outlet section, (i.e.), l_1 and l_2 was studied by keeping the mesh density constant. The influence of l_1 and l_2 was found too negligible in the present case. Finally, Mesh number 4 was chosen for performing global stability and structural sensitivity analysis.

Mesh	l_1	l_2	N	λ_r	Drag
1	5	35	13292	-0.000623987	0.427382
2	5	35	16237	-0.000617999	0.427466
3	5	35	24565	-0.000610824	0.427714
4	5	35	31686	-0.000613321	0.427779
5	10	35	28413	-0.000604445	0.614185
6	5	40	34331	-0.000590479	0.451006

Table 2.1: Mesh dependency study on the least stable eigenvalue, here N is the number of mesh triangles.

2.8 Sudden expansion

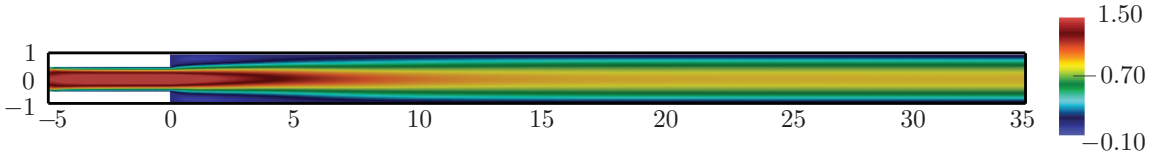

Figure 2.3: Contour plot of streamwise velocity of the baseflow computed using mesh 4

Base flow computed by Newton method for a two dimensional expansion flow is shown in figure 2.3. It can be seen that the flow has two re-circulation regions that are symmetric around the axis to each other. The maximum velocity is in the center of the expansion and the velocity decreases once the

flow expands downstream. The convergence of the base flow was checked by measuring the L^2 norm. Once the base flow was obtained, linear stability analysis was performed using equation (2.22). At low Re the flow was globally stable and all the eigenvalue were negative. As Re increased, few eigenvalue started moving in the positive direction. The first unstable eigenvalue $\lambda_r = 0.00001$ was obtained at critical Reynolds number $Re_c = 143$. Figure 2.4 shows the plot of first 6 least unstable eigenvalues. The eigenvalue with blue circle is the most unstable as it growth value becomes positive. Mode obtained is termed as direct mode or symmetry breaking mode and it has no oscillating component, as the imaginary part of the eigenvalue is zero. The adjoint modes were computed using equation (2.30).

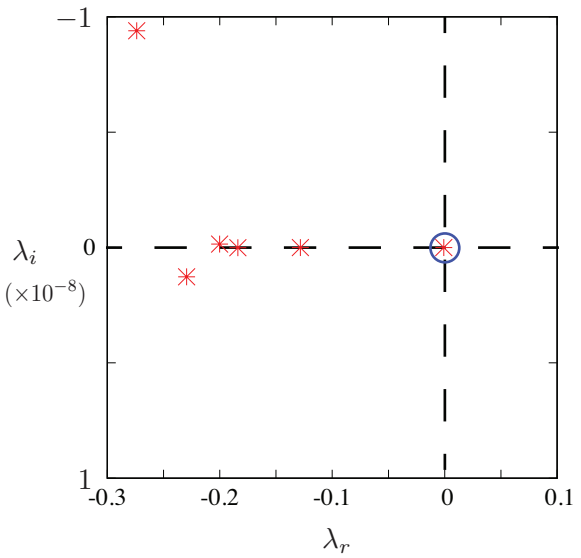

Figure 2.4: First 6 eigenvalue obtained for a sudden expansion flow at $Re_c = 143$. The eigenvalue circled with blue ring is the least unstable.

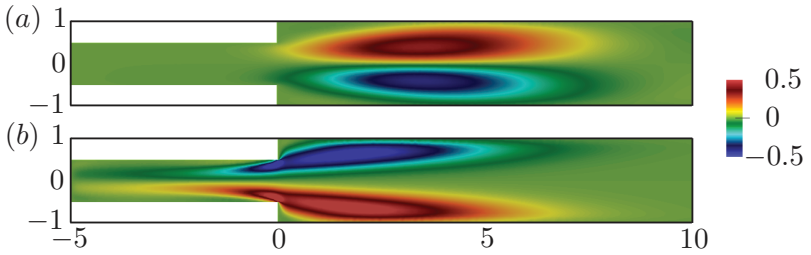

Figure 2.5: Contour plot of streamwise velocity at $Re_c = 143$. (a) Direct mode, (b) adjoint mode. Only $10d$ out of $35d$ is shown.

Figure 2.5(a) corresponds to streamwise velocity and it can be seen that it has a positive and a negative lobe. The positive lobe and negative lobe represents that the flow moves faster and slower respectively. This difference in the flow breaks the symmetry in the flow; this mode makes the center core region to shift to one side of the domain, which in turn makes one of the recirculation regions longer and the other one shorter. Since the mode has no oscillating component, the size of the recirculation region becomes independent of time. The structure of adjoint mode in the streamwise direction is shown in figure 2.5(b) has two lobes similar to that of the direct mode but seem to be situated in area of recirculation region. It tends to stretch from the expansion region and to be very active in the near wall region.

Crosswise velocity for direct and adjoint mode are shown in figure 2.6 and it can be seen that they are less dominant went compared to the streamwise velocity modes. Pressure modes are show in figure 2.7, the pressure modes tends to alternate itself along the streamwise direction, more active near the expansion region and tends to decay as it moves downstream.

Structural sensitivity of the base flow is computed with the help of direct and adjoint modes using equation (2.31). It helps us to identify the structure of perturbation to baseflow that tend to have max-

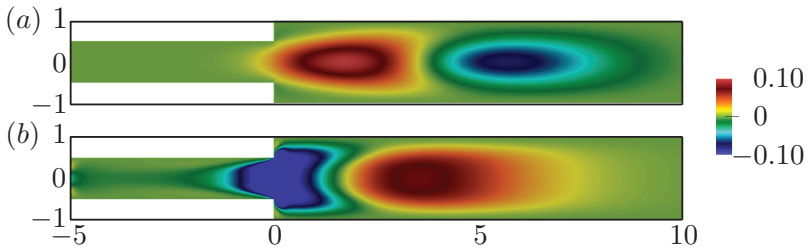

Figure 2.6: Contour plot of crosswise velocity at $Re_c = 143$. (a) Direct mode, (b) adjoint mode. Only $10d$ out of $35d$ is shown.

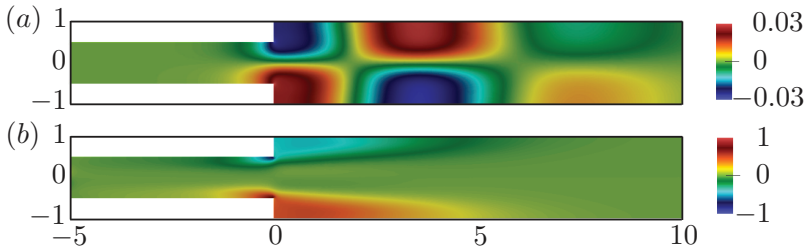

Figure 2.7: Contour plot of pressure at $Re_c = 143$. (a) Direct mode, (b) adjoint mode. Only $10d$ out of $35d$ is shown.

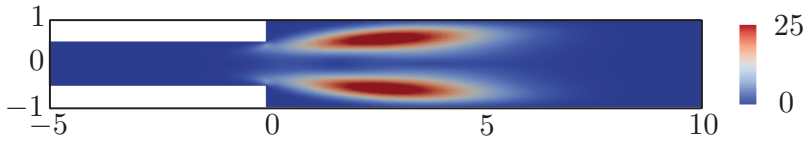

Figure 2.8: Structural sensitivity parameter, S, for the most unstable eigenvalue. Only $10d$ out of $35d$ is shown.

imum variation to the least unstable eigenvalue. Figure 2.8 shows the structural sensitivity parameter, one of the most important thing to note is that region of the maximum sensitivity lies in the shear layer that form between the expanding flow and the recirculation region. It is also found to exist close to the expansion section. This provides us with an intuition that any perturbation close to the expansion section is increases the sensitivity.

Our results on linear stability analysis on symmetric base flows, which confirms a picthfork bifurcation are consistent with literature on stability analysis of two dimensional expansion flow [18, 27, 29].

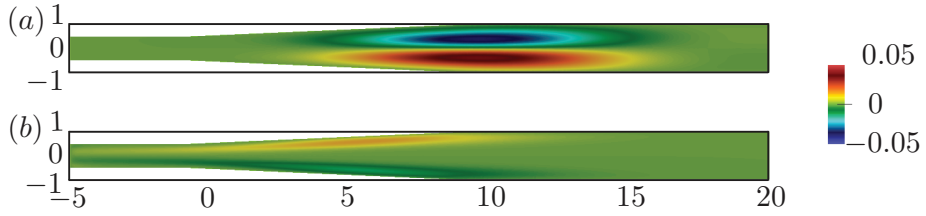

Figure 2.9: Contour plot of streamwise velocity at $Re = 475$. (a) Direct mode, (b) adjoint mode. Only $20d$ out of $45d$ is shown.

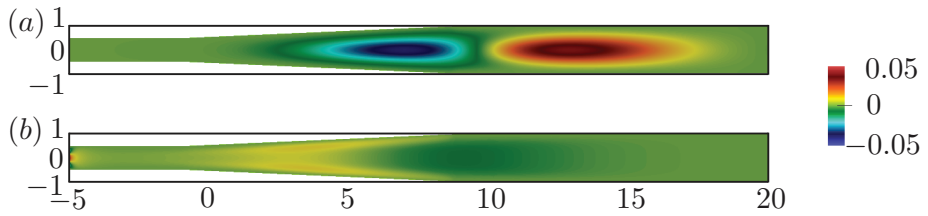

Figure 2.10: Contour plot of crosswise velocity at $Re = 475$. (a) Direct mode, (b) adjoint mode. Only $20d$ out of $45d$ is shown.

2.9 Gradual expansion

Further, a gradually expansion section of diverging angle $\alpha = 10°$ was analyzed. The mesh and the size of the domain were adjusted accordingly to have accurate results. It was found that the symmetry breaking mode occurs at $Re_c = 475$, which is much higher than the case of a sudden expansion section. One of the reason for such higher value of critical point is that the onset of the recirculation in a gradually expansion section occurs at much higher Re. It is to be noted that, if the diverging angle becomes zero i.e $\alpha = 0$ then it is a case of plane poiseuille flow, which becomes unstable at $Re_c = 5772$. Figure 2.9 shows the direct and adjoint mode along the streamwise direction. Similar to that of the sudden expansion, the direct mode consist of a positive and negative lobe but which extends itself all along the gradually expansion section. Crosswise velocity shown in figure 2.10 shows that how gradual expansion can effect the length of these lobes that extend from inlet of the expansion section to the outlet of expansion section. Pressure mode in figure 2.11 alternate themselves but looks elongated all over the expansion section and the adjoint pressure mode in figure 2.11 tends to be active around the walls of the expansion section. Contour for sensitivity parameter is shown in figure 2.12, it clearly shows that the region of maximum sensitivity lies all over the expansion region and remains close to the wall, which is due to the presence a very small recirculation region in the domain.

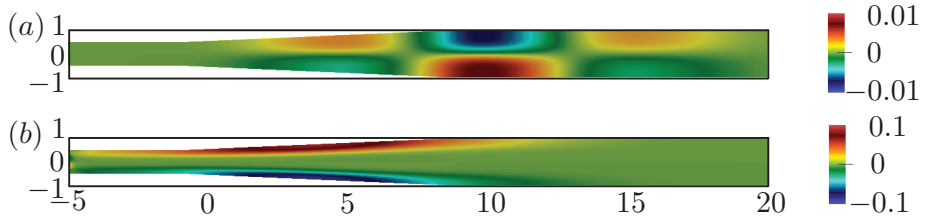

Figure 2.11: Contour plot of pressure at $Re = 475$. (a) Direct mode, (b) adjoint mode. Only $20d$ out of $45d$ is shown.

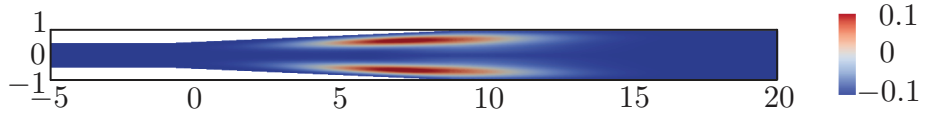

Figure 2.12: Structural sensitivity parameter, S, for the most unstable eigenvalue. Only $20d$ out of $45d$ is shown.

2.10 Conclusion

Stability analysis on a two-dimensional sudden expansion and gradual expansion shows that the first symmetry break mode is stationary and has no oscillating component to it. For sudden expansion the first unstable mode occurs at $Re_c = 143$ and in case of gradual expansion it occurs at $Re_c = 475$. Further, analysis with varying the divergence angle showed that the value of Re_c tends to increase with decreasing expansion angle. Streamwise velocity mode tends to be situated close to expansion section,

in case of gradual expansion section; it looks elongated along the expansion region. Pressure modes tend to alternate themselves along the streamwise direction and present very close to the expansion section. Structural sensitivity parameter that gives the region to which baseflow is susceptible, in case of sudden expansion it remains close to expansion and section and very sensitive in the shear layer formed between the recirculation region and the core flow. For gradual expansion, the sensitive region tends to lie all along the expansion region. Both the analysis shows that any perturbation at the expansion is sensitive and can lead to early transitions. Stability analysis in three dimension is difficult to achieve because the base flow is global stable for $Re_c \lesssim 3400$, it requires a long computational domain and the code has to be parallelised to solve it. The structural sensitivity analysis is in accordance with the finding of the [20, 32] that the expansion section acts like an amplifier, which amplifies the incoming perturbation. It can also be noted that [20] in three dimensional transient growth analysis the perturbation is amplified in between the recirculation region and starts to decay, once it crosses the reattachment point. Further, stability analysis with varying expansion ratio [33] has shown that after the symmetry breaking instability, a second instability occurs to three different modes. The type of modes depends upon the expansion ratio. We are interested in studying this variation of modes with respect to the expansion ratio. Similarly, application of passive flow control method [29] on the gradual expansion flow would help us to understand the effects of it. All the above methods are done using linearised NS equations, without taking into account the non-linear part. In order to consider the non-linearity of the equation, DNS with perturbation close to inlet has to be performed. In chapter 3, we will study about applying a simple perturbation to the inlet pipe and study the transition behaviour.

Chapter 3

Computational Method

3.1 Introduction

The NS equations (1.1) can be solved in different ways, which mostly dependent on type of the problem. Finite Difference Method (FDM), Finite Element Method (FEM), Finite Volume Method (FVM), and spectral methods (SM) are the well known methods used in general. All these methods have their own advantages and disadvantages. The FDM method is easy to implement, but cannot be applied for complex geometry problems. FEM can handle complex geometries; it is therefore applicable to wide range of problems. The strong form of the partial differential equation is reduced to weak form by using the variational formulation. The weak form of the equation consists of trail functions (expansion or approximating functions) and test functions (weight functions). The approximate representation of the solution to the differential equation is given by the trail functions, which is a linear combination of suitable trial basis functions. The test function ensures that the differential equation and some boundary conditions are satisfied as closely as possible by the truncated series expansion. In order to ensure that the approximate solution, defined by the truncated series satisfies the differential equation, the test function are used to minimize the residual that is obtained when the approximate solution is substituted into the differential equation. The test function is obtained in a way that the inner product of the test function added with the residual is zero. The choice of trail functions is the main criteria that differentiate the SM from FEM. Choosing a high order basis functions leads to SM that has a high spatial accuracy. Similar to FDM, applying SM to complex grids is difficult. In 1984, Patera [34] first gave the method that combines the flexibility of FEM along with the accuracy of SM. The hybrid method was called the "Spectral Element Method" (SEM). In this chapter, we initially present the spatial and temporal discretization of the incompressible Navier–Stokes equations. In the following section, the discrete form of the equation is explained along with the fractional step method. Later, NEK5000 [35], a three dimensional SEM code developed by in National Argonne Laboratory is discussed.

3.2 Spectral Element Method

3.2.1 Domain Decomposition

As mentioned, the computational domain Ω is divided into sets of non-overlapping sub-domains (elements) $\Omega_e, e = 1, 2..., E$ such that :

$$\Omega = \bigcup_{e=1}^{E} \Omega_e \tag{3.1}$$

Each element can be visualized as a smaller computational domain on which spectral method (A.2) is applied. These elements share their boundaries; hence the elements have same order of polynomial basis functions. This method of having same order for each element is called as conformal grid. If the elements have hanging nodes, then it is called non-conformal grid, which makes the discretization process complex. "Lagrange polynomials" (A.2.2) are used for higher order basis functions. Consider a finite sequence of distinct points $\{\xi_i\}_{i=0}^{N} \subset [-1, 1]$, where $\xi_0 = -1$ and $\xi_N = 1$, and let the function $u : [-1, 1] \to \mathcal{R}$ be a one dimensional representation of a solution. The Lagrangian interpolation of u

reads

$$u(\xi_i) = \sum_{j=0}^{N} u_j \phi_j(\xi_i) = u_i, \qquad i = 0, 1..., N. \tag{3.2}$$

where $\{u_j\}_{j=0}^{N}$ is the basis coefficients corresponding to a set of orthogonal nodal basis functions

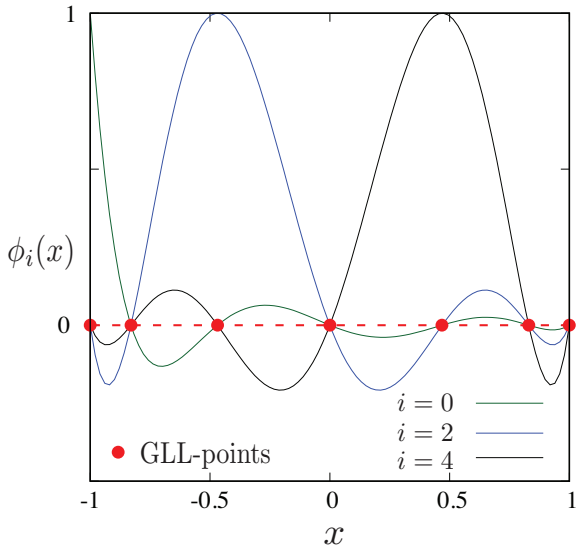

Figure 3.1: GLL mesh for a square domain $\Omega = [-1, 1]$ with $E = [5 \times 5]$, (a) $N = 5$ and (b) $N = 10$

$\{\phi_j\}_{j=0}^{N}$. Nodal basis functions are known as "Lagrangian interpolants" and have the property that the basis coefficients $\{u_i\}_{i=0}^{N}$ are also function values at the distinct points $\{\xi_i\}_{i=0}^{N}$, i.e. $\phi_j(x_i) = \delta_{ij}$ holds, where δ_{ij} is the Kronecker delta function, which equals to one if $i = j$ and zero otherwise. In SEM, Legendre polynomials $P_N(x)$ is used to choose the Largrange basis functions, where N is the polynomial order. The discrete points $\{\xi_i\}$ are the polynomial roots of $(1 - x^2)P'_N(x)$. These points are called the Gauss Lobatto Legendre (GLL) points, and the corresponding Lagrange polynomials can be defined as "GLL polynomials". Figure 3.1 shows a one dimensional GLL point along with the basis function. It can be seen that the functions becomes zero at other GLL points. The mesh has dense points close to the element boundary. Since the Lagrange polynomial is orthogonal, this leads to a diagonal or block diagonal "mass matrix", which is preferred in time domain computations due to that the inversion of such matrices are trivial.

The other advantage of using GLL points is that, it can be used to compute the numerical quadrature (A.1.5). Consider a GLL polynomial p of degree $\leq 2N - 1$, then the quadrature formula is given by:

$$\int_{-1}^{1} p(x)dx \equiv \sum_{j=0}^{N} \omega_j p(\xi_j), \qquad \xi_j \in [-1, 1], \tag{3.3}$$

where $\{\omega_j\}_{j=0}^{N}$ are quadrature weights given by

$$\omega_j = \frac{2}{N(N+1)} \frac{1}{[P_N(\xi_k)]^2} \tag{3.4}$$

Interpolation in one dimension can be extended to two or three dimensions by using tensor products. Figure 3.2 shows SEM meshes, constructed using GLL points. In case of deformed mesh, a reference element $\hat{\Omega} = [-1, 1]^d, (d = 2, 3)$ is used to define a mapping between the reference element and each element in the domain, i.e. $\mathbf{x}^e : \hat{\Omega} \rightarrow \Omega^e$. If the mesh is rectangular, then the transformation is affine, and the jacobian becomes a constant value. SEM in NEK5000 employs quadrilateral in two dimensions and hexahedral in three dimensions. Solving the partial differential equation in a finite computational domain Ω consist of spatial and temporal discretization. In the following section, spatial discretization that lead to a semi-discrete matrix form and temporal discretization is explained, along with fractional step method.

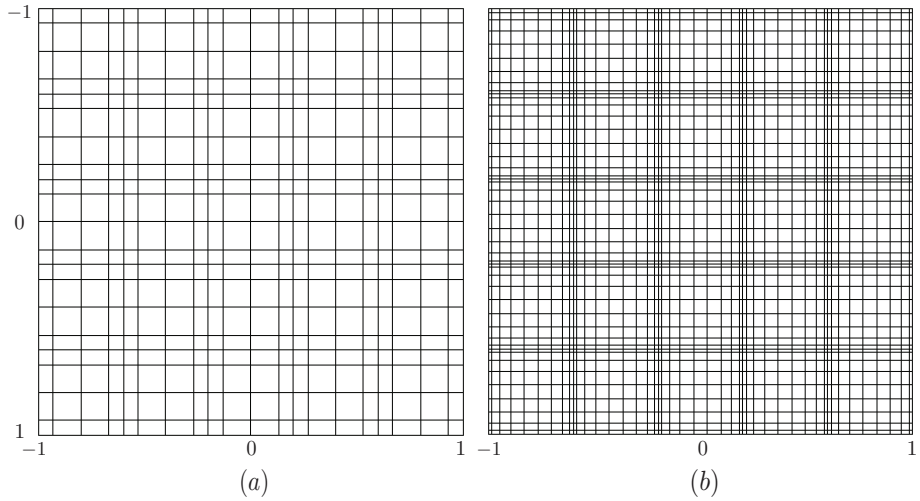

Figure 3.2: GLL mesh for a square domain $\Omega = [-1, 1]$ with $E = [5 \times 5]$, (a) $N = 5$ and (b) $N = 10$

3.3 Spatial discretization

3.3.1 Weak formulation

The strong form (A.1.1) of equation (2.2) is reduced to weak form (A.1.3), which allows us to use the Lagrangian basis functions along with the Galerkin method (A.1.4). That gives a spatial accuracy that is consistent with the order of the basis functions. In order to obtain the weak form, variational formulation is used. Equation (2.2) is multiplied with test functions $\mathbf{v} \in H^1(\Omega)^d$ and $q \in L^2(\Omega)$ then we integrate over Ω to obtain

$$\int_\Omega \mathbf{v} \cdot \frac{\partial u}{\partial t} d\Omega + \int_\Omega \mathbf{v} \cdot (\mathbf{u} \cdot \nabla \mathbf{u}) d\Omega = -\int_\Omega \mathbf{v} \cdot \nabla p d\Omega + \frac{1}{Re} \int_\Omega \mathbf{v} \cdot \nabla^2 d\Omega + \int_\Omega \mathbf{v} \cdot \mathbf{f} d\Omega \tag{3.5}$$

$$\int_\Omega q(\nabla \cdot \mathbf{u}) d\Omega = 0 \tag{3.6}$$

Integration by parts on the viscous and pressure terms then yields

$$\int_\Omega \mathbf{v} \cdot \frac{\partial u}{\partial t} d\Omega + \int_\Omega \mathbf{v} \cdot (\mathbf{u} \cdot \nabla \mathbf{u}) d\Omega = -\oint_{\Gamma_e} \mathbf{v} \cdot p n d\Gamma_e - \oint_{\Gamma_n} \mathbf{v} \cdot p n d\Gamma_n + \int_\Omega p(\nabla \cdot \mathbf{v}) d\Omega \tag{3.7}$$

$$+ \frac{1}{Re} \oint_{\Gamma_e} \mathbf{v} \cdot \nabla u \cdot n d\Gamma_e + \frac{1}{Re} \oint_{\Gamma_n} \mathbf{v} \cdot \nabla u \cdot n d\Gamma_n - \frac{1}{Re} \int_\Omega \nabla \mathbf{u} \cdot \nabla \mathbf{v} d\Omega$$

$$+ \int_\Omega \mathbf{v} \cdot \mathbf{f} d\Omega \tag{3.8}$$

$$\int_\Omega q(\nabla \cdot \mathbf{u}) d\Omega = 0$$

Later test functions $(V \times Z) \subset (H^1(\Omega)^d \times L^2(\Omega))$ for $(\mathbf{u}, p)$ are chosen such that the solution is sufficiently smooth and includes natural and essential (Dirichlet and periodic) boundary conditions. Trail functions are chose in space $\mathbf{v} \in V_0 = H_0^1(\Omega)^d$ and $q \in Z = L_0^2(\Omega)$ such that the boundary integrals that correspond to essential boundary conditions cancels. Natural boundary conditions are assumed to cancel the boundary integral $(\oint_{\Gamma_n})$ in the case they are used and the test functions are assumed to cancel the boundary integrals $(\oint_{\Gamma_e})$ for the essential boundary conditions. Considering all the conditions, then the "weak formulation" of the problem can be stated as:

Find $(\mathbf{u}, p) \in V \times Z$ such that:

$$\frac{d}{dt}(\mathbf{v}, \mathbf{u}) + \mathcal{A}(\mathbf{v}, \mathbf{u}, \mathbf{u}) = \mathcal{B}(\mathbf{v}, p) + \frac{1}{Re}\mathcal{C}(\mathbf{v}, \mathbf{u}) + \mathcal{F}(\mathbf{v}), \quad \forall \mathbf{v} \in V_0, \tag{3.9}$$

$$\mathcal{B}(\mathbf{u}, q) = 0 \qquad \forall q \in Z \tag{3.10}$$

Where

$$\frac{d}{dt}(\mathbf{v},\mathbf{u}) = \int_\Omega \mathbf{v}\cdot\frac{\partial u}{\partial t}d\Omega = \frac{d}{dt}\int_\Omega \mathbf{v}\cdot\mathbf{u}d\Omega$$

$$\mathcal{A}(\mathbf{v},\mathbf{u},\mathbf{u}) = (\mathbf{v},\mathbf{u}\cdot\nabla\mathbf{u}) = \int_\Omega \mathbf{v}\cdot(\mathbf{u}\cdot\nabla\mathbf{u})d\Omega$$

$$\mathcal{B}(\mathbf{v},p) = -(\nabla\cdot\mathbf{v},w) = -\int_\Omega(\nabla\cdot\mathbf{v})wd\Omega$$

$$\mathcal{C}(\mathbf{v},\mathbf{u}) = -(\nabla\mathbf{v}\cdot\nabla\mathbf{u}) = -\int_\Omega \nabla\mathbf{u}\cdot\nabla\mathbf{v}d\Omega$$

$$\mathcal{F}(\mathbf{v}) = (\mathbf{v},\mathbf{f}) = -\int_\Omega \mathbf{v}\cdot\mathbf{f}d\Omega$$

By Galerkin method choosing trial and test functions in the same Sobolev space that is built up by of Lagrangian interpolants. Then, the discrete sub-spaces is chosen in the following way $(\mathbf{u}_N, p_N) \in V_{0,N}\times Z_N \subset V_0\times Z, v\in V_{0,N}$ and $q\in Z_N$

Find $(\mathbf{u}_N, p_N)\in V_{0,N}\times Z_N$ such that:

$$\frac{d}{dt}(\mathbf{v}_N,\mathbf{u}_N) + \mathcal{A}_N(\mathbf{v_N},\mathbf{u_N},\mathbf{u_N}) = \mathcal{B}_N(\mathbf{v}_N,p_N) + \frac{1}{Re}\mathcal{C}_N(\mathbf{v}_N,\mathbf{u}_N) + \mathcal{F}_N(\mathbf{v}_N), \quad \forall\mathbf{v}_N\in V_{0,N} \tag{3.11}$$

$$\mathcal{B}_N(\mathbf{u}_N,q_N) = 0 \qquad \forall q_N\in Z_N \tag{3.12}$$

where

$$\begin{aligned}
\mathcal{A}_N(\mathbf{v_N},\mathbf{u_N},\mathbf{u_N}) &= (\mathbf{v}_N,\mathbf{u}_N\cdot\nabla\mathbf{u}_N)_{GLL},\\
\mathcal{B}_N(\mathbf{v}_N,p_N) &= -(\nabla\cdot\mathbf{v}_N,w_N)_{GLL},\\
\mathcal{C}_N(\mathbf{v}_N,\mathbf{u}_N) &= -(\nabla\mathbf{v}_N\cdot\nabla\mathbf{u}_N)_{GLL},\\
\mathcal{F}_N(\mathbf{v}_N) &= (\mathbf{v}_N,\mathbf{f}_N)_{GLL},\\
(\mathbf{v}_N,\mathbf{u}_N) &= (\mathbf{v}_N,\mathbf{u}_N)_{GLL},
\end{aligned}$$

Here the inner products on the form $(\cdot,\cdot)_{GLL}$ are computed with the GLL-quadrature rule, which includes all quadrature computations that include velocity and pressure. Computing $(\cdot,\cdot)_{GLL}$ on a collocated grid and staggered grid is called as $(\mathbb{P}_N\times\mathbb{P}_N)$ and $(\mathbb{P}_N\times\mathbb{P}_{N-2})$ method respectively. For more details about discretization,readers are suggested to refer [36, 37]

3.3.2 Semi-discrete matrix form

Reducing the Integral form to matrix form is the most convenient way to solve the set of equations. Here, we describe the steps for converting domain integrals to semi-discrete matrix form for a two dimensional non-deformed conformal grid. For more complicated grids the readers are suggested to refer [36, 37]. Consider a single element on a rectangular domain $\Omega = [0,L_1]\times ...\times[0,L_d]$, with $\{\phi_j\}_{j=0}^N$ Lagrangian interpolants and reference element $\hat{\Omega} = [-1,1]^d$.. Then an affine transformation $\mathbf{x}:\hat{\Omega}\to\Omega, (r_1,...r_d)\to(x_1,...d_d)$ is given by $\mathbf{x}(r_1,...,r_d) = ((L_1/2)(r_1+1),....,(L_d/2)(r_d+1))$. The quadrature nodes and weights of an integral approximation are given by $\{\xi_i\}_{l=0}^N\subset[-1,1]$ and $\omega_{l\,l=0}^N$ respectively.Also let $\mathrm{diag}(A_1,...A_m)$ represents a diagonal block matrix with the matrices $A_1,...,A_m$ through the diagonal.

The inner products of (3.12) are computed using (3.1) as :

$$(u,v)_N = \int_\Omega vud\Omega = \sum_{\hat{i}\hat{j}}\sum_{ij}\left(v_{\hat{i}\hat{j}}\int_\Omega \phi_{\hat{i}}\phi_{\hat{j}}\phi_i\phi_j dxdy\right)u_{ij} \tag{3.13}$$

Where $\bar{v} = v_{\hat{i}\hat{j}}$ and $\bar{u} = u_{ij}$ are vectors of basis coefficients obtained after affine transformation. A much simpler form of the inner product (3.13) is:

$$(u,v)_N = \bar{v}^T M\bar{u}, \tag{3.14}$$

where M is the so called "mass matrix" with the entries, after affine transformation:

$$M_{\hat{k}k} = \int_{-1}^{1}\int_{-1}^{1} \phi_i(r_1)\phi_{\hat{i}}(r_1)\phi_j(r_2)\phi_{\hat{j}}(r_2)\frac{L_1}{2}dr_1\frac{L_2}{2}dr_2 \tag{3.15}$$

$$= \frac{L_1L_2}{4}\left(\int_{-1}^{1}\phi_i(r_1)\phi_{\hat{i}}(r_1)dr_1\right)\left(\int_{-1}^{1}\phi_j(r_2)\phi_{\hat{j}}(r_2)dr_2\right)$$

$$\approx \frac{L_1L_2}{4}\left(\sum_{l=0}^{N}\rho_l\phi_{\hat{i}}(\xi_l)\phi_i(\xi_l)\right)\left(\sum_{l=0}^{N}\rho_l\phi_{\hat{j}}(\xi_l)\phi_j(\xi_l)\right) \tag{3.16}$$

$$\left\{\phi(\xi_j)=\delta_{ij}, \quad \hat{M}=\mathrm{diag}(\{\rho_0,\rho_1,...,\rho_N\})\right\} \tag{3.17}$$

$$= \frac{L_1L_2}{4}\hat{M}_{\hat{i}i}\hat{M}_{\hat{j}j} \tag{3.18}$$

where $L_1L_2/4$ is the constant Jacobian that corresponds to the affine mapping and $\hat{k}=1+\hat{i}+(N+1)\hat{j}$, $k=1+i+(N+1)j$ is is the ordering of the elements. Equation (3.18) written in tensor product form yields

$$M = \frac{L_1L_2}{4}\left(\hat{M}\otimes\hat{M}\right) \tag{3.19}$$

Where $\hat{M}$ is the one dimensional mass matrix and $\otimes$ is the tensor product.

The derivatives in the equation can be represented by the differential matrix ($\hat{D}$), which in one dimension is given by:

$$\hat{D}_{ij} = \left.\frac{d\phi_j}{dr}\right|_{r=\xi_i}, \qquad i,j\in\{0,1,...,N\}^2 \tag{3.20}$$

The derivative operator for two dimensions reads

$$D_1 = \left(I\otimes\hat{D}\right)\frac{2}{L_1}, \qquad D_2 = \left(\hat{D}\otimes I\right)\frac{2}{L_2}, \tag{3.21}$$

Stiffnes matrix ($\hat{K}$), of the equation in one dimensional form is given by:

$$\hat{K}_{ij} = \int_{-1}^{1}\left.\frac{d\phi_i}{dr}\right|_{r=\xi_j}\left.\frac{d\phi_j}{dr}\right|_{r=\xi_i}dr \approx \sum_{l=0}^{N}\hat{D}_{li}\rho_l\hat{D}_{lj}, \qquad i,j\in\{0,1,...,N\}^2 \tag{3.22}$$

The two dimensional operator for the stiffness matrix becomes

$$K = \frac{L_2}{L_1}\left(\hat{M}\otimes\hat{K}\right)+\frac{L_1}{L_2}\left(\hat{K}\otimes\hat{M}\right) \tag{3.23}$$

Now define

$$\mathbf{M}=\mathrm{diag}(M,....M), \quad \mathbf{K}=\mathrm{diag}(K,....K), \quad \mathbf{D}=[D_1...D_d], \tag{3.24}$$

We construct general matrices that represent all flow fields. Then the inner products of the discrete variational form (2.14) can be evaluated as follow

$$\mathcal{A}_N(\mathbf{v},\mathbf{u},\mathbf{u}) = (\mathbf{v},u\cdot\nabla u) \;= \bar{\mathbf{v}}^T\mathbf{C}(\bar{\mathbf{u}})\bar{\mathbf{u}} \tag{3.25}$$

$$\mathcal{B}_N(\mathbf{v},p) = -(\nabla\cdot\mathbf{v},p) \;= -\bar{\mathbf{v}}^T\mathbf{D}^T\bar{p} \tag{3.26}$$

$$\mathcal{C}_N(\mathbf{v},\mathbf{u}) = -(\nabla\mathbf{v},\nabla\mathbf{u}) = -\bar{\mathbf{v}}^T\mathbf{K}\bar{\mathbf{u}} \tag{3.27}$$

$$\mathcal{F}_N(\mathbf{v},\mathbf{u}) = (\mathbf{v},\mathbf{f}) \qquad\; = \bar{\mathbf{v}}^T\mathbf{M}\bar{\mathbf{f}} \tag{3.28}$$

This results in the following semi-discrete matrix form of the Navier-Stokes equations

$$\mathbf{M}\frac{d\bar{\mathbf{u}}}{dt}+\mathbf{C}(\bar{\mathbf{u}})\bar{\mathbf{u}}+\frac{1}{Re}\mathbf{K}\bar{\mathbf{u}}-\mathbf{D}^T\bar{p}=\mathbf{M}\bar{\mathbf{f}} \tag{3.29}$$

$$-\mathbf{D}\bar{\mathbf{u}}=0 \tag{3.30}$$

3.4 Time discretization

The temporal discretization which is widely used in NEK5000 is backward differentiation and extrapolation of order k (BDFk/EXTk) scheme. The order of time discretization is important for accuracy and stability. Complex equation like the Navier-Stokes require a higher order implicit temporal discretization to attain stability and accuracy. Since the equations include both velocity and pressure, the time advancement can hardly be done in a single equation. Instead so-called "splitting" methods are used, that decouple the velocity and pressure and solve the system in two steps. This procedure can be performed in several ways. In this thesis we restrict ourselves to shortly explain the methods included in the Nek5000 code, which are based on the fractional step method.

3.4.1 The BDFk/EXTk scheme

The k^{th} order implicit backward differentiating scheme is based Taylor expansion. Consider a equation of the form $dy/dt = f(y)$, then the BDFk scheme is given by:

$$\frac{1}{\Delta t}\sum_{t=0}^{k}\beta_k y^{n+1-i} \approx f(y^{n+1}) \tag{3.31}$$

where $\{\beta_i\}_{i=1}^{k}$ are BDF coefficients and Δt is the time-step size. From equation (3.31), it can be seen that the number of implicit relations to be solved are the same for different orders k. Hence, the computational cost does not depend on the choice of order. The term in Navier–Stokes discretization, when treated implicitly creates non-symmetric, non-linear system, which makes it difficult to solve. In turn a explicit method, which implements high order extrapolation on the non-linear terms including the advection part is used. The k^{th} order extrapolation (EXTk) of a general non linear term $f(y^{n+1})$ is given by

$$f(y^{n+1}) \approx \sum_{i=1}^{k}\alpha_i f(y^{n+1-i}) \tag{3.32}$$

where $\{\alpha_i\}_{i=1}^{k}$ is a set of extrapolation coefficients corresponding to the specific order of the scheme. Adding the BDFk and EXTk schemes together results in the BDFk/EXTk scheme

$$\frac{1}{\Delta t}\sum_{i=0}^{k}\beta_k y^{n+1-i} = \sum_{i=1}^{k}\alpha_i f(y^{n+1-i}) \tag{3.33}$$

Figure 3.3 shows the stability region of second and third order BDFk/EXTk schemes for the scalar equation $dy/dt = \lambda y$. It can be seen that the BDF3/EXT3 scheme does include more of the imaginary axis eigenvalues than the BDF2/EXT2 scheme. The BDFk/EXTk discretization applied to the semi-discrete equation (3.30) yields

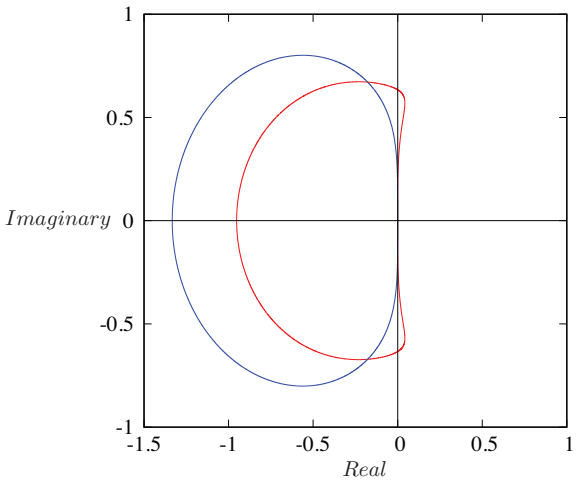

Figure 3.3: Stability regions of BDFk/EXTk methods. Red line and blue line corresponds to BDF3/EXT3 and BDF2/EXT2 respectively.

$$\mathbf{M}\frac{1}{\Delta t}\sum_{i=0}^{k}\beta_i\bar{\mathbf{u}}^{n+1-i} - \mathbf{D}^T\bar{p}^{n+1} + \frac{1}{Re}\mathbf{K}\bar{\mathbf{u}}^{n+1} = -\sum_{i=1}^{k}\alpha_i\mathbf{C}(\bar{\mathbf{u}}^{n+1-i})\bar{\mathbf{u}}^{n+1-i} + \mathbf{M}\bar{\mathbf{f}}^{n+1} \tag{3.34}$$

$$-\mathbf{D}\bar{\mathbf{u}}^{n+1} = 0 \tag{3.35}$$

Which is transformed into

$$\mathbf{H}\bar{\mathbf{u}}^{n+1} - \mathbf{D}^T\bar{p}^{n+1} = \mathbf{M}(\bar{\mathbf{f}}^{n+1} - \frac{1}{\Delta t}\sum_{i=1}^{k}\beta_i\bar{\mathbf{u}}^{n+1-i}) - \frac{1}{\Delta t}\sum_{i=1}^{k}\alpha_i\mathbf{C}(\bar{\mathbf{u}}^{n+1-i})\bar{\mathbf{u}}^{n+1-i} \tag{3.36}$$

$$-\mathbf{D}\bar{\mathbf{u}}^{n+1} = 0 \tag{3.37}$$

where $\mathbf{H} = \mathrm{diag}(H, ..., H)$ is the discrete Helmholtz operator defined as :

$$\mathbf{H} = \frac{1}{Re}\mathbf{K} + \frac{\beta_0}{\Delta t}\mathbf{M} \tag{3.38}$$

It is convenient to write (3.37) as a linear system. We get:

$$\begin{bmatrix} \mathbf{H} & -\mathbf{D}^T \\ -\mathbf{D} & 0 \end{bmatrix}\begin{bmatrix} \bar{\mathbf{u}}^{n+1} \\ \bar{p}^{n+1} \end{bmatrix} = \begin{bmatrix} \tilde{\mathbf{f}}^{n+1} \\ 0 \end{bmatrix} \tag{3.39}$$

where

$$\tilde{\mathbf{f}}^{n+1} = \mathbf{M}\left(\bar{\mathbf{f}}^{n} - \frac{1}{\Delta t}\sum_{i=1}^{k}\beta_i\bar{\mathbf{u}}^{n+1-i}\right) - \frac{1}{\Delta t}\sum_{i=1}^{k}\alpha_i\mathbf{C}(\bar{\mathbf{u}}^{n+1-i})\bar{\mathbf{u}}^{n+1-i} \tag{3.40}$$

This system of equation can be solved with the fractional step method.

3.5 The fractional step method

The most widely used decoupling method is the fractional-step method, which has a first order time error that can be improved to second order by pressure correction. Recall, we are given a system on the form:

$$\mathbf{H}\bar{\mathbf{u}}^{*} = \tilde{\mathbf{f}}^{n} + \mathbf{D}^T\bar{p}^{n} \tag{3.41}$$

by approximating the inverse $\mathbf{H}$ results in

$$\bar{\mathbf{u}}^{*} = \mathbf{H}^{-1}(\tilde{\mathbf{f}}^{n} + \mathbf{D}^T\bar{p}^{n}) \tag{3.42}$$

which is followed by a pressure correction step

$$\mathbf{E}\nabla^2\bar{p}^{n+1} = -\frac{1}{\Delta t}\mathbf{D}\bar{\mathbf{u}}^{*} \tag{3.43}$$

$$\bar{\mathbf{u}}^{n+1} = \bar{\mathbf{u}}^{*} + \Delta t\mathbf{M}^{-1}\mathbf{D}^T\nabla^2\bar{p}^{n+1} \tag{3.44}$$

$$\bar{p}^{n+1} = \bar{p}^{n} + \nabla^2\bar{p}^{n+1} \tag{3.45}$$

where $\mathbf{E} = \mathbf{D}\mathbf{M}^{-}1\mathbf{D}^T$ is a consistent Poisson operator for pressure.

3.6 DNS using NEK5000

3.6.1 Pipe mesh

The NEK5000 [35] employs a basic program called *genbox*, which helps to create spectral element mesh that consist of tensor-product arrays of elements. Considering a cylindrical pipe section to be used for study of straight and expansion pipe, *genbox* was used to create a two dimensional cylindrical mesh initially that consist of quadrilateral elements. Another program called *prenek* was used to edit the mesh to add refinement near the wall section. Figure 3.4(a, b, c) depicts three cylindrical meshes with different Elements (E) and polynomial order (N). It can be clearly viewed that the wall is well refined. Finally the two dimensional cylindrical mesh is extruded in the axial direction to form a three dimensional pipe as show in figure 3.4(d). The flow in the axial direction is driven by a pressure gradient, which is adjusted dynamically by the time-integration scheme to assure a constant mass flux is obtained. This method is used instead of a fixed pressure gradient. The basic idea is that the mean-flow is linear in the pressure gradient, which allows the pressure gradient to be adjusted in each time step in order to maintain a constant bulk velocity U_b.

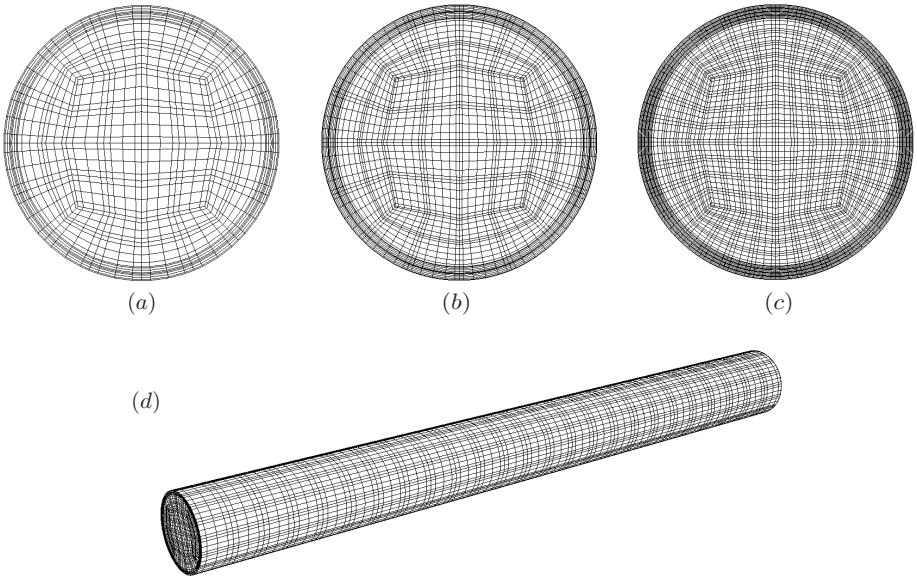

Figure 3.4: SEM mesh with quadrilateral elements for (a) E= 80, N=5, (b) E=80, N=7, (c) E=320, N=5 and (d) is the three dimensional view of the pipe

3.6.2 Computational resource

Since it is not possible to run big computation on desktop computer, all the computations presented here were carried out using the super computer facility at CRIHAN. For a single simulation a maximum of 1000 cores can be used for 24 hours.

Figure 3.5: CRIHANN Super computer facility.

3.6.3 Data visualization and post processing

Visulization of large data is not possible until a special file reader is used. VisIT (Visualization IT) provides a special file reader for NEK5000. All the contour plot show in the thesis were created using VisIT. For the case of post processing, data were dumped on to a specific output file and were analysed using special codes written using Python.

Chapter 4

Effect of tilt perturbation

4.1 Introduction

The flow in axisymmetric sudden-expansion pipe flow has been studied experimentally [16, 19, 38, 39] and numerically [21, 22]. The expansion pipe consist of a small inlet d and a larger outlet diameter D. In general, the inlet diameter d is used as the length scale to define the Reynolds number $Re = Ud/\nu$, where U is the mean flow velocity and ν is the kinematic velocity. The flow inside the expansion pipe initially separates in the expansion region and reattaches downstream, there by forming a recirculation region. This region grows linearly in the axial direction as the Re is increased. Once a critical Re is exceeded, the recirculation region becomes asymmetric and breaks. In experiments, the recirculation region loses symmetry at $Re \simeq 1139$ [19] and then breaks to form localised turbulence that occupies a stable spatial position [38]. In terms of global stability analysis, [21] have shown that the symmetry breaking occurs after a critical Reynolds number of ≈ 3273. The reason for the early occurrence of transition is believed to be due to experimental imperfections. The imperfections gets amplified as the Re increases and creates a by-pass to the turbulent regime. In numerical simulation these imperfections are very small and the transition to turbulence occurs at much higher Re when compared to experiments. In order to trigger turbulence a numerical finite amplitude perturbation is added to the system, which in turn creates the by-pass that helps to reach the turbulent regime. This process of adding finite amplitude perturbation can be explained via system dynamics, as show in figure 4.1.The green line in the figure correspond to a laminar regime, which is an attractor, i.e., any infinitesimal perturbation to the system decays and system remains laminar. The transition to turbulence only occurs only when the critical Re is reached. In case of expansion pipe flow this not possible and it is explained in the following sections. When a finite amplitude perturbation δ is added to the laminar system, the system takes a bypass (dotted lines) to the turbulent regime. This early transition to turbulence depends upon the amplitude δ of the perturbation, higher the perturbation, earlier is the transition. Numerical simulations with an applied imperfection [22] found the transition to turbulence to occur at $Re \approx 1800$. The goal of the present study is to numerically simulate a gradual expansion (diverging) pipe flow with a finite amplitude imperfection added to the system that could trigger early transition to turbulence. The long-term motivation of this study is to understand the effect of the perturbation on the system and

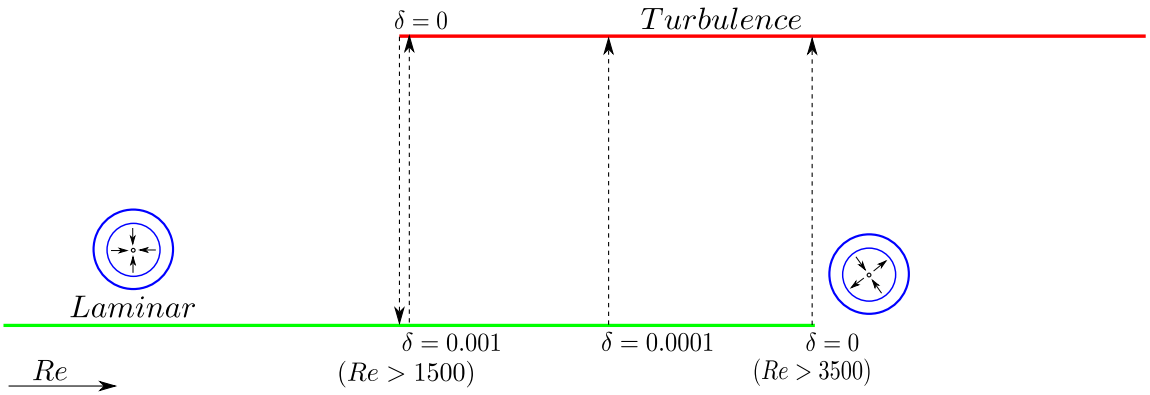

Figure 4.1: System dynamics view of the expansion pipe flow system with finite amplitude perturbation

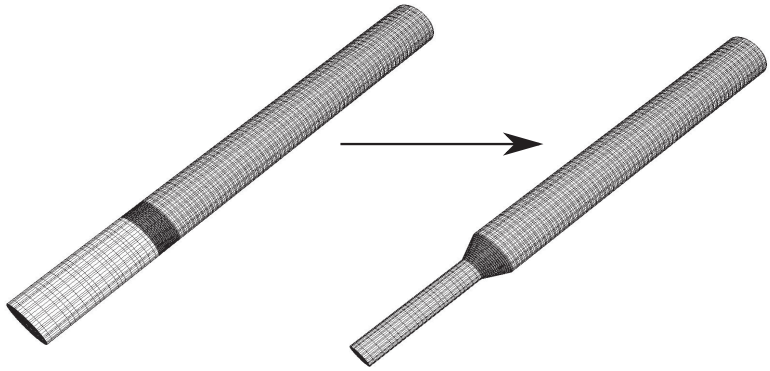

Figure 4.2: Morphing of a straight pipe mesh to a gradual expansion pipe

how the localized turbulence gains energy to sustain in a constant spatial position. In the first part, the numerical method and its computational grid validation are presented. In the second part, the results for the asymmetric growth of the recirculation are discussed, along with the oscillation of the flow, the time evolution of the localised turbulence, and observations of decay of the turbulent structure.

4.2 Numerical method

The unsteady incompressible Navier-Stokes equation for a viscous Newtonian fluid is solved using NEK5000 (SEM) as discussed in chapter 3.The Navier-Stokes equation is recollected here for the convince of the reader and to explain the application of boundary condition:

$$\nabla \cdot \boldsymbol{v} = 0 \tag{4.1}$$

$$\frac{\partial \boldsymbol{v}}{\partial t} + \boldsymbol{v} \cdot \nabla \boldsymbol{v} = -\nabla P + \frac{1}{Re}\nabla^2 \boldsymbol{v}, \tag{4.2}$$

where $\boldsymbol{v} = (u, v, w)$ and P denote the scaled velocity vector and pressure respectively. The equations (4.1) and (4.2) were non-dimensionalised using the inlet pipe diameter, d, for the length scale and the mean velocity at the inlet, u, for the velocity scale. The time scale and the pressure scale are therefore $t = d/u$ and ρu^2, Where ρ is the density of the fluid. The equations are solved with the boundary conditions

$$\boldsymbol{v}(\boldsymbol{x}, t) = 2(1 - 4r^2)\boldsymbol{e}_z\,, \tag{4.3}$$

$$\boldsymbol{v}(\boldsymbol{x}, t) = 0\,, \tag{4.4}$$

$$P\boldsymbol{n} - \boldsymbol{n} \cdot \nabla \boldsymbol{v}(\boldsymbol{x}, t)/Re = 0 \tag{4.5}$$

corresponding to a fully developed Hagen-Poiseuille flow (4.3) at the inlet, no-slip at the walls, and a stress free outflow (4.5) condition at the outlet of the pipe, where $\boldsymbol{x} = (x, y, z)$ is the position vector and $\boldsymbol{n}$ denotes the normal vector. The flow was initialised with Poiseuille in the inlet section and each simulation was computed using 512 cores. In order to create a gradual expansion pipe, initially a straight pipe was created. The straight pipe mesh is later morphed using a simple mathematical model. The equation for scaling factor S to morph the domain is given as:

$$S = \begin{cases} 1, & z < E_{in}, \\ 1 + \frac{(D-1)(z-E_{in})}{E_{out}-E_{in}}, & E_{in} < z < E_{out}, \\ D, & z > E_{out}. \end{cases} \tag{4.6}$$

$$x = S \times x \tag{4.7}$$

$$y = S \times y \tag{4.8}$$

Where E_{in}, E_{out} are the axial position of the inlet and outlet of the expansion section respectively. D is the outlet diameter of the pipe. Figure 4.2 show a small pipe of length $25d$ morphed into a gradual

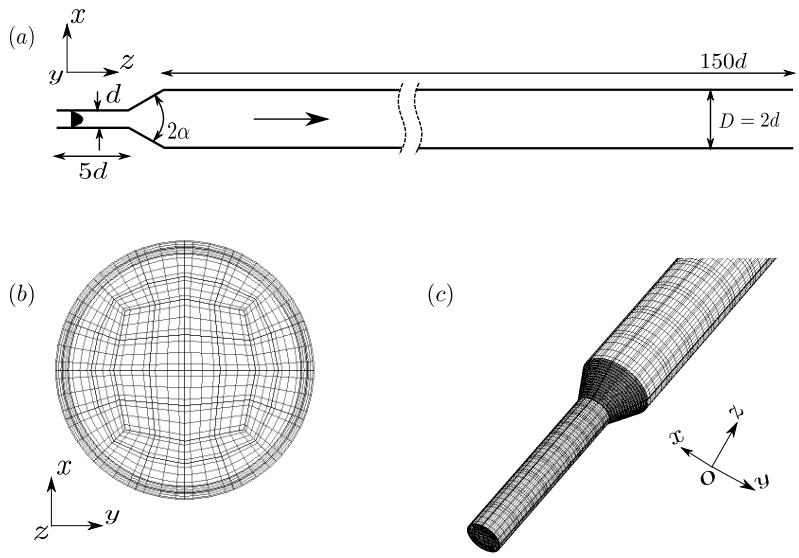

Figure 4.3: The spectral-element mesh used in the present study with a divergent angle of $\alpha = 26.57°$. (a) Sketch of the domain, (b) cross-section of the mesh (dark lines represent the elements and the grey lines represent the Gauss-Labatto-Legendre points) and (c) a three-dimensional view of the mesh near the diverging section. The mesh is made of $K = 14\,400$ elements.

expansion pipe. Here the length of the expansion section is $1d$. The equations were solved using an open source code nek5000 developed by [40]. Spatial discretisation is based on the spectral element method using Legendre polynomials. The equations are reduced to a weak form and discretised in space by Galerkin approximation. N^{th} order Lagrange polynomial interpolants on Gauss-Labatto-Legendre points were chosen as the basis for the velocity space, similary for the pressure space. In all the simulations $\mathbb{P}_N - \mathbb{P}_N$ formulations were implemented. The time-stepping in nek5000 is semi-implicit in which the viscous term of the Navier-Stokes equations are treated implicitly using third order backward differentiation and the non-linear terms are treated by a third order extrapolation scheme. The gradual expansion pipe as shown in figure 4.3 consists of three parts (1) the inlet, (2) the diverging section and (3) the outlet. The velocity field is simulated in the Cartesian coordinate system (x, y, z). The expansion ratio is $E = D/d = 2$. The length of the divergent section is kept constant in this study and of length d, which leads to a divergence half-angle $\alpha = 26.57°$. The length of the inlet pipe is $5d$ and the outlet pipe length is $150d$. The computational mesh was constructed using hexahedral element, with fine refinement near the wall and the expansion section. This was done to perfectly resolve the sensitive flow separation and reattachment point. The (x, y) cross-section contains 80 elements and 175 element in the z direction. The total number of grid point in the computational domain can be calculated using KN^3, where K is the number of element and N is Legendre polynomial order. In order to find the proper size of the computational domain, simulations were carried out keeping the value of E constant and changing the value of N. Table 4.1 shows the length of the recirculation region for different orders of polynomial at $Re = 1000$. Here, flow reattachment point, z_r, and the viscous drag $(\rho U^2/2)\mathcal{A}_w C_f$, where $\mathcal{A}_w$ is the surface area of the outlet pipe wall and C_f is the friction coefficient are used as criteria to check for convergence. The reason for using length of the recirculation region z_r as criteria because it is very sensitive to the resolution of the separated shear layer, particularly near the separation point. It can seen from 4.1 that the polynomial order of $N = 5$ is sufficient to resolve the flow accurately. This value of N and the mesh have been used in all the following simulations presented in this chapter. The polynomial order of $N = 5$, along with $K = 14\,000$ leads to a mesh of size $\approx 1.8 \times 10^6$ grid points. The total number of grid points in the simulation is approximately KN^3. The flow was initialised with Poiseuille in the inlet section and each simulation was computed using 512 cores. Table 4.1 shows the length of the recirculation region for different orders of polynomial at $Re = 1000$. The mesh convergence study was carried out by changing the polynomial order N of the Legendre polynomial, of the spectral elements. The observations used to assess convergence are the flow reattachment point, z_r, and the viscous drag $(\rho U^2/2)\mathcal{A}_w C_f$, where $\mathcal{A}_w$ is the surface area of the outlet pipe wall and C_f is the friction coefficient. The length of the recirculation region depends sensitively on the resolution of the separated shear layer, particularly near the separation point. The

N	Reattachment Position z_r	Viscous Drag
3	43.68	0.8430
4	43.65	0.3566
5	43.58	0.3419
6	43.59	0.3418
7	43.58	0.3419

Table 4.1: Convergence study, changing the order of polynomial N. z_r is the length of the recirculation region in the pipe for $Re = 1000$.

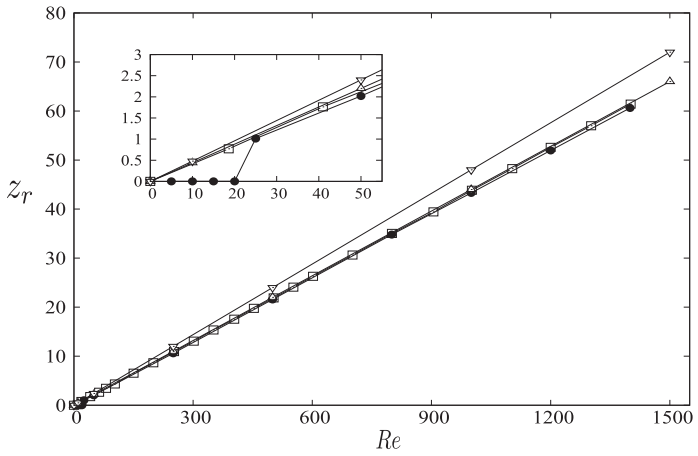

Figure 4.4: (a) Streamline of the recirculation region of length z_r inside the diverging pipe at $Re = 300$. (b) Recirculation region length, z_r, with respect to Re. ($\bullet$) corresponds to best-fit proportionality given by $2z_r/d = 0.0866Re$ for present case. ($\square$) corresponds to $2z_r/d = 0.0874Re$ [20], ($\triangle$) and ($\triangledown$) corresponds to experimental result [16, 39] $2z_r/d = 0.088\ Re$ and $2z_r/d = 0.096Re$ respectively for sudden expansions.

polynomial order of $N = 5$ is sufficient to resolve the flow accurately. This value of N and the mesh have been used in all the following simulations, which corresponds to $\approx 1.8 \times 10^6$ grid points. To further validate the accuracy of the simulations, the growth of the recirculation as a function of the Reynolds number is shown in figure 4.4.The simulations show that the extent of the recirculation region is of the form $2z_r/d = 0.0866Re$, which agrees well with previous studies for sudden expansion flow. Unlike the sudden expansion flow, for a gradual expansion pipe, the onset of recirculation occurs after a critical flow velocity. From the inset in figure 4.4 it can be seen that initially the value is zero and after a critical Re the recirculation region starts to occurs, this depends upon the divergence half-angle α and Re [23]. The figure 4.5 are contour plots of axial velocity. For $Re = 10$ the streamlines inside the domain are straight, indicating there is no recirculation region. In case of $Re = 100$, the recirculation can be seen close to the expansion section.

4.3 Finite amplitude perturbation

According to stability theory, the first bifurcation in expansion pipe flow occur at very high Re. To numerically simulate this Re, we need a very long computational domain, which is not possible with the present computational resource. Even if we could build domain to run high Re, the growth of the unstable mode will be slow and would require a very long computational time to achieve onset of turbulence. In order to overcome this problem of computing long domain, a finite amplitude perturbation is added to system that creates a bypass to turbulence regime. For sudden expansion pipe flow, numerical simulations [20, 21] have shown that the flow is unstable to infinitesimal perturbations for $Re \approx 3273$, but the transition in experiments occurs at much lower Re [16, 19, 38]. The exact nature of the observed instability is therefore unclear. The small deformation or imperfection creates perturbation in the flow that gets amplified due to convective instability mechanism, which leads to time-dependent solutions. Numerical results [20], have shown that small perturbation get amplified by transient growth in the sudden expansion for $Re \leq 1200$, advect downstream and decays. In the present computational domain,

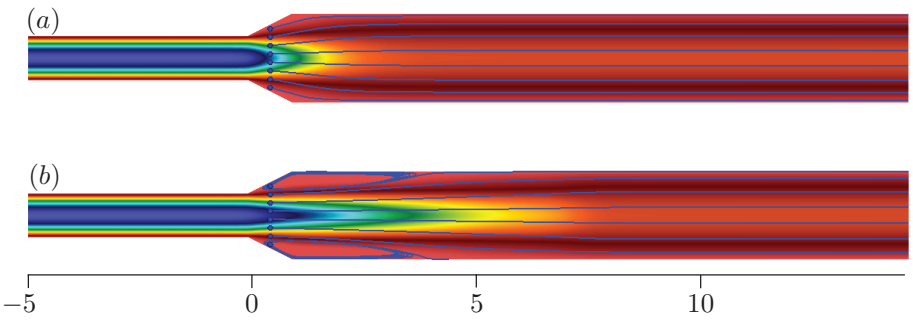

Figure 4.5: Contour plot of axial velocity with streamlines for showing the length of recirculation region (*a*) $Re = 10$, shows there is no recirculation region and (*b*) $Re = 100$.

the flow is linearly stable up to $Re \gtrsim 2200$, i.e., the flow is laminar. For larger Re the recirculation bubble extends close to the end of the outlet section and cannot be calculated reliably. In order to trigger turbulence as discussed above, we added a finite amplitude perturbation at the inlet of expansion pipe flow. The finite amplitude perturbation is applied along with the Hagen-Poiseuille flow in the form:

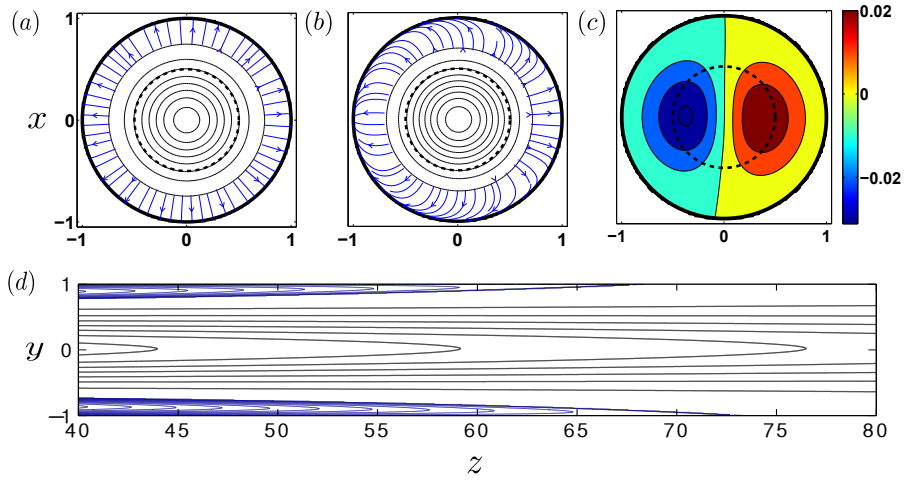

Figure 4.6: Cross-sections of the pipe. Contour line plots of the axial velocity (solid black lines) taken at $z = 22.5d$ for (*a*) $Re = 1000$ and (*b*) $Re = 1600$. The dashed line corresponds to the inlet pipe diameter and the blue lines with arrows represent the crosswise velocities within the recirculation region. (*c*) Contour plot of the perturbation, i.e., flow with perturbation ($\delta = 0.001$) subtracted from the base flow ($\delta = 0$) for $Re = 1600$. (*d*) Streamwise cross-section of the flow around the reattachment point at $Re = 1600$ with $\delta = 0.001$.

$$u(\boldsymbol{x}, t) = 2(1 - 4r^2)\boldsymbol{e}_z + \delta \boldsymbol{e}_y \,, \tag{4.9}$$

where δ is the finite-amplitude applied to crosswise velocity.

The addition of the perturbation (4.9) distorts the flow, nudging it in the direction of the crosswise direction. In all the simulations presented in this chapter, a fixed value of $\delta = 0.001$. Figure 4.6(*a*-*c*) shows cross-sections of the pipe at $z = 22.5d$ from the expansion section. Thick dark lines shows contours of the axial velocity, where the thick dotted line represents the diameter of the inlet section and the blue lines with arrows shows the region of recirculation region. At low Re the flow remains axisymmetric as show in Figure 4.6(*a*), which corresponds to $Re = 1000$. when $Re = 1600$, the flow inside the pipe starts becoming asymmetry because of the nudging perturbation as show in figure 4.6(*b*). It can be identified by comparing the solid and dashed lines. In to order to clearly understand the effect of perturbation on the flow, an initial computation without perturbation (baseflow) is done. This baseflow solution is subtracted from a perturbed flow solution for the same value of Re. The result of subtraction is show in figure 4.6(*c*) and it can be seen that low is accelerates on the right-hand side of the pipe section and decelerates on the opposite side. To further quantify this, cross section in the axial plane is shown in

figure 4.6(d), it can be seen that recirculation region is asymmetry. This reattachment pattern is very sensitive to the form of the perturbation given at the inlet, which motivates the application of a simple form of disturbance.

4.4 Growth and Oscillation

Asymmetry growth of the flow in figure 4.6(a) can be measured by calculating position of the centroid of the axial velocity from the centre point of the pipe. The axial velocity is projected on to a Cartesian circular grid (x, y).
The moment of the function in x and y direction is given by:

$$M_x = \sum_x xv(x,y) \qquad M_y = \sum_x yv(x,y) \tag{4.10}$$

$$M = \sum_x \sum_y v(x,y) \tag{4.11}$$

Then the position of the centroid $(\bar{x}, \bar{y})$ is:

$$\bar{x} = \frac{M_x}{M} \qquad \bar{y} = \frac{M_y}{M} \tag{4.12}$$

Then square distance of the centroid from the centre of the pipe is:

$$\varepsilon = \bar{x}^2 + \bar{y}^2 \tag{4.13}$$

The square of this distance is denoted by ε ([19]). Figure 4.7(a) shows ε as a function of Re with least-square fit on the data obtained. It can be seen that at low Re there is no variation in the position of the centroid, a steady symmetric state is observed for $Re < 912$. As Re increases, a symmetry-breaking bifurcation occurs at a critical $Re_c = 912$. This value is smaller than the case of sudden expansion pipe ($Re_c = 1139$ in the experiment by [19]). Clearly, the critical Re depends on the position of the cross-section, α and δ. The value of ε increases linearly ($912 < Re < 1500$) forming a steady asymmetric state, with biased growth in the recirculation region. The magnitude of the symmetry deviation grows as the square root of Re, typical of supercritical bifurcation. The error bars in figure 4.7(a) represent the amplitude of the fluctuations in ε.

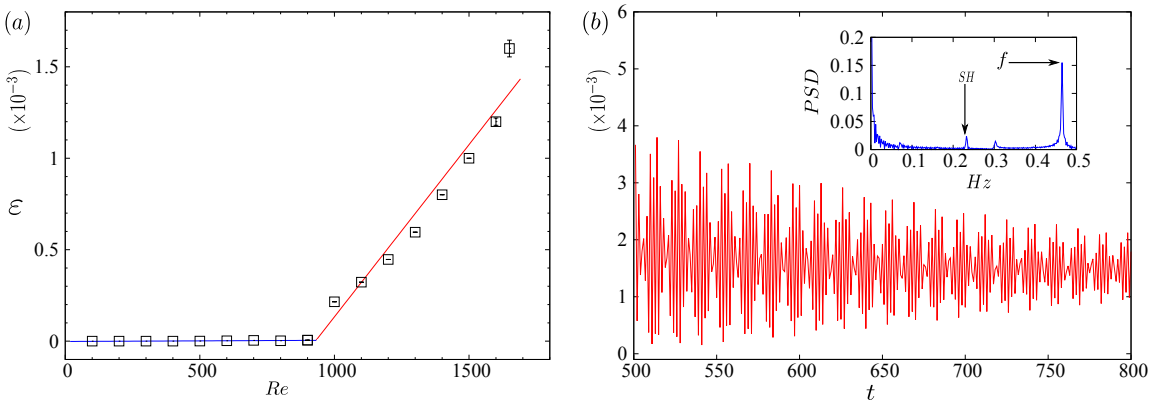

Figure 4.7: (a) Asymmetry growth of the flow measured by the square of the distance of the centroid from the centre of the pipe, ε, as a function of Re. The lines are least-square fit of the data and the intersection of the lines is at $Re_c = 912$ for the estimate of symmetry breaking bifurcation point. (b) Oscillations of ε at $Re = 1650$ as a function of time. The inset is the fast Fourier transform of the signal with a fundamental frequency $f = 0.468$ and a period doubling sub-harmonic $SH = 0.234$.

As the Re is increased further ($1500 \leq Re \leq 1650$), the flow becomes time dependent. The position of the centroid starts varying, due to the oscillation of the reattachment point downstream [38]. These oscillations are also observed in experiments of sudden expansion flow [19]. Figure 4.7(b) shows the value of ε as function of time, it can be seen that it exhibits quasi-periodic oscillations in the shear

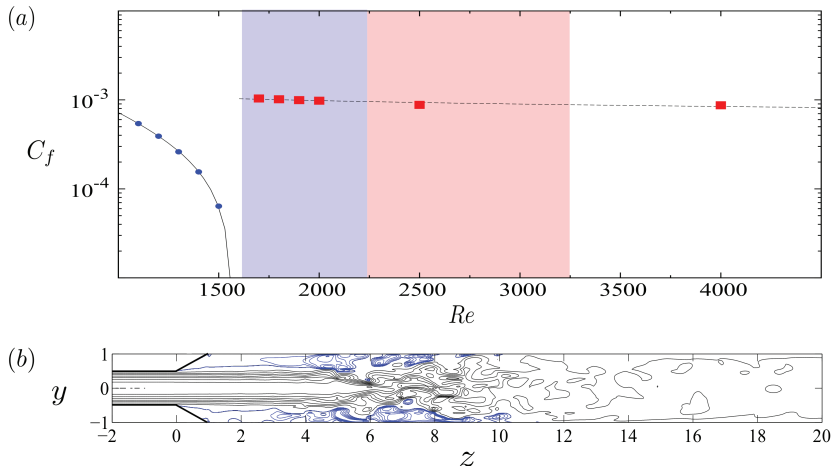

Figure 4.8: (a) Plot of friction coefficient, C_f, with respect to Re. The (blue) filled-circles represent the steady laminar asymmetric flow; the (red) filled-squares represent unsteady localised turbulent state. The continuous line represents the fit for the laminar state: $C_f = 1.97/Re - 0.0012$ and the dotted line represents a fit for localised turbulent state: $C_f = 0.0066(Re \times E)^{-0.22}$. The shaded regions $1650 \lesssim Re \lesssim 3273$ is the hysteretic regime, where the blue subsection indicates the extent of the regime explored on the laminar branch. (b) Contour plot of streamwise velocity of localised turbulence at $Re = 1680$ with $\delta = 0.001$.

layer around the recirculation region. Fast Fourier Transform (FFT) was performed on the signal to identify the dominating frequency. The inset in figure 4.7(b) is the FFT of the signal as a function of frequency, where $f = 0.468$ and $SH = 0.234$ a period doubling sub-harmonic. f seems to correspond to the frequency of vortex shedding around a circular body, which occurs due to the Kelvin-Helmholtz instability [41, 42]. This frequency of oscillation depends upon the type of the perturbation added to the system [32, 43]. Once the Re goes higher, the recirculation region to become turbulence.

4.5 Hysteresis

In order to measure the onset of turbulence, the skin friction coefficient, C_f are calculated on the whole domain. Figure 4.8(a) shows the friction coefficient, C_f, as a function of Re. At low Re, the flow is steady and asymmetric and the value of C_f decreases. The negative value in the skin friction coefficient is due to the presence of recirculation region, which extends up to approximately half the of the outlet section before transition. Around the transition Reynolds number, $Re_t \simeq 1680$, the recirculation region inside the pipe breaks and leads to a localised turbulent state, which can be seen by the sudden rise in the value of C_f and the axial velocity contours is shown in figure 4.8(b).

The turbulence that occurs, takes a constant spatial position inside the domain, near to the sudden expansion section [22, 38]. The formation of turbulence, near the diverging section, increases C_f due to higher internal mixing and resulting shear at the boundary. In this regime, C_f values scale roughly with the same exponent as the Blasius friction law, even though straight pipe flow are not turbulent at these Re. The present calculations for the perturbed flow were run up to $t = 600$ and the localised turbulence remained present. The perturbation was then removed and the flow was simulated up to $t = 1200$. The turbulence was observed to be self-sustained, and to occupy the same spatial position. The behaviour of system the whole system is explained using figure 4.8(a). The gradual expansion pipe without perturbation creates steady, symmetric solution until $Re < 2200$, beyond that the numerical simulation creates outlet boundary condition problem because of the recirculation region extending close to the outlet section. Once the perturbation is added, at low Re the solution is steady and asymmetric. After $Re > 1680$, the flow becomes turbulent. The range of Re in which laminar state as well as turbulent state co-exist is denoted by blue shade ($1650 \lesssim Re \lesssim 2200$). Since the recirculation region is broken, the simulation can be extended up to a very high Re. Global stability analysis [21] have revealed that the first bifurcation for the sudden expansion pipe occurs at $Re \gtrsim 3273$ above which natural transition can be expected without any added perturbation. Given the much larger computational cost and that we have already computed a range of Re, where the laminar and turbulent flows co-exist, we have not pursued the linear instability. To analyse the relaminarisation of the gradual expansion pie flow,

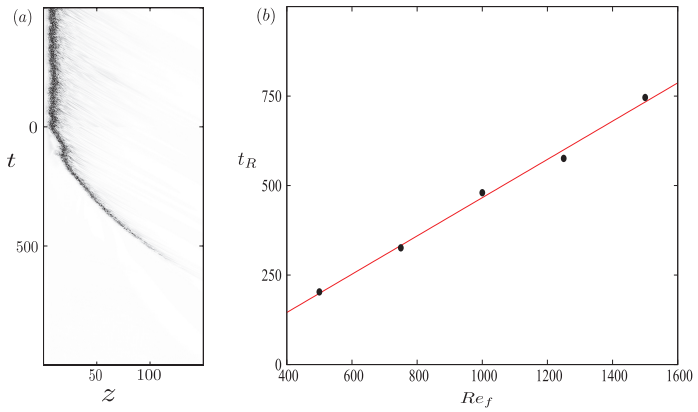

Figure 4.9: Relaminarisation study. (a) Spatio-temporal diagram (same legend as figure 4.10) of localised turbulence decay from $Re_0 = 2000$ to $Re_f = 1500$. (b) Relaminarization time, t_R, versus Re_f.

simulations were performed, where localised turbulence was generated at $Re_0 = 2000$ and the decay to laminar flow observed for Re below Re_t. In figure 4.9(a), the spatio-temporal diagram shows a typical relaminarisation case. At $t = 0$, Re is reduced suddenly from $Re_0 = 2000$ to $Re_f = 1500$. Here, the localised turbulence detaches from the inlet section almost immediately, then convects downstream and simultaneously decays, which can be seen as the disappearance of the vortical structures [17, 44]. The relaminarisation time, t_R, was obtained by monitoring the time taken for the total energy in the computational domain to fall below a threshold of 10^{-6}. Above $Re_f = 1500$ the turbulence leaves the computational domain before falling below the threshold. The figure 4.9(b) shown t_R as a function of Re_f. The straight line fit indicates that the decay time of the turbulence increases linearly for $Re < 1500$, as identified in experiments [23]. Here, no significant period of time was observed before the detachment of turbulence from the walls. Simulations were not carried out within the hysteresis region due to high computational cost. For these Re the turbulence is self-sustained for some time before detachment from the inlet section, and the time before detachment is expected to diverge rapidly as in uniform pipe flow [8].

4.6 Higher Reynolds number

Simulations were carried out at high Re to study how the onset of the localized turbulence occurs and it's dynamics. The spatio-temporal diagrams show in figure 4.10 corresponds to (a) $Re = 4000$, (b) $Re = 3000$, (c) $Re = 2000$ and (d) $Re = 5000$. The horizontal axis represents the centre axis of the pipe from the diverging section to the outlet. The streamwise vorticity value has been normalised with the maximum vorticity and been plotted with the same scale for comparison purposes. Initially at $Re = 2000$, the turbulence onsets at $t = 25$ and moves downstream, at $t = 100$ the turbulence starts moving upstream towards the diverging section and finally holds a stable position $z/d \simeq 10$. For $Re = 5000$, the onset of turbulence nearly occurs at the same time as that of $Re = 2000$, but the amount of time it takes to reach a localised position is $t = 40$, which is much smaller than that of the $Re = 2000$. The time taken to hold a stable position decreases as Re increases. The velocity trace downstream the localised turbulence for $Re = 2000$ recovers laminar flow (see figure 4.10(e)). In the case of $Re = 5000$, the flow downstream the intense region of turbulence exhibits inhomogeneous patterns. This is due to presence of high inertial force, compared to viscous force that damps the turbulence back to laminar state. The streamwise velocity trace (see figure 4.10(f)) suggests weak turbulence, that does not return to laminar flow and eventually could lead to puff splitting [8, 9]. This property of expansion flow with laminar inlet profile forming localised turbulence and decaying in the outlet section is in good relation with experiments [23].

4.7 Coherent structures

Structure within the localised turbulence is further studied using spatial correlations, which have been used to identify fast and slow streaks that dominate the coherent structures within puffs in pipe flow

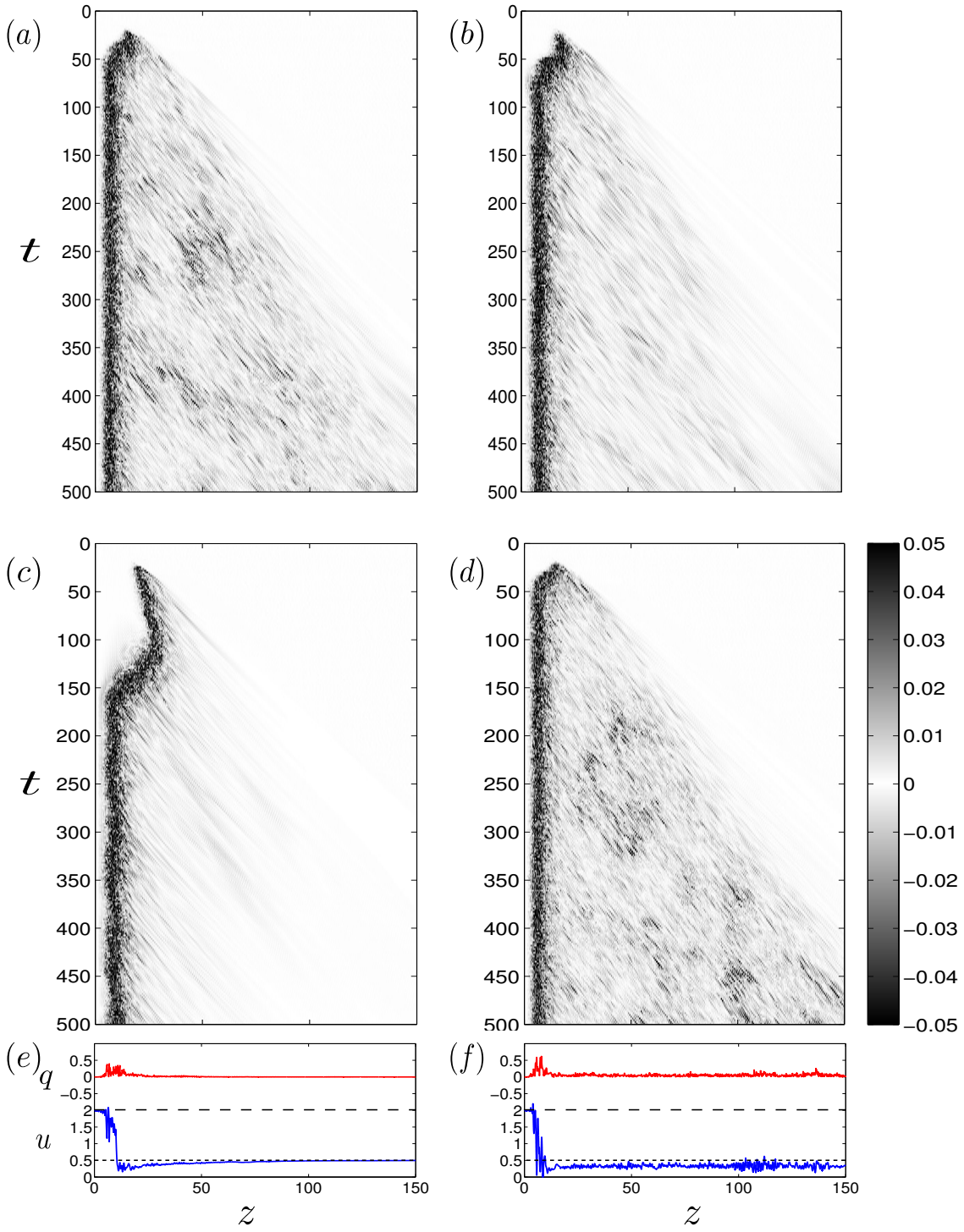

Figure 4.10: Evolution of localised turbulence. Spatio-temporal diagram of streamwise vorticity along the centreline of the pipe, where $z = 0$ corresponds to the start of the diverging section, for (a) $Re = 4000$, (b) $Re = 3000$, (c) $Re = 2000$ and (d) $Re = 5000$. (e) and (f) $q^2 = v^2 + w^2$ in (red) and streamwise velocity u (blue) at the final time step of (c) and (d). The dashed lines represent the Poiseuille centreline velocity in the inlet and the outlet sections.

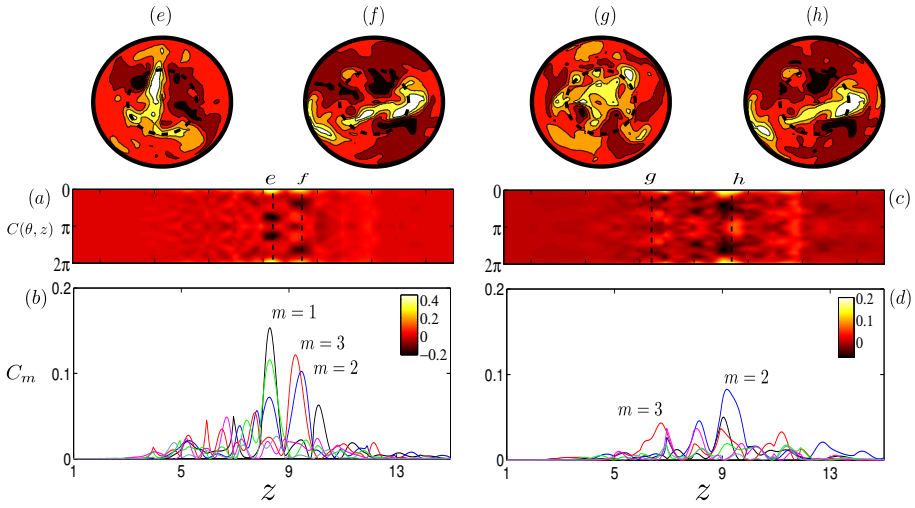

Figure 4.11: Spacial correlation on streamwise velocity of localised turbulence at $Re = 2000$. Contour of correlation, $C(\theta, z)$, at (a) $r = 0.5d$ and (c) $r = 0.8d$. Projection function of $C(\theta, z)$ for different azimuthal wave number m at (b) $r = 0.5d$ and (d) $r = 0.8d$. $(e - h)$ Cross-sections of the axial flow relative to the time averaged profile with fast flow (light/white) and slow flow (dark/red) taken at the corresponding vertical dashed lines.

[6]. The correlation in the streamwise velocity is obtained using the function:

$$C(\theta, z) = \left[\frac{2 \langle u_z(\theta + \phi, z) u_z(\phi, z) \rangle_\phi}{\langle \max(u_z)^2 \rangle_t} \right]_r \tag{4.14}$$

where $\langle \cdot \rangle_s$ indicates averaging over the subscripted variable, u_z is the instantaneous axial flow velocity and r is the radial position. The signature of structures of a particular azimuthal wavenumber m is obtained by projecting the correlation function, $C_m(z) = 2 \langle C(\theta, z) \cos(m\theta) \rangle_\theta$ [6]. Figure 4.11(a,b) shows the correlation at $r = 0.5d$ and it can be seen that the $m = 1$ mode dominates the flow. Whereas in figure 4.11(c,d) at $r = 0.8d$, the $m = 2$ structure dominates the flow along with $m = 3$ with a much smaller correlation value, which suggests that the flow is more active in the centre region than near to the walls. Overall this analysis points out that the localised turbulence in the gradual expansion possess a different flow structure from the turbulent puff [5, 6, 45] where $m = 3$ and 4 dominate the flow near to the wall. The cross-sections in figure 4.11(e-h) indicate slow and fast moving flow.

4.8 Conclusions

Numerical results for the flow through a circular pipe with a gradual expansion in presence of an imperfection have been presented in this chapter. The small imperfection leads to a linear asymmetry growth of the recirculation region, which has also been observed in experiments of sudden expansion pipe flow. As Re is increased, the long recirculation region oscillates seemingly due to shear Kelvin-Helmoltz instability [19, 38]. This time-dependent motion lies in a narrow range of Re for the amplitude studied here ($\delta = 10^{-3}$). From $Re_t \approx 1680$, the flow with the imperfection triggers localised turbulence in the outlet section of the pipe. For $Re > Re_t$ a route to the subcritical turbulent flow is established, and remains unchanged if the small perturbation is removed. Thus the flow through a perfect gradual axisymmetric expansion in a pipe exhibits multiplicity in the solution set of the Navier-Stokes equations, where both axisymmetric states and turbulent motion coexist over a range of Re. Above $Re_t \simeq 1680$, the turbulent flow is expected to have a lifetime that increases significantly. The system therefore exhibits hysteresis behaviour if Re is increased beyond critical for linear instability and then reduced below this value, until $Re \approx 1650$. This property of localised turbulent flow with laminar inlet profile forming localised turbulence and decaying in the outlet section agrees with experiments [23, 38]. The localised turbulence does not convect downstream but holds a stable spatial position. The structure within the localised turbulence is further studied using spatial correlations, which identifies fast and slow streaks that dominate the coherent structures. The main finding is that flow is more active in the centre region than near to the walls. Hence, it is important to note that the localised turbulence observed here has different structure from that of a turbulent puff in uniform pipe flow [6].

Chapter 5

Effect of vortex perturbation

In the previous, we studied pipe flow with gradual expansion with small tilt perturbation at the inlet. Here, we return to simple case of sudden expansion with vortex perturbation, to study the effect of perturbation. Direct numerical simulations for incompressible viscous fluid in a expansion pipe flow with a finite amplitude perturbation at inlet is presented in this chapter. The perturbation in the form of a vortex with its axis parallel to the axis of the pipe, is applied along with Hagen-Poisueille flow. At sufficiently high Reynolds numbers the recirculation region breaks into a turbulent patch that changes position axially depending on the strength of the perturbation. This vortex perturbation is believed to produce a less abrupt transition than in previous studies with a tilt perturbation, as the localized turbulence is observed via the formation of a wavy structure at a low order azimuthal mode, which resembles an optimally amplified perturbation. For higher amplitude, the localized turbulence remains at a constant axial position. It is further investigated using proper orthogonal decomposition, which indicates that the centre region close to the expansion is highly energetic.

5.1 Introduction

A brief introduction to axisymmetric expansion flow, is given in this section to make the chapter self-consitient for the reader. The flow through an axisymmetric expansion in a circular pipe is of both fundamental and practical interest. The geometry arises in many applications, ranging from engineering to physiological problems such as the flow past stenosis [46]. The bifurcations of flow patterns in sudden expansions have been studied experimentally [16, 19, 38, 39] and numerically [21, 22]. In all these studies, flow separation after the expansion and reattachment downstream leads to the formation of a recirculation region near the wall. Its extent grows linearly as the flow velocity increases. Numerical simulations and experimental results have shown that the recirculation region breaks axisymmetry once a critical Reynolds number is exceeded. Here, the Reynolds number is defined $Re = Ud/\nu$, where U is the inlet bulk flow velocity, d is the inlet diameter and ν is the kinematic viscosity. In experiments, the recirculation region loses symmetry at $Re \simeq 1139$ [19] and forms localized turbulent patches that appears to remain in at a fix axial position [22, 23, 47]. Global stability analysis [21] suggests that the symmetry breaking occurs at a much larger critical Re. The reason for the early occurrence of transition in experiments is believed to be due to imperfections, which are very sensitive to the type or the form of the imperfections. These imperfections are modelled in numerical simulations by adding arbitrary perturbations. Small disturbances are likely to be amplified due to the convective instability mechanism, and appear to be necessary to realise time-dependent solutions. Numerical results [20], have also shown that small perturbations are amplified by transient growth in the sudden expansion for $Re \leq 1200$, advect downstream then decay. Simulations in relatively long computational domains, which accommodate the recirculation region with an applied finite amplitude perturbation at the inlet [22, 47], discussed in chapter 4 have found the transition to turbulence to occur at $Re \gtrsim 1500$, depending upon the amplitude of the perturbation. The most basic perturbation is to mimic a small tilt at the inlet, via a uniform cross-flow, on top of the Hagen-Poiseuille flow [22, 47, 48]. This perturbation creates an asymmetry in the recirculation region downstream, which oscillates due to Kelvin-Helmholtz instability, similar to that of a wake behind axisymmetric bluff bodies [42]. At higher Re, the recirculation breaks to form localized turbulence. Another possibility is to include a rotation of the inlet pipe, and numerical simulations with a swirl boundary condition [49], have shown the existence of three-dimensional instabilities above a critical swirl velocity. Experimental studies have also been conducted [50], for expansion ratio of 1:8, confirming the existence of convective and absolute

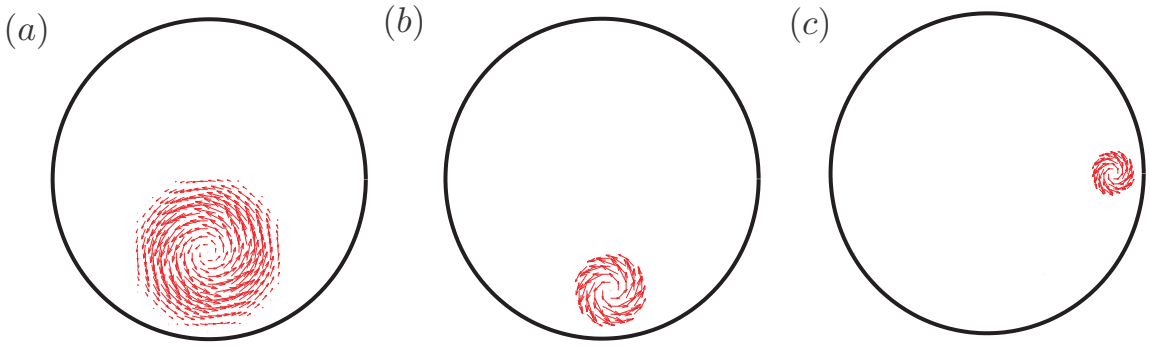

Figure 5.1: Vector plot of $\bar{u}$.(a) $\mathcal{R} = 0.25$, (b) $\mathcal{R} = 0.125$ and (c) $\mathcal{R} = 0.1$ at different positions inside the domain.

instabilities, and also time-dependent states. The higher the Re, the smaller is the swirl sufficient for the transition between states to take place. In the present investigation, a small localized vortex perturbation is added at the inlet, without wall rotation, along with the Hagen-Poiseuille flow. This vortex perturbation has been implemented to observe a less abrupt transition to localized turbulence than observed for the tilt case, enabling study of the most energetic modes during the transition. The goal of this chapter is to discuss results of expansion pipe flow with a localized vortex perturbation added to the system. Initially numerical method is discussed with regards to the simulations performed with vortex perturbation. Secondly, spatio-temporal dynamics of the turbulent patch and the analysis of the localized turbulent patch using Proper Orthogonal Decomposition (POD) is presented. Finally, the conclusions are stated.

5.2 Vortex perturbation

When trying to make connection between experimental observations and simulations, the issue of the choice of perturbation must be addressed. Many perturbations have been tested experimentally [51–54] and replications in numerical works have reproduced some of the observations [15, 55–57]. In the paper of Wu *et al.* [15], it is clearly mentioned that a perturbation on the axis of the pipe requires large amplitude to trigger transition or decays quickly. In this chapter consider a simple localized perturbation, and introduce a localized vortex to the inlet Poiseuille flow. The radial size of the vortex may be controlled as well as its position in the inlet section. This perturbation also satisfies the continuity condition at the injection point and automatically breaks axisymmetry, contrary to the tilt perturbation [21, 47] We define $s = \sqrt{(x-x_0)^2 + (y-y_0)^2}$ as the distance between the center of the vortex at (x_0, y_0) to any point (x, y) in the cross-section, at which the local measure of rotation is given by

$$\Omega = \begin{cases} 1, & s \leq \mathcal{R}/2, \\ 2(\mathcal{R}-s)/R, & \mathcal{R}/2 < s \leq \mathcal{R}, \\ 0, & s > \mathcal{R}\,, \end{cases} \tag{5.1}$$

where $\mathcal{R}$ is the radius of the vortex. The velocity perturbation $\bar{u}$ in Cartesian coordinates is then

$$\bar{u} = \delta\,\Omega\,(y_0 - y,\, x - x_0,\, 0)\,, \tag{5.2}$$

where δ is a parameter measuring the strength of the vortex. The full inlet condition is therefore

$$\begin{aligned} v_x &= \Omega(x - x_0), \\ v_y &= \Omega(y_0 - y), \\ v_z &= 2(1 - 4r^2) \end{aligned} \tag{5.3}$$

Then the inlet condition is given by:

$$\boldsymbol{v}(\boldsymbol{x}, t) = (x - x_0)\boldsymbol{e}_x + (y_0 - y)\boldsymbol{e}_y + 2(1 - 4r^2)\boldsymbol{e}_z \tag{5.4}$$

where $r^2 = x^2 + y^2$. Figure 5.1 show vortex perturbation inside inlet section, 5.1(a) shows a vortex of size $\mathcal{R} = 0.25$ and 5.1(b, c) shows that with the formula vortex can be placed anywhere inside the

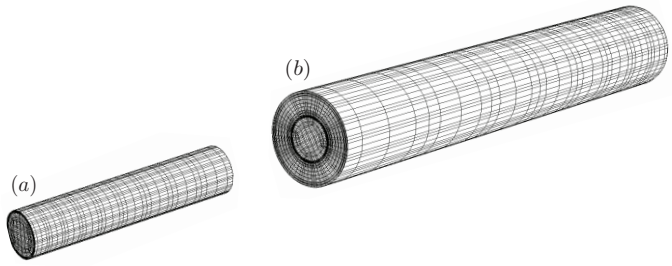

Figure 5.2: Computational domain (a) inlet domain, (b) outlet domain which are stitched together.

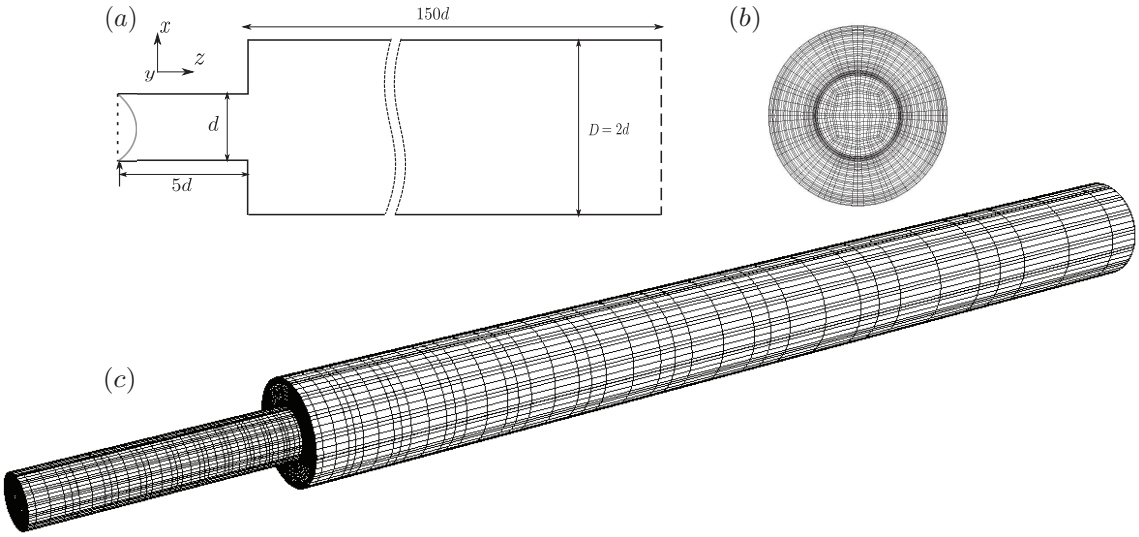

Figure 5.3: The spectral-element mesh of the sudden expansion pipe. (a) Sketch of the domain, (b) (x, y) cross-section of the mesh (the dark lines represent the elements and the grey lines represent the Gauss-Lobatto-Legendre mesh), (c) (x, z) cross section of the pipe around the expansion and (d) truncated three dimensional view of the expansion pipe. The mesh is made of $K = 63,200$ elements.

domain. The other advantage of the formulation is that additional vortex can be added. In all the simulations presented in this chapter, a single vortex with size $\mathcal{R} = 0.25$ is kept constant.

5.3 Computational domain

The sudden expansion mesh is created by stitching to straight pipes, which two different diameters as shown in Figure 5.2. The flow inside in the expansion pipe geometry is governed by unsteady three-dimensional incompressible Navier-Stokes equations for a viscous Newtonian fluid as discussed in chapter 4. The equations are solved with the initial condition (6.6) and boundary conditions:

$$\boldsymbol{v}(\boldsymbol{x}, t) = 0 \qquad \boldsymbol{x} \in Wall, \tag{5.5}$$

$$P\boldsymbol{n} - \boldsymbol{n} \cdot \nabla \boldsymbol{v}(\boldsymbol{x}, t)/Re = 0 \qquad \boldsymbol{x} \in Outlet, \tag{5.6}$$

corresponding to no-slip (6.1) at the walls, and a open boundary condition (6.2) at the outlet of the pipe. The equation (6.2) is a Neumann boundary at the outlet, with $\boldsymbol{n}$ being the surface vector pointing outwards from the computational domain, chosen to avoid numerical oscillations. Figure 5.3(a) is a schematic diagram of the sudden expansion pipe. The length of the inlet pipe is $5d$, the outlet pipe is $150d$, and the expansion ratio is given by $E = D/d = 2$, where D is the outlet pipe diameter. The computational mesh was created using hexahedral elements. Figure 5.3(b) shows the (x, y) cross section of the pipe with 160 elements and the streamwise extent of the pipe has 395 elements. The mesh is refined near to the wall and near the expansion section (see figure 5.3(c)). A three dimensional view of the mesh along the expansion pipe is displayed in figure 5.3(d). The mesh used here contains approximately

N	KN^3 ($\times 10^6$)	Reattachment Position z_r	Viscous Drag
4	4.0	43.58	0.3725
5	7.9	43.72	0.3333
6	13.6	43.73	0.3323

Table 5.1: Convergence study, changing the order of polynomial N. z_r is the non-dimensional length of the recirculation region in the pipe for $Re = 1000$.

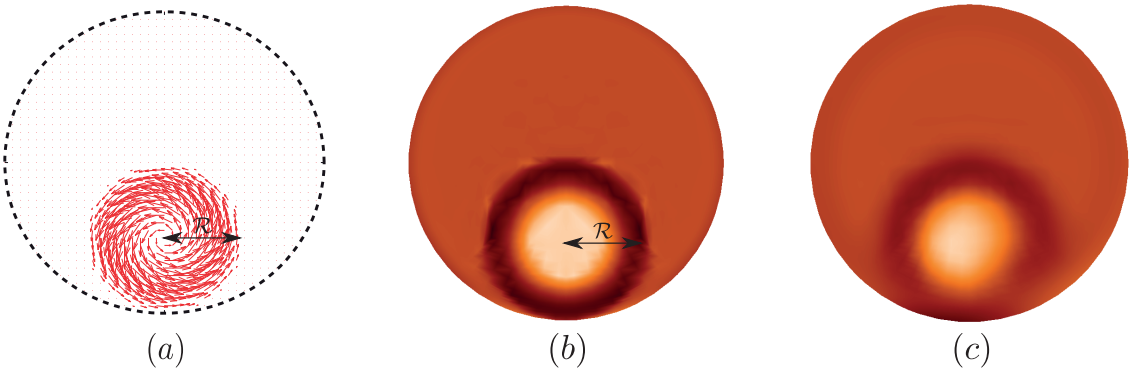

Figure 5.4: (a) Vector plot of $\vec{u}'$. Axial vorticity contour of the vortex perturbation ($\mathcal{R} = 0.25$) in the inlet of the pipe at (b) $z = -5$ and (c) $z = -2.5$ for $Re = 2000$. Black and white corresponds to the maximum and minimum of vorticity and orange (grey) represents zero vorticity.

four times more elements than our previous study [47]. Table 5.1 shows the parameters used to assess convergence: (i) the flow reattachment point, z_r, and (ii) the viscous drag. The convergence study was done at $Re = 1000$ (z_r is very sensitive and may be affected by the outlet at larger Re) and no qualitative changes were found for $Re = 2000$. $N = 5$ is sufficient to resolve the flow accurately near the separation point as well as at the reattachment point. The total number of grid points in the mesh is approximately $KN^3 = 7.9 \times 10^6$, where K is the number of elements. The entire set of simulations reported here took over one calendar year to complete on four processors.

5.4 Effect of amplitude of the vortex perturbation

The perturbation is added at the inlet pipe along with the parabolic flow velocity profile at $z = -5$. Figure 5.4(a) is a cross-section of velocity field of the vortex perturbation. Figure 5.4(b) and (c) show contour plots of axial vorticity at the inlet section of the pipe, $z = -5$, and further downstream at $z = -2.5$. The contours show that the perturbation diffuses and becomes smoother along the inlet. At the expansion section, $z = 0$, perturbations are known to be amplified [20]. In previous works [21, 47], the addition of a tilt perturbation has been found to trigger transition to turbulence. However, the tilt perturbation (i) creates a discontinuity at the inlet and (ii) does not break the mirror symmetry. In this respect, the vortex perturbation permits a more controlled transition, resulting in smoother dependence of the transitional regime on the strength of the perturbation. Figure 5.5 shows a space-time diagram for the centreline streamwise vorticity at $Re = 2000$ for different perturbation strengths, δ. After $t \approx 500$, it can be seen that for different δ the flow settles into different behaviours of the turbulent patches, observed over the following 1500 time units. Computational costs limit simulations to larger t. For $\delta < 0.05$, the perturbation decays before reaching the expansion section. At $\delta = 0.05$ (see figure 5.5(a)), a turbulent localized patch forms, then moves downstream. Around $t \simeq 600$ another turbulent patch forms upstream at $z \simeq 60$ and the downstream patch decays immediately. This process appears to repeat in a quasi-periodic manner. When the amplitude of the vortex perturbation is increased, $\delta = 0.1$, see figure 5.5(b), again a patch of turbulence appears, then moves downstream. When a turbulent patch arises upstream at $t \simeq 600$, the patch downstream again decays immediately. This time, however, the process appears to repeat more stochastically, in time and location, of the arising upstream patch. Occasional reversal in the drift of the patch is also observed. It is expected that if the patch drifts far downstream, then it will relaminarise, since the the local Reynolds number based on the outlet diameter is $Re/E = 1000$, somewhat below the 2000 typically required for sustained turbulence.

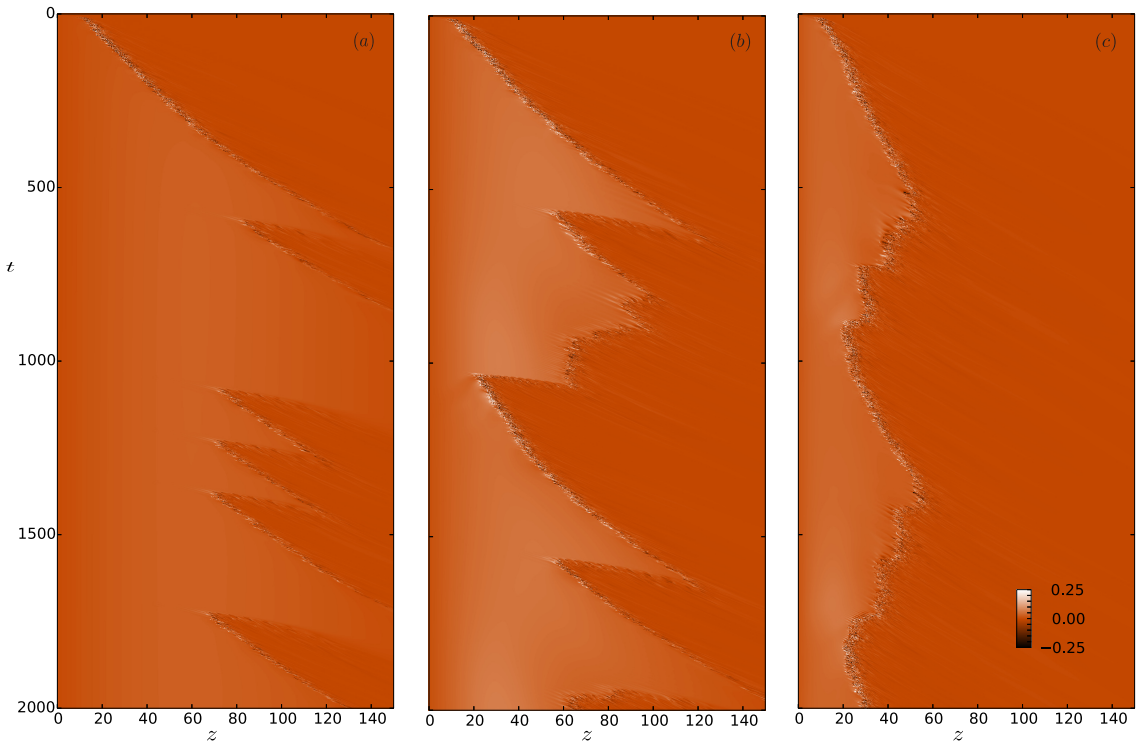

Figure 5.5: Spacetime diagram of the centreline streamwise vorticity for $Re = 2000$ for (a) $\delta = 0.05$, (b) $\delta = 0.1$, and (c) $\delta = 0.2$.

It is likely that the deformation to the flow profile by the upstream patch reduces the potential for growth of perturbations within the patch downstream, disrupting the self-sustaining process. Still for $\delta = 0.1$, figure 5.6 shows the streamwise vorticity for a (x, z) cross-section over the whole pipe: $150d$. At $t = 1000$ (see figure 5.6(a)), it can be seen that only a single turbulent patch exists in the domain. At $t = 1025$ (see figure 5.6(b)), an axially periodic structure appears at $z \simeq 10$. Once this develops into turbulence (see figure 5.6(c)), the patch downstream dissipates rapidly (see figure 5.6(d)). The appearance of the new patch in our expansion is different from the puff splitting process observed in a straight pipe [3–5, 7–9, 53, 58]. Here the new turbulent patch evolves out of the amplified perturbation at the entrance and breaks down into turbulence, forming a new patch upstream of an existing patch. The patch drifts downstream and decays. The slopes in the diagrams of figure 5.5 indicate the drift velocity of the patch, which varies with respect to δ and z, and decreases as δ increases. Figure 5.7 shows the iso-surface streamwise vorticity for the axially periodic structure that appears at $z \simeq 10$, in this case it is shown for $12.5 < z < 25$ at $t = 2000$. This structure appears repeatedly and resembles the optimally amplified perturbation found in a sudden expansion flow by [20]. Initially the structure appears near the expansion region, where the flow is very sensitive to perturbations, it is amplified and then breaks down into turbulence downstream. For $\delta = 0.2$, see figure 5.5(c), the turbulent patch never goes beyond $z \simeq 60$. Here the perturbation develops consistently into turbulence, so that its position remains roughly constant. The patch remains close enough to the entrance so that there is insufficient space for a new distinct patch to arise. For large amplitude $\delta = 0.5$, the turbulence patch does not drift, remaining at a more stable axial position, shown in the spatiotemporal diagram of figure 5.8(a). A snapshot of the flow at $t = 100$ is also presented in figure 5.8(b), and this streamwise vorticity contour plot highlights the effect of the vortex perturbation that is clearly at the origin of the turbulent patch. In previous works [21, 47], spatially localized turbulence has also been observed, and one question that can be asked is how similar or different is this localized turbulence from the turbulent puffs observed in straight pipe flow [5]? Using spatial correlation functions, previous works [47] have found that the localized turbulence in expansion pipe flow is more active in the centre region than near the wall, hence different from the puffs in uniform pipe flow [6]. In the next section, we provide results on a another analysis tool: the proper orthogonal decomposition.

Figure 5.6: $x - z$ cross sections of streamwise vorticity contour plot for $Re = 2000$ with $\delta = 0.1$ at (a) $t = 1000$, (b) $t = 1025$, (c) $t = 1050$ and (d) $t = 1100$. Each triad represents the full pipe length, truncated at every $50d$ for simple visualization purpose. Here black and white corresponds to the maximum and minimum of vorticity and orange (grey) represents zero vorticity.

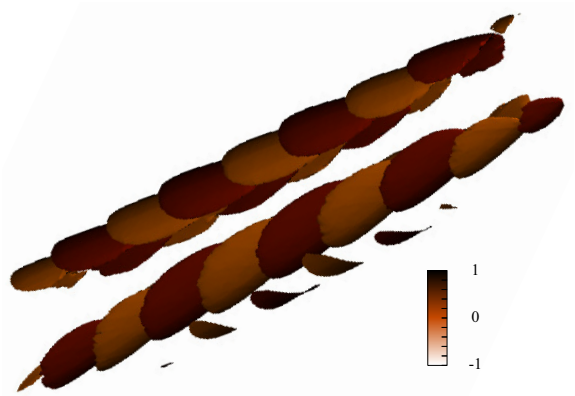

Figure 5.7: Iso-surface of streamwise vorticity resembling the optimal perturbation for $Re = 2000$, $\delta = 0.1$ at $t = 1025$ and spanning from $z = 12.5$ to 25 from left to right.

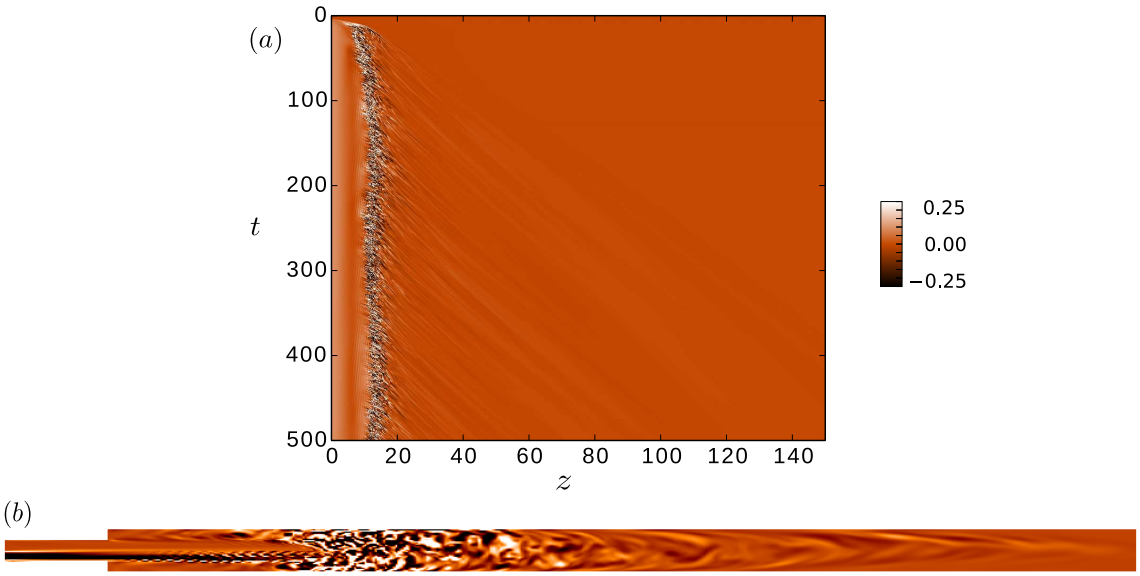

Figure 5.8: (*a*) Spacetime diagram for the centreline streamwise vorticity for $Re = 2000$ and $\delta = 0.5$. (*b*) Zoomed contour plot of the streamwise vorticity for z up to 50, black and white corresponds to the maximum and minimum of vorticity and orange (grey) represents zero vorticity. Note the perturbation development between the expansion section and the turbulent patch.

5.5 Proper Orthogonal Decomposition Method

Principle Component Analysis, often called Proper Orthogonal Decomposition (POD) in the context of fluid flow analysis, has been widely used by several researchers [59–62] to identify coherent structures in turbulent flows by extracting an orthogonal set of principle components in a given set of data. Each data sample a_i, being a snapshot state, may be considered as a vector in m-dimensional space, where m is e.g. the number of grid points. These vectors may be combined to form the columns of the $m \times n$ data matrix $\boldsymbol{X} = [a_1\, a_2\, \ldots\, a_n]$, where, n is the number of snapshots. Let $\boldsymbol{T}$ be an $m \times n$ matrix with columns of principle components, related by to $\boldsymbol{X}$ by

$$\boldsymbol{T} = \boldsymbol{X}\boldsymbol{W}\,. \tag{5.7}$$

$\boldsymbol{T}$ is intended to be an alternative representation for the data, having columns of orthogonal vectors with the property that the first n' columns of $\boldsymbol{T}$ span the data in $\boldsymbol{X}$ with minimal residual, for any $n' < n$. Here the inner product $a^T a$ corresponds to the energy norm for the minimisation. $\boldsymbol{W}$ is defined via the singular value decomposition (SVD) of the covariance matrix $\boldsymbol{X}^T\boldsymbol{X}$. If the SVD of $\boldsymbol{X}$ is

$$\boldsymbol{X} = \tilde{\boldsymbol{U}}\Sigma\boldsymbol{W}^T\,, \tag{5.8}$$

where, Σ is the diagonal matrix of the singular values, then

$$\boldsymbol{X}^T\boldsymbol{X} = \boldsymbol{W}\Sigma^T\tilde{\boldsymbol{U}}^T\tilde{\boldsymbol{U}}\Sigma\boldsymbol{W}^T = \boldsymbol{W}\Sigma^2\boldsymbol{W}^T\,. \tag{5.9}$$

Also the SVD of $\boldsymbol{X}^T\boldsymbol{X}$ may be calculated,

$$\boldsymbol{X}^T\boldsymbol{X} = \boldsymbol{U}\boldsymbol{S}\boldsymbol{V}^T\,. \tag{5.10}$$

Comparing equation (5.9) and (5.10) we have that $\boldsymbol{W} \equiv \boldsymbol{U}$. Therefore, to calculate the principle components we construct the $n \times n$ matrix of inner products $\boldsymbol{X}^T\boldsymbol{X}$, where it is assumed that $n \ll m$, and compute its SVD (5.10). Only the first columns of $\boldsymbol{T}$ are expected to be of interest, and the j^{th} principle component $\hat{u}_j$ may be obtained by

$$u_j = \sum_{i=1}^{n} a_i \boldsymbol{U}_{i,j}, \qquad \hat{u}_j = u_j/(u_j^T u_j). \tag{5.11}$$

The normalised singular values

$$\hat{\Sigma}_{jj} = \sqrt{\boldsymbol{S}_{jj}/(n-1)}, \tag{5.12}$$

are a measure of the energy captured by each component, having the property that $\hat{\Sigma}_{jj}$ equals the root mean square of $a_i^T\hat{u}_j$ over the data set.

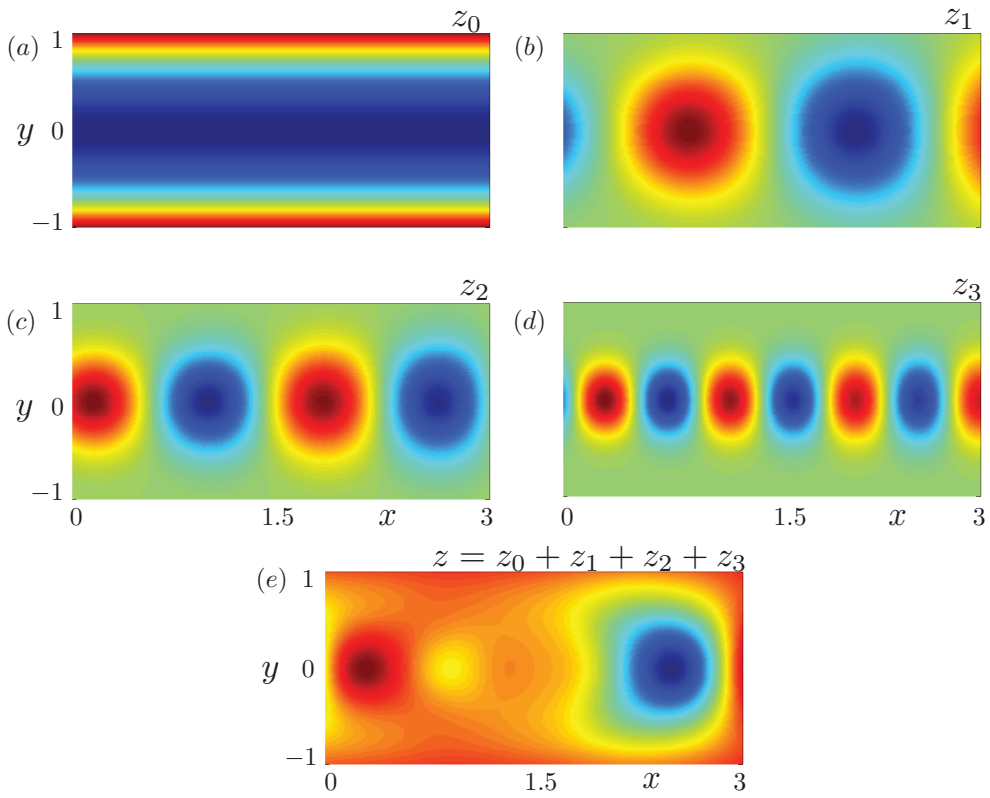

Figure 5.9: Fabricated patterns that are input into the flow.

5.6 Validation of POD alogrithm

To validate the POD algorithms ability to identify coherent structures inside the flow, a series of fabricated patterns that constructed and introduced inside a flow. Equation (5.15) helps to simulate a multi-dominant structures buried in the fluid flow. The basic idea of the validation is to introduce known coherent structures of particular frequency and to check if the POD algorithm can retrieve it. Here, the method proposed by Seena and Sung (2011) is applied to construct the fabricated patterns

$$z_0(x,y,t) = exp(-y^2/0.7) \tag{5.13}$$

$$z_n(x,y,t) = \alpha_n(t) \sum_{m=-\infty}^{m=\infty} (-1)^m exp\left[-\left(\frac{(x-\beta_n m-\gamma_n t)^2}{d_n} + \frac{y^2}{d_n}\right)\right], \quad n = 1,2,3,... \tag{5.14}$$

$$z = z_0 + z_1 + z_2 + z_3 \tag{5.15}$$

where $d_n = a_n x + b_n$ is the diameter of the structure, a_n and b_n are the constants, $a\beta_n$ is the wavelength factor defined as the distance between two neighboring structures, γ_n is the convection velocity of the structure in the streamwise direction, and α_n is the growth or decay factor. The dominant frequencies of these three structures z_1, z_2, and z_3 are determined by $f_n = \gamma_n/(2\beta_n)$ i.e., 0.5 Hz, $1.64Hz$, and $4.0Hz$, respectively. The value of the coefficient $\alpha_n(t)$ determines variations in the convecting structures; that is, at $\alpha_n(t) = 1$ the structures are constant without growth or decay while the cases at $\alpha_n(t) > 1$ and $\alpha_n(t) < 1$ correspond to the growing and decaying structures, respectively. The fabricated multi-dominant structure pattern is composed of three different dynamic structures ($n = 1, 2, 3$), each of which evolves with a certain velocity at different frequencies. The parameters for each pattern are listed in table (5.2).

Figure 5.9 shows snapshots of the structures that are input into the flow field. The structures z_1, z_2 and z_3 are formulated in a such way to be constant, decay and grow respectively as they move from left to right side of the domain. The characteristic frequency of the dominant structure increases with n. Heren the complete flow pattern is constructed by superimposing the the three structures of different sizes and frequencies onto the stationary field. Figure 5.9 (a) shows the stationary filed and the figures 5.9 (b, c, d) represent the three different structures built z_1, z_2 and z_3 respectively. The multi-dominant flow field is $z = z_0 + z_1 + z_2 + z_3$, as show in figure 5.9 (d), it can be seen that after superimposing

n	a_n	b_n	β_n	γ_n	f (Hz)	$\alpha_n(t)$
1	0.030	0.050	0.8	0.8	0.5	1
2	0.015	0.035	0.55	1.8	1.64	$e^{-t/30} - 0.1$
3	0.0075	0.020	0.3	2.4	4.0	$1 - e^{-t/20} + 0.2$

Table 5.2: Constants for the fabricated pattern.

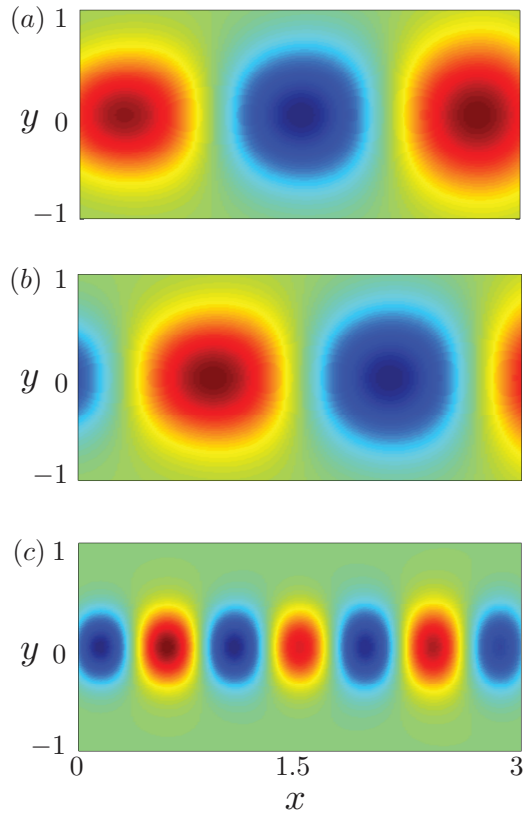

Figure 5.10: The first three POD modes extracted from the fabricated multi-dominant structure pattern.

structures the flow field becomes more complex. To apply POD algorithm on to constructed flow field, total of 200 successive snapshots with a sampling frequency of 10 Hz were analyzed using the POD algorithm, It was found that the, cumulative energy of the first six modes reaches 99.7% of the total. Thus, the first six modes would give an accurate reflection of the three buried structures. The spatial distributions of the first three POD modes are shown in figure 5.10, a general view of which shows that the first, second, and third pairs of POD modes share similarities with the structures q_1,q_2, and q_3 shown in figure 5.9, respectively. In order to further validate, Fourier coefficients of the modes where computed, figure 5.11 (a) shows the value of Fourier coefficient of the first three modes respectively. Figure 5.11 (b) is the Fast Fourier Transform of the Fourier coefficient signal obtained from the first POD mode. The spectrum peaked at $f_1 = 0.49$, $f_2 = 1.61$ and $f_3 = 3.99$ respectively, which is nothing but the frequencies of the three coherent structures that where introduced into the stationary flow field.

5.7 POD on localized turbulence

Applying POD to turbulence can help us visualize the most energetic structures inside it. A large number of snapshots were collected, and it was found that after 1200 snapshots the energy of the leading POD modes (principle components) became independent of the number of snapshots. Figure 5.12(a)shows the axial velocity of mode 1, which constitutes 74% of the total kinetic energy. It can be seen that the center core region is predominant and its shape is reminiscent of the vortex perturbation. Hence, the inlet flow has more effect on the localised turbulence than the wall shear. Mode 2 is shown

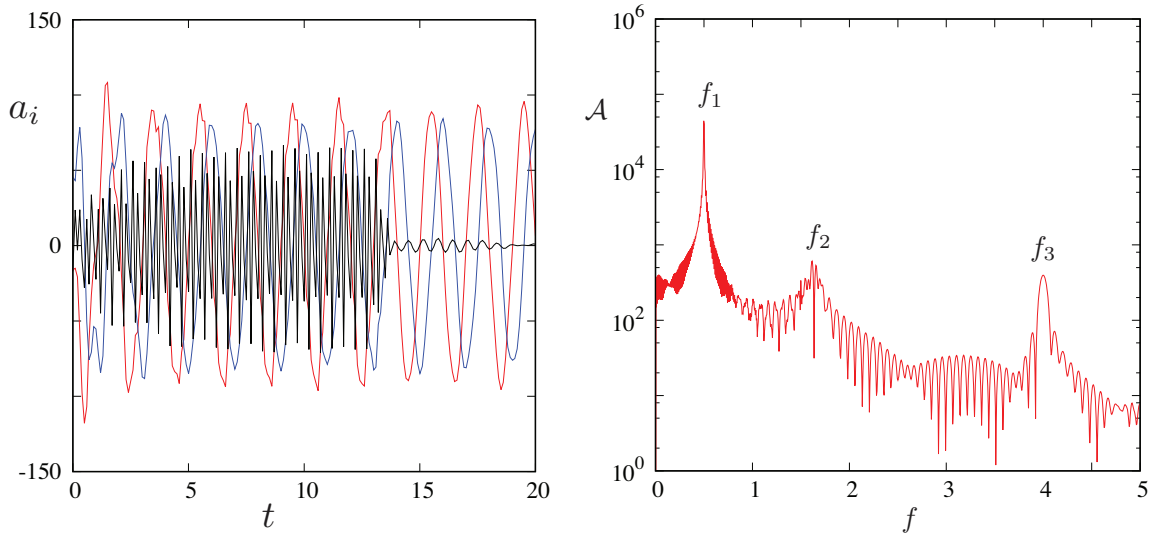

Figure 5.11: (a) Fourier coefficients of first three mode, where red, blue and black correspond to first, second and third POD mode respectively. (b) Power spectra of temporal POD mode coefficients extracted from first POD mode.

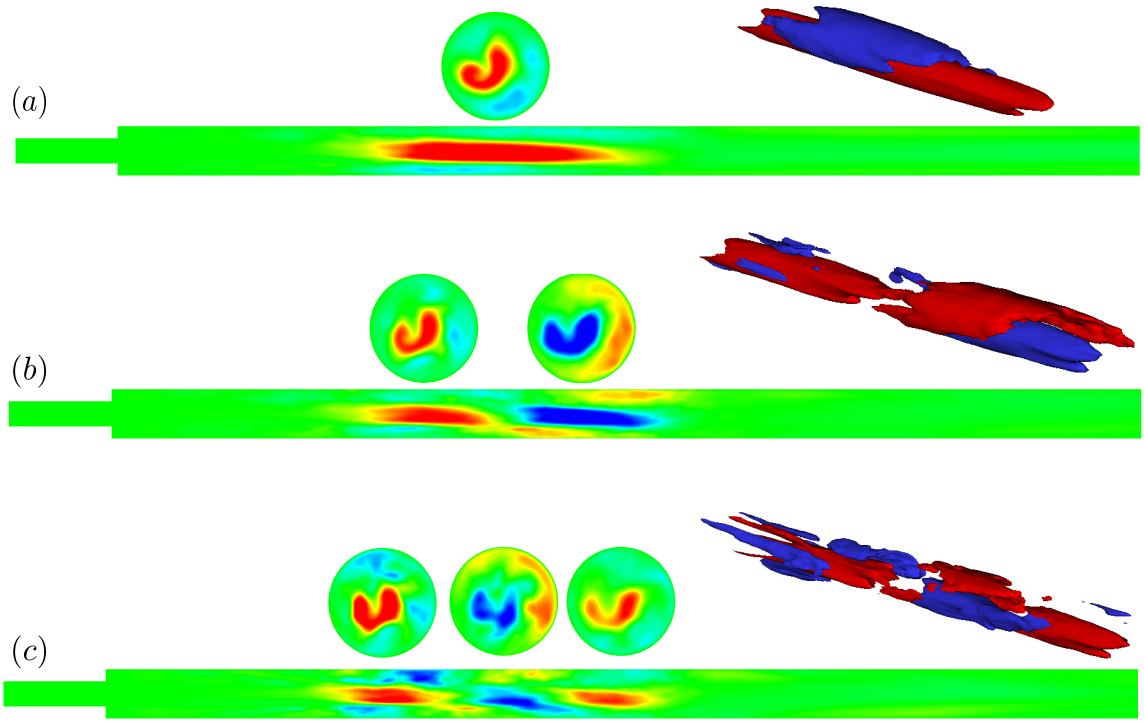

Figure 5.12: Cross sections (x, z), (x, y) and iso-surfaces of the proper orthogonal decomposition. (a) Mode 1, (b) mode 2 and (c) mode 3 computed for $Re = 2000$ and $\delta = 0.5$ using 1500 snapshots. Red (light-gray) and blue (dark-gray) correspond to the maximum and minimum of streamwise velocity component.

in the figure 5.12(b), has two predominant region along the axial direction and constitutes $\approx 20\%$ of the energy. Mode 3 represents only $\approx 3\%$ of the energy and is shown in the figure 5.12(c). The remaining modes appear more complex and less energetic. The study of spatial correlation in chapter 4 and POD has revealed the sustainability of the localized turbulence is due to the inlet flow and the perturbation that is applied along with it. Any change in the perturbation or the inlet condition can have drastic effect on the localized turbulence, Once the perturbation is turned off the flow field will revert back to laminar state.

In addition, simulations were carried out by changing $\mathcal{R}$ and (x_0, y_0) independently. It has been found that (i) a smaller vortex perturbation: $\mathcal{R} \lesssim 0.2$ and (ii) a vortex closer to the centreline could not sustain a fixed localized turbulent patch [15].

5.8 Conclusions

Numerical results for the flow through a circular pipe with a sudden expansion in presence of a vortex perturbation at the inlet have been presented. For $Re = 2000$ and a relatively small perturbation amplitude, $0.05 \lesssim \delta \lesssim 0.1$, a patch of turbulence in the outlet section is observed to drift downstream, then decay upon the appearance of another patch of turbulence upstream. Moreover, this vortex perturbation produces a controlled transition, in that the transitional regime depends smoothly on the perturbation strength, and the origin of symmetry breaking is defined. Further, the turbulent patch that forms first appears via a low order azimuthal mode resembling an optimal perturbation. The process repeats quasi-periodically or stochastically as the amplitude of the perturbation, δ, increases. The turbulent patch formation is different from the puff splitting behaviour observed in uniform pipe flow [3, 5, 8, 58], as here the new patches arise upstream of existing turbulent patches. The drift velocity of the patch varies with δ, decreasing as δ is increased. For large δ, the patch does not drift downstream, but holds a stable spatial position forming localized turbulence. The structure within the localised turbulence is further studied using proper orthogonal decomposition, which indicates that the first mode comprises most of the energy and the flow is more active in the centre region than near the wall. The growth and decay of the vortex perturbation should be explored to understand the onset of turbulence, which will dealt in the chapter 5.

Chapter 6

Transition in a straight circular pipe

In the previous chapter, the effect of vortex perturbation on sudden expansion pipe was examined. In this chapter, we apply the vortex perturbation to the constant diameter pipe with special focus on the wall pressure fluctuations. Numerical simulations of transition to turbulence in a straight pipe [3, 4, 6–9, 45, 63], in general are performed using a short length pipe, using periodic boundary condition. It is used to reduce the computational cost. Recent DNS of straight pipe with long computational domain [15], has shown that the energy of the finite amplitude perturbation at the inlet, grows exponentially. Finite amplitude turbulent perturbation are induced via a thin circular ring present at the core region, which leads to the formation of helical structure that tends to become large-scale reverse hairpin vortices as they convect downstream. Interactions of these reverse hairpin vortices among themselves and their interaction with near wall flow creates smaller hairpin structures that lead to break down to form full developed turbulence. DNS results of transition to turbulence is presented in this chapter. A finite amplitude vortex perturbation, is applied at the inlet, that leads to transition to turbulence. Looking at the mean value of velocity and pressure, reveal less detail about the transition. Whereas, velocity and pressure fluctuations measured at the center of the pipe and in the near wall region seems to increase exponentially. Figure 6.1(a) is a schematic diagram of the pipe. The length of the pipe is $75D$,

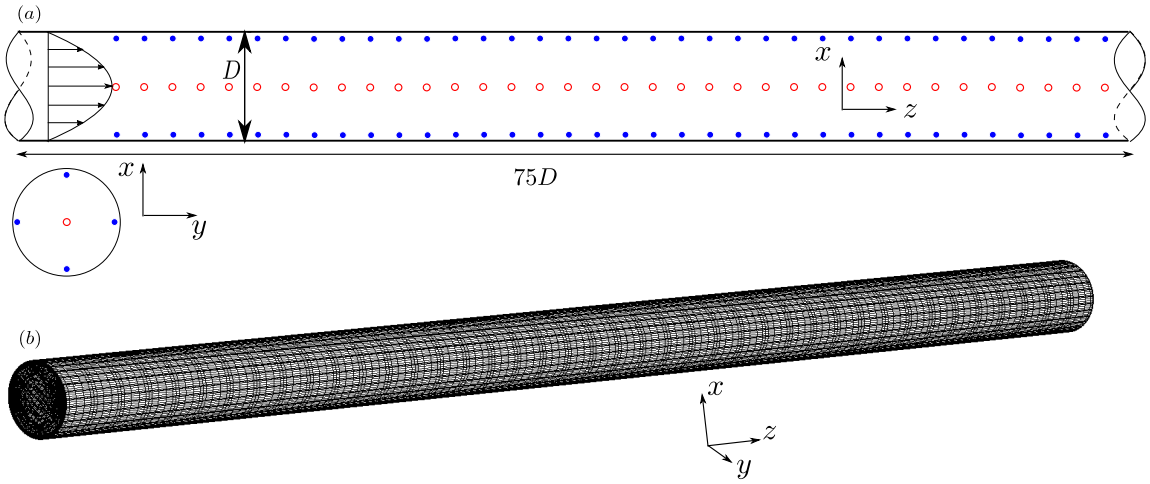

Figure 6.1: The spectral-element mesh of the straight pipe. (a) Sketch of the computational domain, the red circles and blue dots correspond to the numerical probes placed along the axial direction to measure velocity and pressure fluctuations at the center and in the near wall region. A total of 750 probes were placed in centre of the pipe and in the near wall region along the axial direction. (b) Truncated three dimensional view of the pipe. The mesh is made of $K = 64,000$ elements.

where D is the pipe diameter. The computational mesh was created using hexahedral elements. A three dimensional view of the mesh is displayed in figure 6.1(b). A $N = 6$ order Lagrange polynomial interpolants was used on the Gauss-Labatto-Legendre points to have higher resolution. The total number of grid points in the mesh is approximately $KN^3 = 13.8 \times 10^6$, where K is the number of elements. The probes were placed at center as well as in the near wall region to measure the velocity

and pressure along the streamwise direction. In terms of the near-wall region, the probes data were averaged from four measurement point along the circumference of the pipe section.

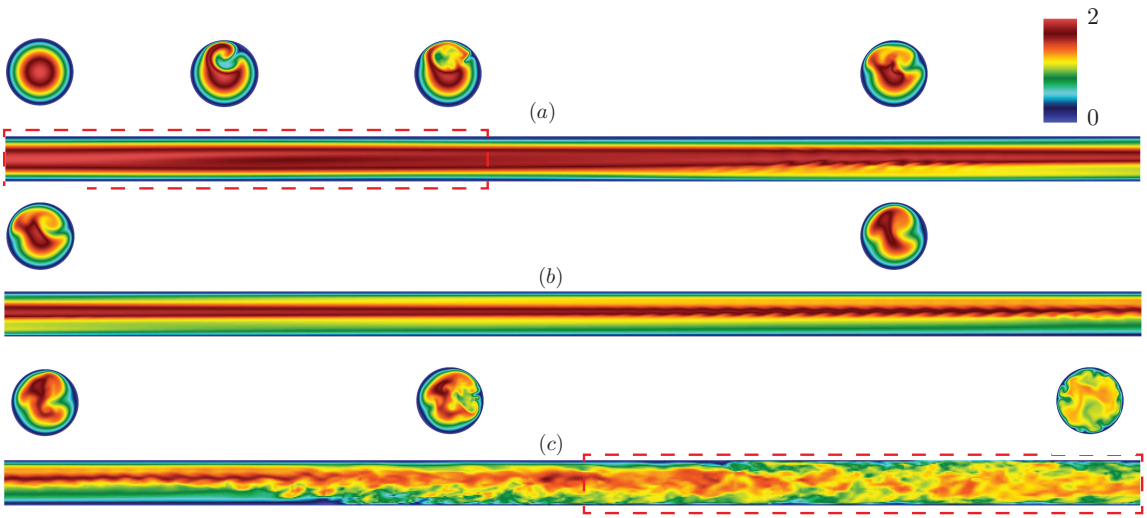

Figure 6.2: Contour plot of streamwise velocity for $Re = 5000$ at $t = 1600$. The pipe has been truncated as (a) $0 - 25d$ (b) $25d - 50d$ (c) $50d - 75d$

6.1 Numerical Method

Three-dimensional incompressible Navier-Stokes equations for a viscous Newtonian fluid as discussed in chapter 4. The equations are solved with the initial condition (6.6) and boundary conditions:

$$\boldsymbol{v}(\boldsymbol{x}, t) = 0 \qquad \boldsymbol{x} \in Wall, \tag{6.1}$$

$$P\boldsymbol{n} - \boldsymbol{n} \cdot \nabla \boldsymbol{v}(\boldsymbol{x}, t)/Re = 0 \qquad \boldsymbol{x} \in Outlet, \tag{6.2}$$

corresponding to no-slip (6.1) at the walls, and an open boundary condition (6.2) at the outlet of the pipe. The equation (6.2) is a Neumann boundary at the outlet, with $\boldsymbol{n}$ being the surface vector pointing outwards from the computational domain, chosen to avoid numerical oscillations. For the inlet boundary condition, Hagen-Poiseuille flow was applied along with a vortex perturbation. Equation of the finite amplitude vortex perturbation is recollected for the convenience of the reader. The vortex perturbation has been designed in a way to control the radial size $\mathcal{R}$ and the strength δ. It can also be placed at any where inside the inlet section. It satisfies the continuity condition at the injection point and breaks mirror symmetry. The distance between center of the vortex at (x_0, y_0) to any point (x, y) in the cross-section is defined by $s = \sqrt{(x - x_0)^2 + (y - y_0)^2}$. Measure of rotation is given by:

$$\Omega \quad = \quad \begin{cases} 1, & s \leq \mathcal{R}/2, \\ 2(\mathcal{R} - s)/R, & \mathcal{R}/2 < s \leq \mathcal{R}, \\ 0, & s > \mathcal{R}\,, \end{cases} \tag{6.3}$$

where $\mathcal{R}$ is the radius of the vortex. The velocity perturbation $\tilde{u}$ in Cartesian coordinates is then

$$\tilde{u} = \delta\, \Omega\, (y_0 - y,\, x - x_0,\, 0)\,, \tag{6.4}$$

where δ is a parameter measuring the strength of the vortex.

$$\begin{aligned} v_x &= \Omega(x - x_0), \\ v_y &= \Omega(y_0 - y), \\ v_z &= 2(1 - 4r^2) \end{aligned} \tag{6.5}$$

Then the inlet condition is given by:

$$\boldsymbol{v}(\boldsymbol{x}, t) = (x - x_0)\boldsymbol{e}_x + (y_0 - y)\boldsymbol{e}_y + 2(1 - 4r^2)\boldsymbol{e}_z \tag{6.6}$$

where $r^2 = x^2 + y^2$. The simulation was initialised with Hagen-Poiseuille flow all over the domain. Initially, the simulations were executed upto $t = 800$. Later, streamwise velocity u and pressure P along the centreline (Red circle in figure 6.1) and near-wall region (blue dots in figure 6.1) were measured from $t = 800$ to 1600. Figure 6.1(a) shows the $x - y$ cross-section of the pipe with one probe in the centre and four probes around the near wall region. In the $x - z$ cross-section the probes are placed at every $0.5D$, which gives 5×150 probes as 750 probes.

6.2 Transition to turbulence

At first, different values of Re, $\mathcal{R}$ and δ and length of the pipe were experimented to understand the transition in straight pipe. Taking into consideration of the computational cost, the length of the pipe was fixed to $75D$ and $Re = 5000$. Simulations revealed that any perturbation below $\delta < 0.5$ and $\mathcal{R} < 0.25$ decays and the flow recovers laminar Poiseuille flow. Later, the value of $\mathcal{R}$ was fixed to $0.25D$ and $\delta = 0.5$. Figure 6.2 shows the streamwise velocity contour plot. For the purpose of visualisation, the $75D$ long pipe has been truncated into three parts. It can be seen in figure 6.2(a) the flow is laminar close to inlet and wavy structures occurs along the domain and finally becomes turbulent close to the outlet. Cross sections in the circumference direction reveals how the perturbation breaks the spatial and temporal symmetries. At inlet, the Poiseuille flow is retained, as we move to $z = 5D$, the perturbation creates a kind of streak inside the domain. This motion of vortex perturbation, affects only one side of the domain. Above $z > 20D$, spatial and temporal symmetries are broken as they move downstream, shown in figure 6.2(b). The flow becomes quasi turbulent for $z > 55D$, which is shown in figure 6.2(c).

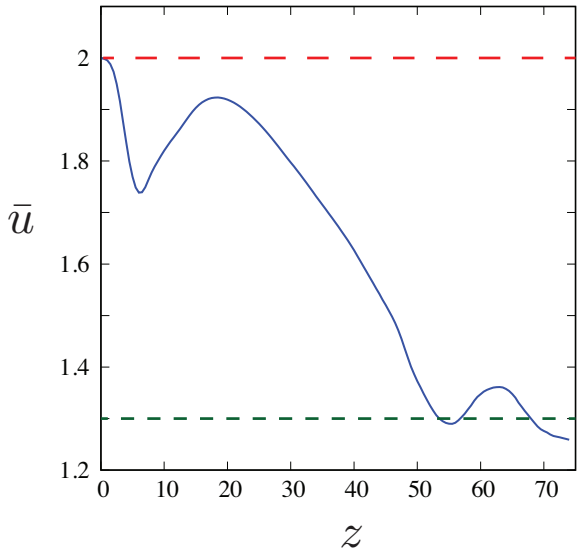

Figure 6.3: Mean value of streamwise velocity $\bar{u}$ along the axial direction, big red dotted line indicate centreline velocity for a laminar flow and the small green dotted line correspond to centreline velocity of fully-developed turbulent flow [64]. 80 000 data samples were taken from 150 probes in the centreline along the axial direction to compute the time average ($t = 800 - 1600$).

6.3 Meanflow

Streamwise velocity u and pressure P from the Navier-Stokes equation solution can be decomposed as two components $u = \bar{u} + u'$ and $P = \bar{p}$ and p'. Here $\bar{u}$ is the mean streamwise velocity, $\bar{p}$ is the mean pressure, u' and p' are the velocity and pressure fluctuations respectively. Fluctuations of the flow, tend to carry most of the information about transition. Figure 6.3 shows the mean velocity plot along the streamwise direction, measured from the centreline of the pipe. Simulation was initially run from $t = 0$ to 800, so that transient part of the flow does not affect the data for statistics. The mean value was calculated on the data obtained from time scale $t = 800$ to 1600. It can be seen that at the inlet, the velocity is twice $\bar{u}$ corresponding to the average parabolic velocity. Sudden decrease in the mean velocity close to the inlet, is due the presence of the vortex perturbation. The rotating vortex

perturbation, has significant effect of the centreline velocity field, which is been marked by the red dotted box in figure 6.2(a). As the flow convect downstream, the vortex starts to dissipate and it size starts diminishing. Similarly, looking at the red dotted box in figure 6.2(c) shows turbulent regime part along the centreline which cause the small bump close to the outlet.

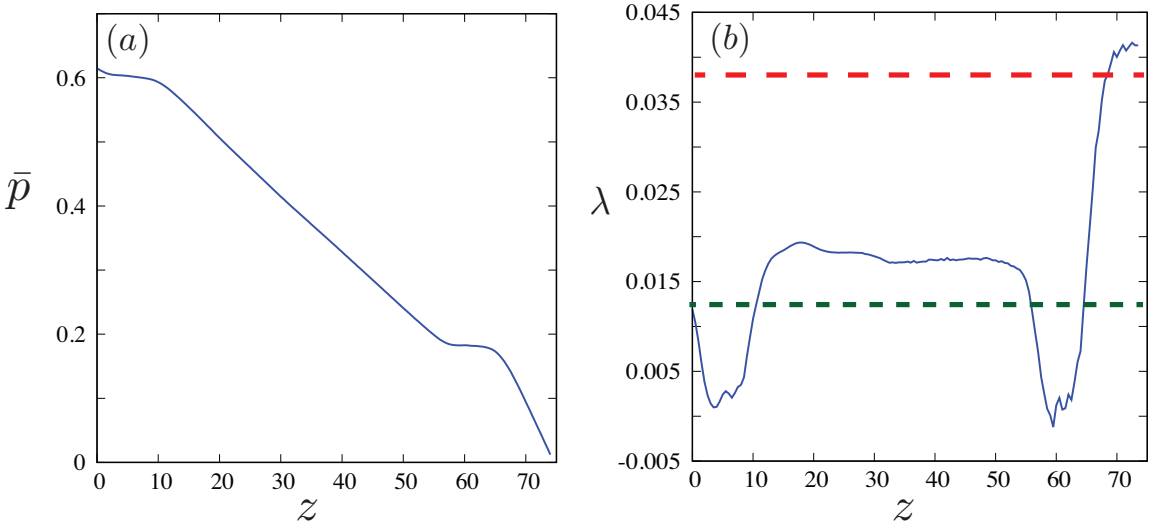

Figure 6.4: (a) Mean value of pressure $\bar{p}$ along the axial direction. (b) Skin friction factor λ along the streamwise direction (dark line). Small and large dotted line correspond to friction factor for laminar flow and fully-developed turbulent flow (Blasius). 80 000 data samples from four probes around the near wall region were used to obtain the time average.

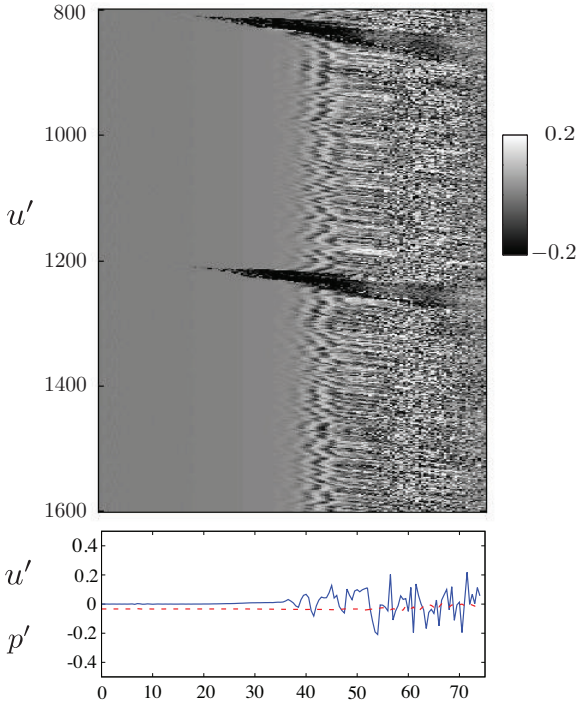

Figure 6.5: Space-time diagram of velocity fluctuations along streamwise direction, the blue and red dotted line correspond to velocity and pressure fluctuations, respectively at $t = 1600$.

Mean pressure P along the streamwise direction is shown in figure 6.4(a). It decreases monotonously from the inlet to outlet. To measure the skin friction factor $\lambda_f = -\frac{dP}{dz} D / \frac{1}{2}\rho u^2$, the gradient of the mean pressure at the near wall region was used. Gradient of pressure along the axial direction was computed

by finding the difference between two consecutive probes placed at $0.5D$ apart. Figure 6.4(b) depicts friction factor along the streamwise direction. The green small dashed line corresponds to friction factor due to laminar flow i.e., $\lambda_f = 64/Re$ and the red dashed line corresponds to $\lambda_f = 0.316/Re^{1/4}$ Blasius friction factor for turbulent pipe flow. The blue line, obtained from the simulation, remains at low value close to inlet because of the presence of laminar flow (see figure 6.2(a)) and the value tends to remain constant and increases once it reaches the turbulent regime close to outlet (see figure 6.2(a)).

6.4 Fluctuations

Fluctuation components were obtained by subtracting the mean values from the flow components. A space-time diagram shown in figure 6.5 was constructed from the stream wise velocity fluctuations at the centreline of the pipe. It shows the existence of laminar regime close to the inlet and turbulent regime after $z = 50D$. To further understand, streamwise velocity (blue line) and pressure fluctuations (red line) at $t = 1600$ from the space diagram are plotted below the space time diagram. The fluctuations close to inlet are zero and constant, which depicts the existence of laminar flow below $z \lesssim 30D$. After $z > 40D$, the amount of fluctuations start increasing. Close to the outlet section, the fluctuations tends to drop. Figure 6.6(a and b) are the standard deviation of velocity and pressure fluctuations along the streamwise direction. In term of standard deviation the velocity and pressure fluctuations, are constant and seems to increase rapidly close to the turbulent regime and decrease as they move towards the outlet. Decrease of the fluctuations at the outlet could be an effect of outlet open boundary condition applied in the numerical method.

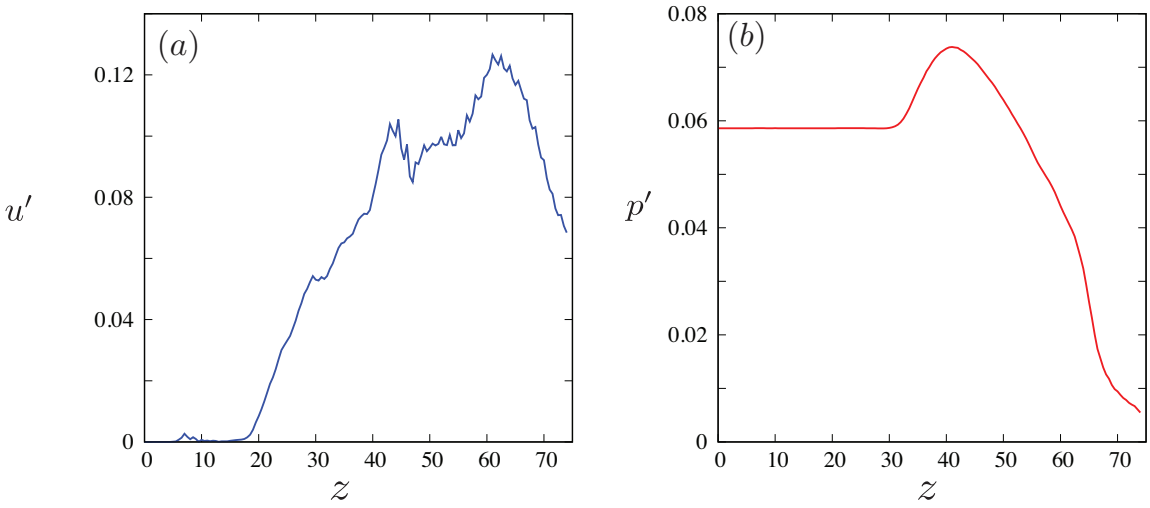

Figure 6.6: Standard deviation of fluctuations obtained using 80 000 samples of (a) velocity (b) pressure respectively.

6.5 Conclusion

DNS result for transition to turbulence at $Re = 5000$ in $75D$ long pipe with a vortex perturbation ($\mathcal{R} = 0.25D$ and $\delta = 0.5$)was presented. Instead of periodic boundary condition, velocity and open boundary condition were applied to study the spatial development of pipe flow. Simulations provide evidence of spatial and temporal symmetry breaking structures occurring inside the domain, which later initiates turbulence downstream. Mean value of velocity from the centreline decreases as the flow develops downstream along with the mean pressure. Analysing the skin friction factor of the pipe reveal the flow is laminar close to the inlet and turbulent at outlet, by comparing with friction factor of laminar flow and full-developed turbulent flow. Velocity fluctuations are absent close to inlet and increases rapidly as it moves downstream, but decay down as they reach the outlet condition. This effect of outlet can be verified only by performing new simulations with a larger computational domain and also by changing the open boundary condition to convective boundary.

Chapter 7

Wall pressure fluctuation in developing turbulent flow

7.1 Introduction

Direct numerical simulations on spatially developing pipe flows have been carried out showing the existence of helical vortex filament and large-scale vortices, which grow as they convect downstream and trigger turbulence [15]. In theory, linear stability analysis [65–72] suggests that the perturbations at the inlet are responsible for transition to turbulence at lower Reynolds number, $Re = UD/\nu$, where U is the mean velocity, D is the pipe diameter, and ν the kinematic viscosity of the fluid. To achieve laminar flow, the perturbations like background vorticity or thermal gradients at the inlet could be minimised using honeycombs, screens and temperature control. Several experimental observations [1, 2, 5, 12–14, 52–54, 73–76] have shown that the laminar state in pipe flows can be achieved over a wide range of flow rates or Re up to 100 000 [2]. Furthemore, it was shown that finite amplitude perturbation at the inlet causes the energy to grow exponentially [15] with the axial distance and creates vortical structures that break down to become fully developed turbulence. Velocity fluctuations are widely used to identify the behaviour of developing turbulent flow. The pressure field on the other hand, which is strongly coupled with the gradient of the mean velocity and fluctuations, is less explored. This chapter is dedicated to report the results of an experimental study of the development of pipe flow at high Reynolds numbers. The wall pressure fluctuations along the axial direction are measured to identify their growth and behaviour. In the first part , the relationship between the pressure and velocity is explained, followed by the re-analysis of data from [14]. Secondly part, explains the experimental setup and the pressure measurement system. Growth of pressure fluctuations as a function of the axial position is discussed In third part for Reynolds number in the range of 10^5 to 10^6. Finally, tuft tuft visualisations are presented.

7.2 Velocity-Pressure coupling

The fluctuations of the velocity component carry information about the behaviour of the flow. Measurements of the statistics of centreline velocity fluctuations were used to obtain the axial position for fully developed pipe turbulence [5, 14]. According to [11] and [14], most of the transition to turbulence occurs in the entrance region up to about 60 diameters from the pipe inlet. In general, most of the literature on developing turbulent flow has been conducted using velocity fluctuations, whereas pressure fluctuations are less explored. This paper deals with studying the behaviour of pressure fluctuations in a developing turbulent circular pipe flow. The pressure field of an incompressible flow can be obtained by taking the divergence of the Navier-Stokes equation, this gives a Poisson equation, that shows a strong coupling between pressure and velocity:

$$\frac{1}{\rho}\nabla^2 P = -\frac{\partial U_i}{\partial x_j}\frac{\partial U_j}{\partial x_i}, \tag{7.1}$$

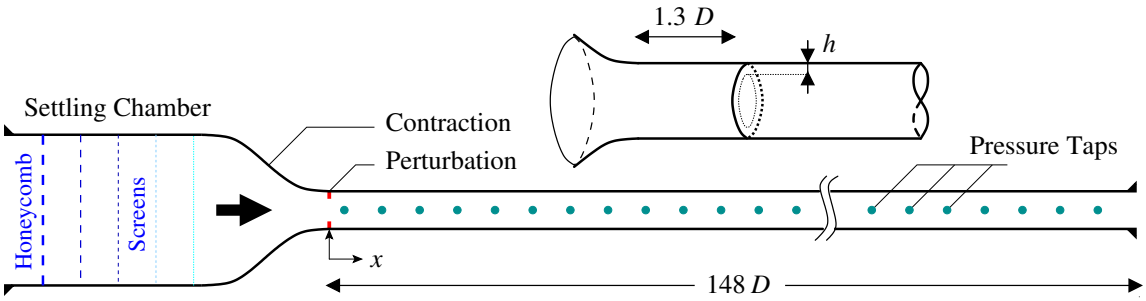

Figure 7.1: Schematic diagram of the pipe flow facility. The inset shows a detailed view of the ring perturbation.

where the pressure $P = \bar{p} + p'$, $U = \bar{u} + u'$ and ρ is the fluid density. Hence, decomposing the equation (7.1) results in the following pressure fluctuation equation:

$$\frac{1}{\rho}\nabla^2 p' = -2\frac{\partial^2}{\partial x_i \partial x_j}\left(u_i' \bar{u}_j\right) - \frac{\partial^2}{\partial x_i \partial x_j}\left(u_i' u_i' - \overline{u_i' u_j'}\right). \tag{7.2}$$

The right hand side in equation (7.2) contains two terms, that have different behaviour. The first term represents the interaction between the gradient of the mean velocity field and the gradient of turbulent velocity field. The second term represents turbulence-turbulence interaction. This clearly shows a link between the mean velocity gradient, velocity fluctuations, the pressure and how they redistribute the turbulence between various fluctuating components.

The goal of the present investigation is to measure the pressure along the pipe for a wide range of Re. In the first part, the experiment and the wall pressure measurement system are briefly described. In the second part, the results for the wall mean and fluctuating pressure are discussed. Then, the effect of the ring perturbation is presented. Finally tuft visualisation in the inlet region and developed turbulent region are shown.

7.3 Experimental set-up

7.3.1 Cottbus Large Pipe test facility (CoLaPipe)

The CoLaPipe (Cottbus large pipe test facility) has a diameter of $D = 190 \pm 0.3$ mm, length of 28 m ($148D$) long and was constructed from 13 acrylic sections of 2 m long and 5 mm thick. The sections were initially aligned using a laser and attached using bolts and nuts. Gaps or leaks are prevented using insulating tape. Figure 7.1 presents a schematic sketch of the test section. The air flow is driven using a radial blower of 45 kW. The pipe is mounted on a closed loop containing a cooling system to maintain constant temperature. All the experiments were conducted at $20 \pm 1°$C. At the inlet of the pipe, the flow passes through a settling chamber with honeycombs, screens and meshes to damp fluctuations [5, 12]. Moreover, a smooth inlet contraction section is used, designed using a fifth order polynomial. The Bernoulli's equation is used to calculate Re by using the mean pressure values obtained before and after the contraction section. At the exit of the contraction, the streamwise turbulence intensity is less than 0.5%. The current experimental setup has a working range of $6 \times 10^4 < Re < 10^6$ (5 to 80 m/s). It corresponds to $0.2 < u_\tau < 3$ m/s, where u_τ is the friction velocity in fully developed flow: $u_\tau = \sqrt{\tau_w/\rho}$, and τ_w is the wall shear stress. More details about the facility can be found in [77] and [78].

7.3.2 Natural transition and orifice perturbation at the inlet

In classical turbulence studies, the pipes are tripped at the inlet and the measurements were conducted at $x/D \gtrsim 30D$ and $70D$ by [79] and [80], respectively, to assure the flow is turbulent. Here we used an orifice perturbation, that is a 2 mm thick aluminium annular ring. The inner radius of the ring is at a constant height h from the pipe wall. The natural transition corresponds to $h = 0$ and the perturbed cases correspond to $h = 4.5$, 9.5, 15.5 and 21.5 mm, which corresponds to area blockage pourcentage of 10, 20, 30 and 40%, respectively. This type of perturbation was already studied systematically in transition experiments [53]. The position of the perturbation is $1.3D$ from the exit of the contraction. By reanalysing the data from [14], figure 7.2 was obtained. It shows that the critical axial position of transition, x_c, decreases as Re is increased and scales as $x_c/D \propto Re^{-2.25}$.

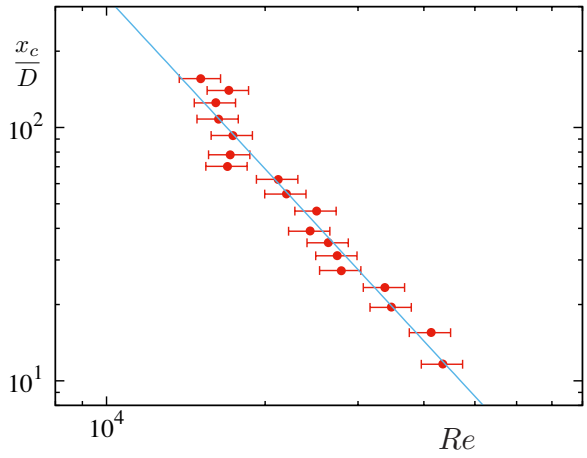

Figure 7.2: Critical position along the pipe axis for transition to turbulence as a function of Re. The reanalysis of the centreline velocity fluctuations as a function of Re for various x/D, from [14], shows that the critical position for transition, x_c, decreases with Re. The continuous line is a power law fit to the data described in the text.

7.3.3 Wall pressure measurement system

The wall pressure in the facility is measured using pressure taps. It has an pinhole diameter, d, of 400 microns. Pressure taps are available along the pipe on 41 locations. At each location, three pressure taps are installed around the circumference. The pressure is measured using a piezo-electric transducer (Measurement Specialities Model 9116) mounted behind the pinhole. To minimise the error of measurements, particular criteria were reached: (i) the diameter of the pressure tap should be small, when compared to the length scale in the flow, i.e., $d^+ = du_\tau/\nu < 20$ [81, 82]. Experimental results presented here were conducted in the range of $8 < d^+ < 47$. (ii) The length of the pressure tube ($\mathcal{L}$) used for each of the pressure tap should be equal in length to avoid the problem of fluctuation damping due to the tube walls. In our case we used 2 meter long tubes to connect to the pressure transducer. (iii) The length of the pressure tube ($\mathcal{L}$) to the pinhole diameter, d, should be greater than 2 ($\mathcal{L}/d > 2$) [83]. All pressure measurements are taken using a pressure scanner with a range of 7 kPa (from Measurement Specialities Model 9116), connected through an Ethernet cable. Five to ten channels are simultaneously measured and the acquisition is performed using LabView. Each pressure signal is 10 000 samples at a frequency of 100 Hz. Initially, 50 000 samples were acquired to determine the pressure fluctuations. With 10 000 samples, we found a deviation of the fluctuations about 1.2%.

7.4 Results and discussion

7.4.1 Friction factor results for fully developed turbulent pipe flow

To validate further the experiment, the friction factor, $\lambda_f = -\frac{dP}{dx}\frac{2D}{\rho U^2}$, as a function of Re is measured in the downstream of the pipe, where flow is fully developed, and is shown in figure 7.3(a). λ_f was calculated with 5 points averaging method using the pressure data in the region $70 < x/D < 130$. The error bars represent the total uncertainty in the measurements, which are based on 5 rehearsals, that indicate a maximum error on Re of 9.6% and on λ_f of 5.6%. The friction factor relationship proposed by Prandtl can be derived from the integration of the mean velocity profile. This relation can be written as:

$$1/\lambda_f^{1/2} = C_1 \log\left(Re\lambda_f^{1/2}\right) + C_2 \tag{7.3}$$

where C_1 and C_2 are coefficients, which may or may not depend on Re. If $C_1 = 2.0$ and $C_2 = -0.8$, then (7.3) is the same as that derived by Prandtl from the smooth-pipe data of [10]. In figure 7.3(b), a least-squares approximation was used on our data to determine the values for the coefficients: $C_1 = 2.0$ and $C_2 = -0.18$. The argument that the coefficients in (7.3) are independent of Re is based on two assumptions: (i) a log law exists, and (ii) the contribution of the near-wall region to the average velocity is negligible. In figure 7.3, we also plot the variation of λ_f with Re along with the skin friction formula

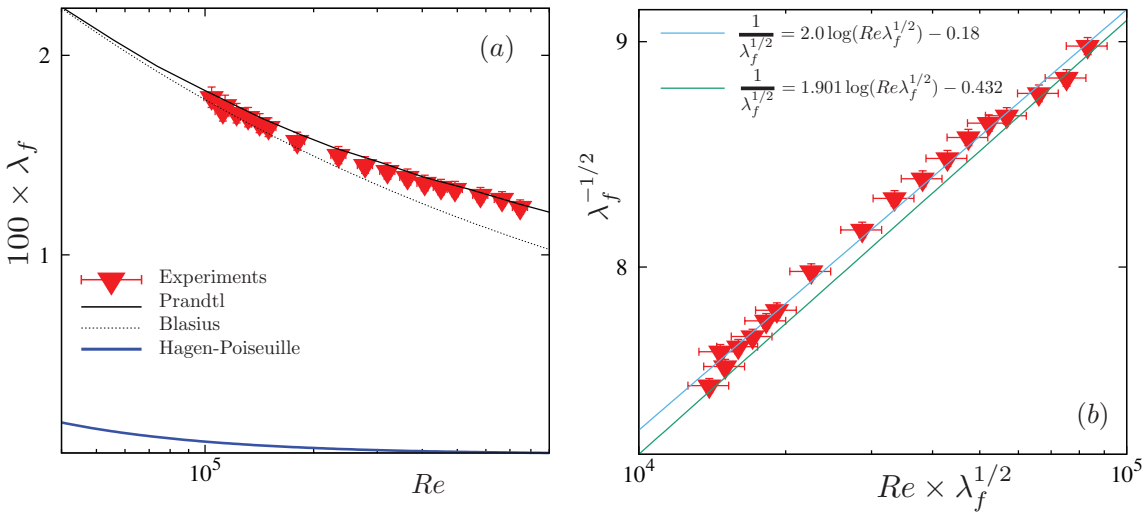

Figure 7.3: Friction factor, λ_f, in fully developed turbulent flow. (a) λ_f as a function of Re. (b) $\lambda_f^{-1/2}$ as a function of $Re \times \lambda_f^{1/2}$. The bottom line is the Prandtl fit for [11] smooth pipe data and the top line is a fit to the present experiments.

proposed by [84]:

$$\lambda_f = 0.3164/Re^{1/4} \tag{7.4}$$

which is considered accurate only up to $Re \leqslant 100\ 000$.

7.4.2 Pressure fluctuations along the pipe

7.4.2.1 Pressure fluctuations along the pipe without ring perturbation

The facility allows for measurements of the wall static pressure: $P = \bar{p} + p'$, where $\bar{p}$ is the mean pressure and p' is the fluctuation. Figure 7.4(a) shows the mean pressure difference from the outlet, $\bar{p}_e$, as a function of the axial position, x/D. It decreases monotonously from the inlet and the slope depends on Re, because there is a strong pressure gradient that drives the flow. However, the mean pressure, $\bar{p}$, does not convey any information about the transition to fully developed turbulence. Hence, the behaviour of fluctuations, p', should be explored. Figure 7.4(b) presents the standard deviation of pressure fluctuations, p', normalised by pressure difference at the contraction, Δp, along the pipe for different Re. Δp is the pressure drop between the inlet and the outlet of the contraction. The outlet of the contraction is the inlet of the pipe ($x = 0$). At the inlet, $p'/\Delta p$ is small and increases with the axial position before reaching a steady state value. In general, the value of p' increases with Re, however when normalised by Δp, it decreases in a self-similar way.

To investigate this self-similar growth, different scalings can be implemented [83]. In figure 7.4(c), p'^+ is shown as a function of x/D, where $p'^+ = p'/\rho u_\tau^2$ and $u_\tau^2 = \lambda_f U^2/8$ is the friction velocity from the fully developed turbulent region. Only a partial collapse of the data is observed and the most striking observation is the exponential increase of the pressure fluctuations close to the inlet region. The p'^+ data can be fitted using an exponential fit: $p'^+ = \alpha + \beta \exp(\gamma x/D)$, which is in a good agreement with the exponential growth of the energy norm in the simulations of [15] in developing turbulent pipe flow. The parameter γ decreases with Re. Further, one can normalise the data using the asymptotic value of the exponential, i.e. $p'^+_\infty = \alpha$, as shown in figure 7.4(d). It indicates that the curvature of the exponential growth shifts toward low x/D for large Re, as indicated by the arrow. This is in qualitative agreement with the experiments of [14] that found an abrupt decrease of the critical position for transition as Re increases (see figure 7.2).

7.4.2.2 Pressure fluctuations along the pipe with ring perturbation

One can wonder if the exponential growth of pressure fluctuations along the pipe (see figure 7.5) is robust to perturbation. Figure 7.5 presents the standard deviation of wall pressure fluctuations along the pipe for different Re and each plot corresponds to a case where a ring perturbation is placed at

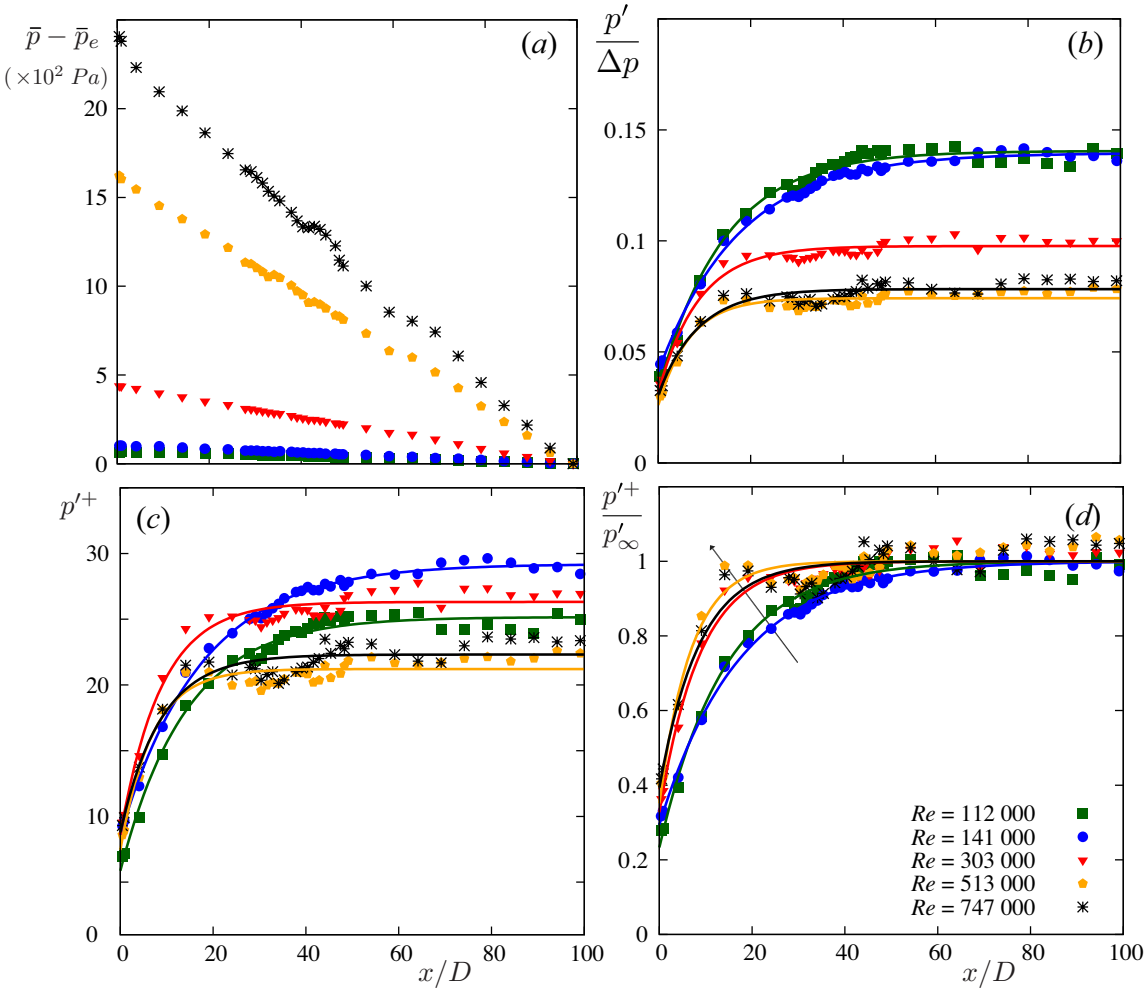

Figure 7.4: Wall mean pressure and fluctuations along the pipe without perturbation: (a) $\bar{p} - \bar{p}_e$, (b) $p'/\Delta p$, (c) p'^+ and (d) p'^+/p'_∞ versus x/D for different Re. The arrow indicates the direction of decreasing curvature.

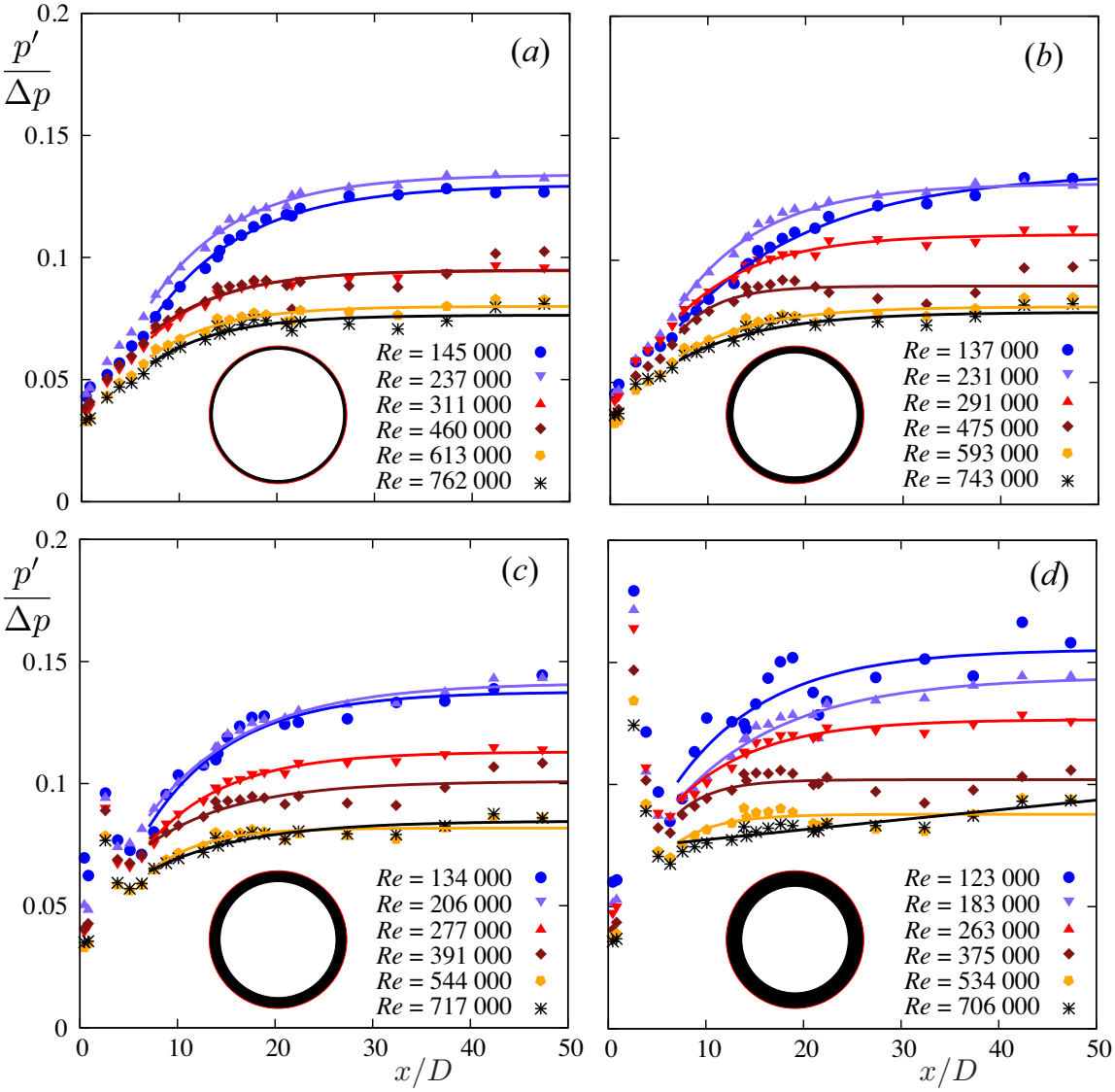

Figure 7.5: Wall pressure fluctuations, $p'/\Delta p$, along the pipe, x/D, for different Re with ring perturbations at $1.3D$ from the inlet. The perturbation makes a area obstruction of (a) 10, (b), 20, (c), 30 and (d), 40%. The insets are sketchs of the ring obstruction.

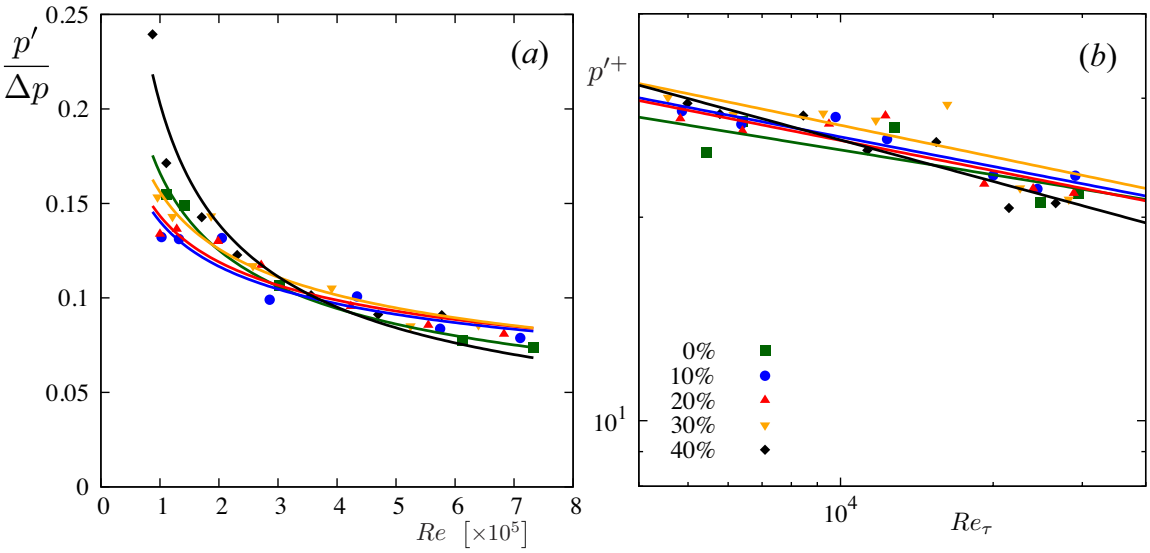

Figure 7.6: Wall pressure fluctuations as a function of Re in the saturated region for different perturbations: (a): $p'/\Delta p$ and (b) p'^{+}.

$1.3D$ from the inlet. Each perturbation corresponds to an obstruction of 10, 20, 30 and 40% of the pipe cross-section area, as sketched in the insets of figure 7.5. It has a strong effect locally, which can be quantified through a sudden peak at $x/D = 1.3$ to 8 corresponding to a flow separation region. However, downstream ($x/D \gtrsim 10$) the pressure evolves exponentially as in the case without perturbation. Our results indicate a systematic increase of $\Delta p'/p$ between the unperturbed flow and the perturbed cases. It is in agreement with the experiments of [85] for $Re = 180\ 000$.

7.4.2.3 Pressure fluctuations as a function of Re

In figure 7.6, we present the variation of pressure fluctuations as function of Re for different perturbation cases. Here p' is an average of three points in the saturated region around $x/D = 50$. The figure 7.6(a) clearly shows that the $p'/\Delta p$ decreases as a function of Re. The best fit is a power law with an exponent around -0.13. The pressure fluctuation, p', is normalised by ρu_τ^2, as shown in figure 7.6(b) as a function of Re_τ, where Re_τ is $\rho u_\tau/\nu$. One might observe that the data collapses, suggesting the fully developed turbulent flow to be independent of the annular perturbation. The decrease in the pressure fluctuation when compared to a turbulent boundary layer flow [83, 86, 87], might be due to the velocity overshoot that is found in the inner region of turbulent pipe flow [14]. This velocity overshoot is absent in terms of channel flow and turbulent boundary layer flow. The smooth curved surface of the pipe interior contributes to the interchange of counter-rotating vortices towards the pipe core, strongly influencing the flow structure in the inner region as well as in the core of the pipe flow.

Spectra have been measured before [88–93] where the focus was on sound production, acoustic effects, compressible effects and vibroacoustic response of thin cylindrical shells.

7.4.3 Tuft flow visualisation

In order to further understand the flow in the inlet section, tuft flow visualisation was carried out and images are presented in figure 7.7. One can see that the wool tuft oscillates as it is a flexible filaments freely hanging in the flow. The tuft is inserted through a pressure tap. Away from the tuft holding position, the tuft is stretched and it does not touch the wall. When the flow velocity is small, the filaments inclines along the flow. Then, above a critical value of Re, the filaments exhibit oscillations. It is observed that the amplitude of the oscillation are small in the inlet region and comparatively 20% larger downstream. It is then assumed that the amplitude is proportional to the pressure fluctuation and related to the formation of wall vortices arising in the inlet [15].

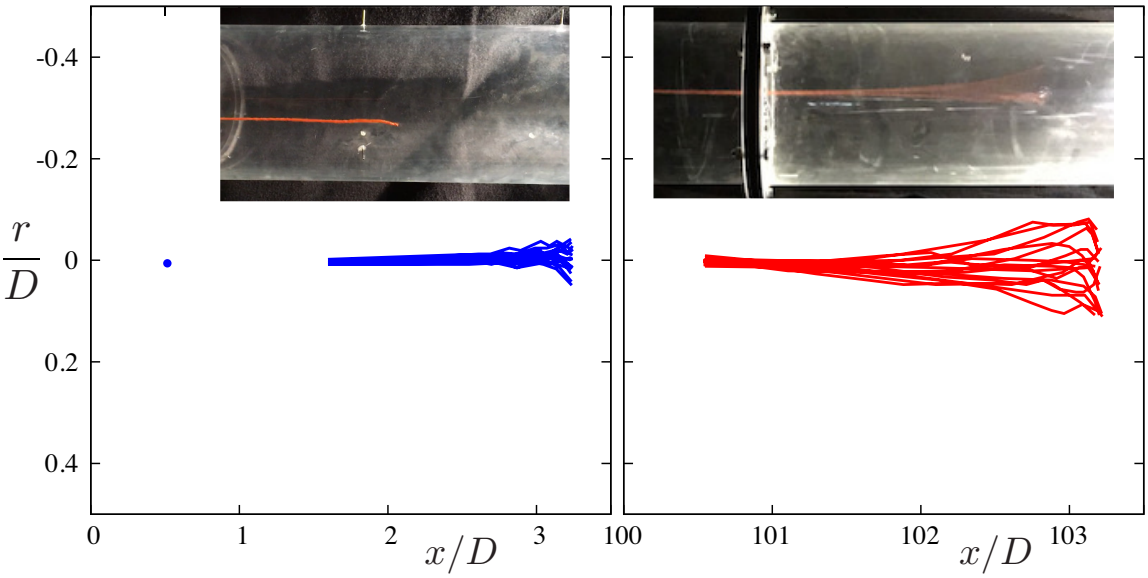

Figure 7.7: Tuft visualisation in the streamwise plane without ring perturbation. The tuft is 50 cm long ($2.63D$) for $Re = 445\ 000$. (a) Superposed view of the tuft filament, pinned at $0.65D$ from the inlet. (b) View at $100D$. The insets are snapshots of the tuft. Note the increase of the amplitude of the flapping. Flow is from left to right.

7.5 Conclusions

The behaviour of pressure was studied in a developing turbulent pipe flow. Both the mean pressure measurements and the pressure fluctuations were discussed in detail. It was observed that the pressure fluctuations have an exponential growth along the pipe with the axial position. This evolution indicates that the growth of the energy is faster than simple diffusion between the wall pressure fluctuations and the mean flow. This agrees with the non-isotropic or wall turbulence view of pipe flow. Then the growth saturates in the so-called developed turbulent region.

There, the root-mean-square values of the wall pressure normalised by the inner variables are found to be decreasing as a function of Re. Finally, tuft visualisations were performed to confirm flow fluctuations at different positions along the pipe. The measurements showed that the amplitude of tuft oscillations increases as the flow goes downstream suggesting wall vortices arising from the wall.

Chapter 8

Conclusion

8.1 Conclusion

Expansion pipe flows have many industrial application, this thesis explores the numerical simulation of two dimensional and three dimensional expansion pipe flows to understand the behaviour of finite-amplitude perturbation. Initially a global stability and sensitivity analysis were carried out on a two dimensional sudden expansion and gradual expansion, which showed that the first instability is a symmetry breaking bifurcation. Sensitivity analysis showed that the most sensitive region of expansion flow lies in the expansion region and the close to the shear layer. This showed us that any perturbation close to this section can have transient growth due to convective instability mechanism.

A three dimensional expansion pipe flow is simulated using a spectral element code with a finite amplitude perturbation at the inlet. Initially at low Reynolds number the flow creates a linear asymmetry growth of the recirculation region occurs. As the Reynolds number is increased, the recirculation region starts oscillating. At Reynolds number greater than 1680, the recirculation region breaks to form localised turbulence in the outlet section of the pipe. Above the transition Reynolds number a route to the sub-critical turbulent flow is established, and remains unchanged if the small perturbation is removed. It was found that both axisymmetric states and turbulent motion coexist over a range of Reynolds number. This property of localised turbulent flow with laminar inlet profile forming localised turbulence and decaying in the outlet section agrees with experiments. The localised turbulence does not convect downstream but holds a stable axial position. Structure within the localised turbulence is further studied using spatial correlations, which identifies fast and slow streaks that dominate the coherent structures. The flow tends to be more active in the centre region than near to the walls.

Later, the tilt perturbation is replaced with a vortex perturbation that satisfies the continuity boundary condition at the inlet. The behaviour of the flow due to the strength of the perturbation is explored. For relatively small perturbation amplitude, a patch of turbulence in the outlet section is observed to drift downstream, then decays upon the appearance of another patch of turbulence upstream. The process repeats quasi-periodically or stochastically as the amplitude of the perturbation strength is increased. Further, the turbulent patch that forms first appears via a low order azimuthal mode resembling an optimal perturbation. The turbulent patch formation is different from the puff splitting behaviour observed in uniform pipe flow, as here the new patches arise upstream of existing turbulent patches. At large perturbation strength, the patch does not drift downstream, but holds a stable spatial position forming localised turbulence. The structure within the localised turbulence is further studied using proper orthogonal decomposition, which indicates that the first mode comprises most of the energy and the flow is more active in the centre region than near the wall.

Applying vortex perturbation to straight pipe flow also triggers turbulence, velocity and pressure fluctuations along the pipe are studied. Divergence of Navier-Stokes equations reveal that the pressure fluctuations and the velocity fluctuations are strongly coupled. The simulations are aimed at studying the statistics of the fluctuations along the stream wise direction and to understand the correlation between the fluctuating components.

Since the study of velocity fluctuations in turbulent pipe flow are largely available, new experimental measurements from Cottbus Large Pipe Facility are presented. Mean pressure and the pressure fluctuations growth were discussed in detail. It was observed that the pressure fluctuations have an exponential growth along the pipe with the axial position.

The position of the pressure fluctuations saturation tends to be in agreement with the velocity fluctuations in variance in streamwise direction. Growth of the pressure fluctuations saturates in the

so-called developed turbulent region. The position of saturation tends to be in agreement with the statistical invariance of the velocity fluctuations in streamwise direction. Applying tripping device close to the inlet, shift the saturation point closer to the inlet section. Finally, tuft visualisations were performed to confirm flow fluctuations at different positions along the pipe. The measurements showed that the amplitude of tuft oscillations increases as the flow goes downstream suggesting wall vortices arising from the wall.

8.2 Future perspective

Certain question are still remain unanswered, which could be explored in the future for expansion pipe flows. Even though the present study offers only a few insights, it opens up many other directions for further research. . In case of a sudden expansion pipe flow, the localized turbulence patch has a length of $\approx 5d$, but experimental investigation of narrow diverging pipes have a turbulent patch that extends all along the expansion section. Numerical simulation with slowly diverging angle could help us answer this question. One another important factor to look for, is to check if these long turbulent patches can split itself.

When the angle of divergence tends to zero, the expansion pipe flow becomes a straight pipe flow. The stability of straight pipe flow lies at infinity, a clear understanding or relation between the two different pipe flow could be made. Is it possible to build a regime map between the straight pipe flow and the expansion flow?

The vortex perturbation has only been tested for variation of strength, a complete study by varying the Reynolds number is required to understand the real effect of it. Even the size of the vortex perturbation along with its position at the inlet should be studied to clearly understand its effect. In this thesis only expansion section of ratio 1:2 is explored, a detailed investigation of effect of expansion ratio on the localised turbulence is also required.

The effect of geometric deformation of the inlet, is interesting to study, which could resemble very close to the experiments. Even though proper orthogonal mode decomposition gives the most energetic mode, it does not give any information about the dynamics. Application of Dynamic Mode Decomposition on the localized turbulence could give more insight about the behaviour.

Experimental investigation for identification of developed turbulence has shown the statistical invariance of fluctuations along the axial directions, a detailed numerical simulation by triggering turbulence using vortex perturbation could help understand the wall fluctuations behaviour.

Resumé

Les écoulements dans des tubes ou des conduites ou les tuyaux circulaires qui ont un diamètre d'entrée petit et un diamètre de sortie plus grand sont appelés élargissements ou divergents. Ces écoulement dans des élargissements ou divergents ont été peu étudiés du point de vue des simulation numériques. Cette thèse présente des résultats de simulations numériques directes des équations de Navier-Stokes pour ces écoulements dans des élargissement. La différence principale entre un écoulement dans une conduite droite et un élargissement est l'apparition d'une zone de recirculation. EIle est forme lorsque l'écoulement se détache du tube de petit diamètre et se rattache en aval à la paroi dans le tube de grand diamètre. Cette zone de recirculation croît linéairement en fonction du nombre de Reynolds. Cette croissance de la région de recirculation ne permet pas l'utilisation de conditions aux limites périodiques pour les simulations numérique. Par conséquent, il est nécessaire d'utiliser un grand domaine de calcul pour contenir la zone de recirculation lorsque le nombre de Reynolds est élevé, ce qui à son tour augmente le coût du calcul. Ici, le nombre de Reynolds est défini par: $Re = Ud/\nu$ avec U la vitesse d'entrée, d le diamètre d'entrée et ν la viscosité cinématique.

Le nombre Reynolds critique de la transition vers la turbulence pour un écoulement dans un élargissement prédit par l'analyse linéaire de stabilité ($Re > 3477$) est plus élevé que celui observé expérimentalement. Ce décalage entre les expériences et la théorie linéaire de stabilité est due à la présence d'imperfections dans le dispositif expérimental, qui fournit une amplitude de perturbation finie à l'écoulement. Analyse de la croissance transitoire ont montré que le mécanisme d'instabilité convective amplifient la perturbation qui pourrait provoquer un chemin plus court vers la turbulence. Les expériences ont montré la formation de tâches de turbulence à proximité de la section d'élargissement qui se relaminarise en aval. L'un des moyens efficaces pour déclencher une turbulence dans les simulations numériques consiste à mimer les expériences, en ajoutant une perturbation d'amplitude finie.

Une étude de stabilité dans un élargissement bi-dimensionnel a été réalisée afin de comprendre la sensibilité des perturbations et l'effet de la taille du domaine. L'analyse globale de la stabilité est faite pour identifier les paramètres les plus instables de la sensibilité aux valeurs propres et structurelle de celui-ci. Tout d'abord, la bifurcation se produit à un Reynolds critique, $Re_c = 143$, ce qui est une bifurcation de rupture de symétrie et n'a aucun élément oscillant (bifurcation stationnaire). Cette bifurcation provoque un gonflement l'écoulement sortant vers une paroi dans la section élargie. La taille de la zone de recirculation augmente d'un côté et diminue sur l'autre côté. En calculant le mode adjoint, le paramètre de sensibilité structurelle peut être calculée. On a constaté que la zone proche de la section d'expansion est très sensible à toute perturbation due à la présence d'une couche de cisaillement. De même, l'élargissement progressif avec un angle de 10° montre que l'apparition de la région de recirculation dépend de l'angle de divergence. Pour ce divergent, la première bifurcation se produit à $Re_c = 475$, ce qui est similaire à celle de l'élargissement brusque, mais la région de la sensibilité structurelle tend à occuper toute la zone d'élargissement.

Nous présentons des résultats obtenu pour des simulations numériques directes tridimensionnelles pour un élargissement progressif ou divergent. Les simulations ont été réalisées avec un profil de vitesse de type Hagen-Poiseuille à l'entrée, sans glissement à la paroi et une condition de contraint libre à la sortie du domaine. Afin de déclencher la turbulence, une perturbation d'amplitude finie n'est ajoutée à l'entrée au profil de vitesse de Hagen-Poiseuille. Si cette perturbation est pas appliquée à l'entrée, l'écoulement reste laminaire et axi-symétrique. Une perturbation de type inclinaison est appliquée dans le sens transversal. Pour un nombre de Reynolds petit, mais fini, la perturbation crée une croissance de l'asymétrie de la zone de recirculation, qui est quantifiée en mesurant le barycentre de la distribution de vitesse dans le sens de l'écoulement. L'asymétrie croît en racine carrée de Re, ceci confirme une transition de type super-critique que l'on retrouve dans les expériences. Enfin, à une certaine valeur du nombre de Reynolds, la région de recirculation commence à osciller et se brise pour devenir une tâche

turbulente. Cette turbulence a tendance à se maintenir à une position axiale constante à proximité de la section d'élargissement et se relaminarise lorsqu'elle se déplace vers l'aval. Un profil de vitesse parabolique (de Hagen-Poiseuille) est récupéré en aval dans la section de sortie. La tâche de turbulence localisée a tendance à occuper la même position axiale, même si sa taille augmente avec Re. En supprimant la perturbation, la tâche de turbulence localisée s'auto-entretien indiquant ainsi l'existence d'une gamme de Re correspondant à un régime hystérétique. La corrélation spatiale dans la tâche de turbulence localisée révèle que presque toute l'énergie cinétique de l'écoulement est due à l'écoulement du jet central. Ceci est différent du *puff* turbulent observé dans la conduite de section constante.

L'application de la perturbation de type inclinaison à l'entrée crée une discontinuité et ne brise pas la symétrie de l'écoulement. Afin de satisfaire l'équation de continuité, un perturbation de type vortex a été sélectionné. La taille de la maille pour le domaine de calcul est également augmentée, afin de tenir compte des petites structures à grande échelle qui sont rejetés en raison de la perturbation de rotation. Le vortex est défini par sa taille et son amplitude à l'entrée en même temps que l'écoulement de Hagen-Poiseuille. Afin d'étudier le comportement de cette perturbation de type vortex, la taille a été fixée et l'amplitude de la perturbation est variée. A faible amplitude, le vortex se relaminarise avant d'atteindre la zone d'élargissement. Lorsque l'amplitude augmente, l'écoulement devient unstable. En amont de la tâche de turbulence localisée, on observe la formation d'une structure ondulatoire réminiscente de la perturbation optimale calculée par d'autres auteurs. Ces tâches de turbulence apparaissent quasi périodiquement et se relaminarisent lorsqu'elles se déplacent en aval. Pour une amplitude critique de la perturbation de type vortex, position de la tâche de turbulence commence à osciller axiallement à proximité de la zone d'élargissement et occupe finalement une position stable. Enfin, la décomposition en modes propres est effectuée sur la tâche de turbulence localisée et montre que le mode le plus énergique se trouve au centre de l'écoulement. Ces éléments ainsi que l'étude de corrélation spatiale de la tâche de turbulence montre clairement que la turbulence localisée gagne son énergie du flux primaire sortant du tuyau d'entrée.

Récemment, des simulations numériques directes de grande résolution et fort Re dans des tubes de section constante ont montré que les perturbations d'amplitude finie s'amplifie de façon exponentielle avant de déclencher des tâches turbulentes. Ainsi, nous présentons les résultats de l'étude à l'aide d'une perturbation de type vortex dans un écoulement dans un tube (de section constante circulaire) droit. Dans un premier temps, la turbulence est déclenchée en raison de la perturbation à l'entrée et la position de la turbulence développée est mesurée. Ici, nous avons l'intention d'étudier le comportement des fluctuations de la vitesse et de la pression le long de l'entrée du tuyau jusqu'à la position de turbulence développée. Dans la littérature, des étude s expérimentales sur l'identification de la position axiale pour l'établissement de la turbulence développée par les fluctuations de vitesse sont disponibles. A l'aide de l'installation CoLaPipe (Cottbus Large Pipe), nous avons réalisé des expériences pour mesurer la fluctuation pression à la paroi. On a constaté que la pression de paroi moyenne diminue à mesure que l'écoulement se déplace vers l'aval. De plus, les fluctuations croîent de façon exponentielle et atteignent un point de saturation. La position axiale de la saturation des fluctuations de pression sont en accord avec la position de la turbulence développée mesurée à partir de la vitesse sur l'axe de la conduite. La croissance exponentielle des fluctuations de pression a tendance à avoir un comportement auto-similaire par rapport à Re. Des simulations numériques au nombre de Reynolds modéré sont effectués pour vérifier ce comportement.

Appendix A

Mathematical concepts

A.1 Approximation of partial differential equations

A.1.1 Strong form of partial differential equation

To explain the structure of weight residual method, consider a domain Ω with external boundary Γ and assume that $f : \Omega \to \mathbb{R}$ is a given function. The strong of the partial differential equation is given by:

$$\begin{cases} \mathcal{L}u - f = 0 \quad \text{in} \quad \Omega \\ \\ u = u_\Gamma \qquad\quad \text{on} \quad \Gamma \end{cases} \tag{A.1}$$

where $\mathcal{L}$ is a continuous positive-definite differential operator . consider the Poisson equation:

$$\begin{cases} -\dfrac{\partial^2 u}{\partial x^2} - f = 0 \quad \text{in} \quad [0,1] \\ \\ u(0) = 0 \qquad u(0) = 1 \end{cases} \tag{A.2}$$

A.1.2 Application of weight residual method

If a set of trial functions, denoted by U, is defined as $U = \{u \mid u \in H^2(\Omega), u = u_\Gamma \text{ on } \Gamma\}$ and a set of test functions, denoted by V, is defined as $V = \{v \mid v \in L^2(\Omega), v = 0 \text{ on } \Gamma\}$, where H is the sobolev space of functions equipped with L^p-norms. Then equation (A.1) can be written as:

Find $u^h \in U^h$ *such that*:

$$(\mathcal{L}u - f, w) = 0 \quad \forall_{w \in W} \tag{A.3}$$

Equation (A.3) form ensures that the projection of function $\mathcal{L}u - f$ on W to be zero. By using $L^2(\Omega)$ inner product (A.3) takes the form:

Find $u^h \in U^h$ *such that*:

$$\int_\Omega (\mathcal{L}u - f) w d\Omega = 0 \quad \forall_{w \in W} \tag{A.4}$$

A finite dimensional subspace $U_h \in U$ with basis $\phi_i, (i = 0, ..., N)$ is chosen for discretization. The solution can be written as a truncated series using the trail function ϕ_i as basis function. The approximate solution $u^h \in Uh$ is then written as:

$$u^h = \sum_{i=0}^{N} c_i \phi_i \tag{A.5}$$

An exact differential $\mathcal{L}$ operator or a discrete differential operator $\mathcal{L}^h$ can be used by the choice of the space U^h. Substituting the a discrete differential operator in equation (A.1) gives:

$$\mathcal{L}^h u^h - f = r^h \quad \text{in} \quad \Omega \tag{A.6}$$

where r^h is called the residual of the equation. The expansion coefficient c_i are the unknowns that are obtained by projecting the residual to zero using the L_2-norm as: $(r^h, w)_W = 0, \forall_{w \in W}$. Since the approximate solution is an element of finite dimensional subspace of U, even the test function can be reduced to finite dimensional subspace $W^h \in W$. ψ_j is the basis function for the test function such that $W^h = \psi_{i=0}^N$ and the discrete weight residual form reads:

Find $u^h \in U^h$ *such that*:

$$\left(\mathcal{L}^h u^h - f, w^h\right)_W = 0 \quad \forall_{w^h \in W^h} \tag{A.7}$$

By applying L_2-inner product, *Find* $c_i, (i = 0, ...N)$ *such that*:

$$\sum_{i=0}^{N} c_i \int_\Omega (\mathcal{L}^h \phi_i)\psi_j d\Omega = \int_\Omega f\psi_j d\Omega \quad j = 0, ..., N \tag{A.8}$$

Equation (A.8) can be written in matrix form as:

$$\mathbf{Lc} = \mathbf{f} \tag{A.9}$$

with:

$$Lij = \int_\Omega (\mathcal{L}\phi_j)\psi_i d\Omega \tag{A.10}$$

$$f_i = \int_\Omega f\psi_i d\Omega \tag{A.11}$$

where $\mathbf{c} = [c_0, ..., c_N]^T$, $\mathbf{f} = [f_0, ..., f_N]^T$. The coefficient c_i is obtained by solving the set of equations (A.9). The approximate solution u^h is then obtained by substituting c_i in (A.5). The choice of test function ψ_j determine the type of discretization method.

A.1.3 Weak formulation

By applying integration by part to weight residual form (A.3), a bilinear form $a(u, w)_w$ can be obtained such that (A.1) can be written as:

Find $u \in U$ *such that* :

$$a(u, w)_w = (f, w)_w \qquad \forall_{w \in W} \tag{A.12}$$

In case of Poisson equation (A.2):

$$a(u, w)_w = (\frac{\partial u}{\partial x}, \frac{\partial w}{\partial x})_w \tag{A.13}$$

According to Lax-Milgram theorem, a unique solution u exists to the partial differential equation if the bilinear form $a(u, w)$ is coercive on W (positive definite) and bounded. For more details on the theorem, please refer to Appendix of [94]. The reason to call it weak form is that the solution u which was initially in $H^2(\Omega)$, after application of variational formulation the inner product $(\frac{\partial u}{\partial x}, \frac{\partial w}{\partial x})$ requires that both $U \subset H^1(\Omega)$ and $W \subset H^1(\Omega)$. The other advantage of the weak form is that the application of boundary condition on the domain is easier.

A.1.4 Galerkin Methods

If the finite dimensional test function U^h and the train function W^h are chosen to be the same and applying the variational formulation (A.3), then the method is termed as Galerkin weight-residual method. The approximation of the bilinear form is given by:

$$a(u^h, w^h)_w = (f, w^h)_w \qquad \forall_{w^h \in W^h} \tag{A.14}$$

Considering u as the exact solution of the (A.3) and $U^h \subset U$

$$a(u, w^h)_U = (f, w^h)_U, \qquad \forall_{w^h \in U^h} \tag{A.15}$$

Subtracting (A.14) from (A.15) gives:

$$(\mathcal{L}(u^h - u), w^h)_U = 0, \qquad \forall_{w^h \in U^h} \tag{A.16}$$

Equation (A.16) can be interpreted key property that leads to error $e = u^h - u$ between the solution of the original problem and the Galerkin approximation is orthogonal to the finite dimensional subspace U^h. This method leads to linear system of equation, which can be construed into set of matrix that can be solved by computer program.

A.1.5 Numerical Integration

Integral formulas in the weak form are generally evaluated using simple trapezoidal rule. Higher order methods, however, requires higher order integration rules. The method expands the solution over a certain polynomial basis. Thus, they require the calculation of integral of polynomial of certain order. The quadratures derived from the requirement to be exact for all the polynomials of certain order are called Gauss quadratures. The general formula for numerical integration is given as:

$$\int_a^b p(\xi) f(\xi) d\xi = \sum_{i=0}^{N} w_i f(\xi_i) + R_N(f) \tag{A.17}$$

where $p(\xi)$ is the weight function of the integration satisfying $p(\xi) \geq 0$ and $\int_a^b p(\xi) d\xi > 0$ and $R_N(f)$ is the error of the quadrature. The Gauss numerical integration is formed in a such a way that to find w_i and ξ_i for a minimum error of the quadrature $R_N(f) \equiv 0$ for polynomials of the maximal possible degree. Equation (A.17) cannot be used for polynomial of order higher than $2N+1$ as it contains only $2N+2$ free parameters. Let $Q_0 = 1, Q_1, ..., Q_N, ...$ is the system of orthogonal polynomials with respect to the weight function $p(\xi)$, i.e.:

$$\int_a^b p(\xi) Q_i Q_j d\xi = \delta_i j, \qquad i, j = 0, ..., N, ... \tag{A.18}$$

with $\delta_i j$ being the Kronecker symbol. Note that for a given $p(\xi)$ the system Q_i is uniquely determined by (A.18). In case of finite element methods and spectral methods $p(x) = 1$ and the corresponding orthogonal system consists of the so-called Legendre polynomials. The reader is requested to refer [36, 37, 94] for other orthogonal polynomials that are used. Considering $\{\xi_i\}_{i=0}^N$ to be the zeros of Q_{N+1}, then (A.18) defines unique sequence $\{w_i\}_{i=0}^N$ such that it is exact for all the polynomials of order N. It can be proved [36, 94] that $R_N(f) \equiv 0$ for all the polynomials of order $2N+1$. Then the numerical integration formula for any arbitrary polynomial $\Phi(\xi) = Q_{N+1}(\xi) q(\xi) + r(\xi)$, for $q, r \in P_N$ of order $2N+1$, where P_N being the linear space consisting of all the polynomials of order less or equal to N is given as:

$$\int_a^b p(\xi) \Phi(\xi) d\xi \equiv \sum_{i=0}^{N} w_i \Phi(\xi_i) \tag{A.19}$$

It can also be interpreted as, if (A.17) is exact for all the polynomials of order $2N+1$ than $\{\xi_i\}_{i=0}^N$ must be the zeros of Q_{N+1} and $\{w_i\}_{i=0}^N$ is chosen by (A.19). In case of Legendre orthogonal weights and nodes of the quadrature are given by:

$$x_j = \text{zeroes of } L_{N+1} \qquad 0 \leq j \leq N \tag{A.20}$$

$$w_j = \frac{2}{(1 - x_j^2)[L_{N+1}(x_j)^2]} \qquad j = 0, ..., N \tag{A.21}$$

The above equation (A.21) is not valid for polynomial of order higher than $2N-1$ since equation (A.17) consist only of $2N$ free parameters. In order to take the boundary in to account and to be valid for polynomial of order $2N-1$, not exact for all polynomial $2N$ a quadrature can be constructed using the above method. The resulting quadrature is termed as Gauss-Labatto quadrature and its corresponding nodes and weights are given by

$$x_0 = -1 \qquad x_j = \text{zeroes of } L'_N \qquad x_N = 1 \leq j \leq N-1 \tag{A.22}$$

$$w_j = \frac{2}{N(N+1)} \frac{1}{[L_N(x_j)]^2} \qquad j = 0, ..., N \tag{A.23}$$

A.2 Spectral Methods

A.2.1 Fourier Spectral

In section (A.1.2), it was shown that the solution to a partial differential equation can expanded in a series of expansion functions:

$$u = \sum_{i=0}^{\infty} c_i \varphi_i \tag{A.24}$$

where c_i being the expansion coefficient and φ_i is the orthogonal set of trail function in case of spectral methods. The orthogonality with respect to a weight function w is defined by:

$$\int_{-1}^{1} \varphi_i(x)\varphi_j(x)w(x)dx = \delta_{ij} \tag{A.25}$$

Then the coefficients c_i in (A.24) are given by weighted inner product:

$$c_i = \frac{1}{\|\varphi\|^2} \int_{-1}^{1} u(x)\varphi_i(x)w(x)dx \tag{A.26}$$

with:

$$\|\varphi\|^2 = \int_{-1}^{1} \varphi_i(x)\varphi_i(x)w(x)dx \tag{A.27}$$

If $\varphi(x) = e^{ikx}$, then the method is called as Fourier spectral method, as $\varphi(x)$ is orthogonal in the interval $(0, 2\pi)$ with weight 1. If the solution u of the partial differential equation is infinitely smooth and periodic together with all its derivatives then the k^{th} coefficient of the expansion decays faster than any inverse power of k. This property of exponential decay of coefficients in trial functions is called spectral accuracy, in practice exponential decay of the coefficients never happens but can be made attainable by properly constructing the orthogonal set of functions. Another way of achieving exponential decay is by choosing the eigenfunctions of singular Sturm-Liouville problems defined on $\Omega = (-1, 1)$ as the trial functions. The general equation of singular Sturm-Liouville problems is given by:

$$-\frac{d}{dx}\left(a(x)\frac{d\varphi_i}{dx}\right) + b(x)\varphi_i = \lambda_i w(x)\varphi_i, \qquad a > 0, b > 0 \tag{A.28}$$

Jacobi polynomials like Chebyshev and Legendre polynomials are the solutions to (A.28). Using Jacobi polynomials, which are orthogonal, it can shown that an exponential convergence can obtained for infinitely smooth functions [36, 37].

$$\lim_{N\to\infty} \| u - P_N^h u \|_U = 0 \tag{A.29}$$

Then the finite expansion of the truncated series is given by:

$$P_N^h u = \sum_{i=0}^{N} c_i \varphi_i \tag{A.30}$$

In terms of spectral method, the convergence is achieved by increasing the order of the polynomial N.

A.2.2 Jacobi polynomials

If in the equation (A.28) we consider $a(x) = (1 - x^2), b(x) = 0$ and $w(x) = 1$ then the solutions are Legendre polynomials, given by the recurrence relation:

$$\begin{cases} L_0(x) = 1 \\ L_1(x) = x \\ L_{n+1}(x) = \frac{2n+1}{n+1} x L_n(x) - \frac{n}{n+1} L_{n-1}(x) \end{cases} \tag{A.31}$$

Figure A.1 shows the higher order polynomials that were created using a Python code (Appendix). The advantage of Legendre polynomial over the other orthogonal polynomials is that the weight function is w is given by $w(x) = 1$, which is easier to apply integration by parts in Galerkin formulations.

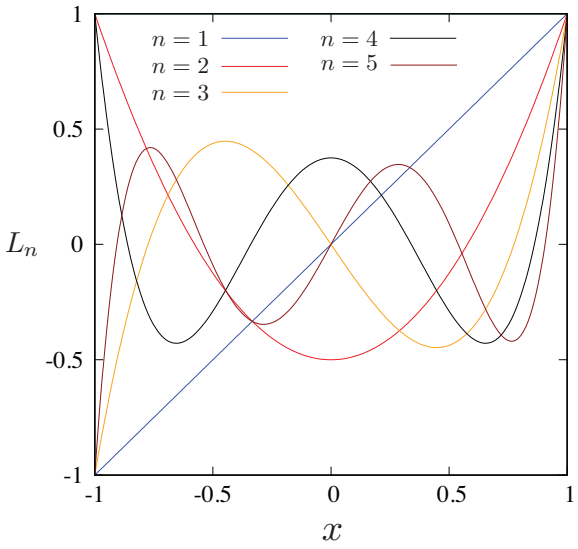

Figure A.1: Legendre polynomials for N= 1,...5

A.2.3 Pseudospectral method

The spectral method is nothing but transformation from the physical space to spectral space. The coefficients c_i in the spectral approximation depend on all the values of $u(x)$ in the physical space and can only be computed by numerical integration. In case of arbitrary functions $u(x)$, this cannot be done exactly. To overcome this problem a set of approximate coefficients $\hat{c}_i$ is obtained by using a an interpolating polynomial $\Pi_N^h u(x)$ of $u(x)$ defined by a finite set of interpolation points. The equation for interpolant is given as :

$$\Pi_N^h u = \sum_{i=0}^{N} \hat{c}_i \varphi_i \tag{A.32}$$

Then by applying the quadrature nodes and weight of Legendre polynomials, the discrete coefficients $\hat{c}_i$ can be approximated :

$$\hat{c}_i = \frac{1}{\|\varphi\|^2} \sum_{k=0}^{N} u(x_k)\varphi_i(x_k)w(x_k) \tag{A.33}$$

with:

$$\|\varphi\|^2 = \sum_{k=0}^{N} \varphi_i(x_k)\varphi_i(x_k)w_k \tag{A.34}$$

The spectral accuracy is retained even after the continuous transform is replaced by an interpolating polynomial (A.32)of Gauss-quadrature points. In practice, however, the interpolation polynomials are written as a linear combination of Lagrange interpolation polynomials through the Gauss-type quadrature points:

$$\Pi_N^h u = \sum_{i=0}^{N} u_i \varphi_i \tag{A.35}$$

in this way the coefficients are just given by the value of the function in the interpolation points $u_i = u(x_i)$.

A.2.4 Legendre-Gauss-Lobatto-Lagrange interpolation polynomials

The basicfunction ϕ_i of Legendre-Gauss-Lobatto-Lagrange (LGL) interpolation polynomials then are given by :

$$\phi_i = \frac{-1}{N(N+1)L_N(x_i)} \frac{(1-x^2)L'_N(x)}{x - x_i} \tag{A.36}$$

Figure A.2(a) shows basicfunction for N=2 LGL points and (b) for N = 6 points. In general using LGL-points along with Legendre polynomial is preferred, than any other orthogonal polynomials and interpolation points.

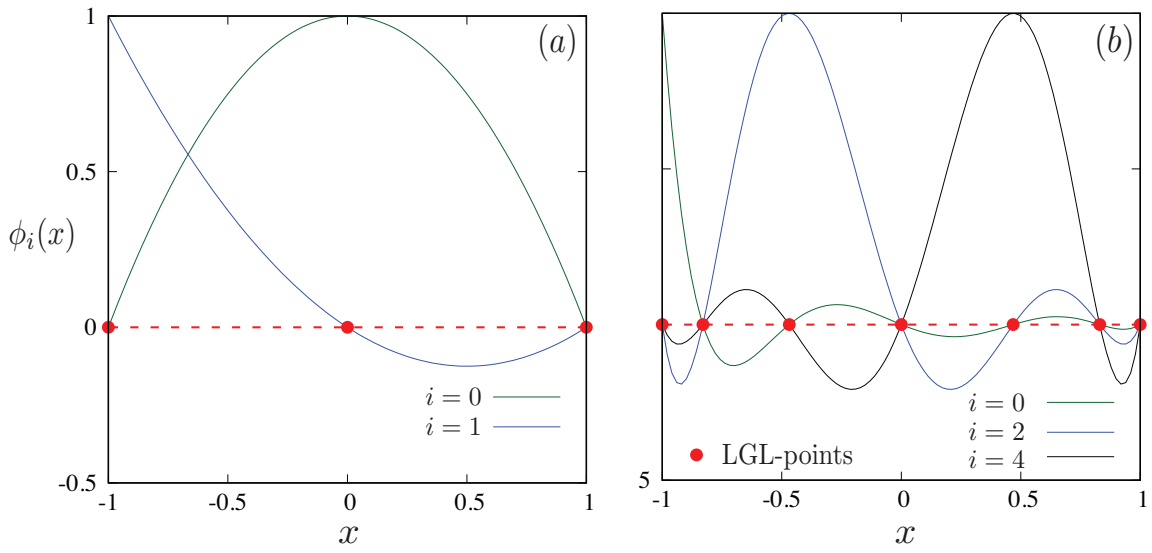

Figure A.2: Legendre polynomials for N= 1,...5

A.3 Spectral Element Method

Spectral element method, combines the advantage of FEM, which can be used to discretize complex geometries and that of the spectral methods to use higher order polynomial for faster convergence and accuracy. It was proposed by Patera [34], Initially the doamin is divided into N_el non-overlapping elements Ω_e

$$\Omega = \bigcup_{e=1}^{N_{el}} \Omega_e \tag{A.37}$$

Then the space of approximation $U^h = \{u \in U| \quad u_{\Omega_e} \in P_N(\Omega_e)\}$, where $P_N(\Omega_e)$ denotes the space of polynomials in Ω_e of degree $\leq N$. Convergence is either obtained by increasing the degree of the polynomials or by increasing the number of elements N_{el}. The basis functions φ_i are typically high-order Lagrange interpolation polynomials through the local Gauss-Lobatto integration points defined per element.

Appendix B

NEK5000

This chapter is dedicated to guide a future researcher to launch a simulation using NEK5000 spectral element code and explain the module that I have written during thesis. In order to launch a DNS of straight pipe as described in chapter 6, five files are required. They are as follows:

- .rea - Contains the control parameters and the mesh coordinates
- .usr - Contains the sub-routine to process during simulation
- .map - Consist of the mapping of spectral elements
- SIZE - Contains the information of elements per processor and polynomials
- .batch - Contains information to launch the simulation on the cluster.

B.1 .rea file

The mesh coordinate and the control parameters for running a DNS is given in this file, it can be created using `genbox` or `pretex` from Nek tools. It can also be created by Python or MATLAB. `.map` file is generated along with the `.rea` file. Parameters inside the file is denoted by the letter p. It contains a total of 118 parameters. `p002` corresponds to the kinematic viscosity, a negative value represents Reynolds number i.e $Re = 1/\nu$. The number of time steps required to run the simulation is given in parameter `p011`. The `p01` determines the number of output file to be given. Finally, `p021, p022` are used to fix tolerance level of the pressure and the velocity solvers. These are the most important parameter, for more details the reader is requested to read NEK5000 user manuals.

```
 ****** PARAMETERS *****
   2.60999990      NEKTON VERSION
   3 DIMENSIONAL RUN
         118  PARAMETERS FOLLOW
   1.00000     p001 DENSITY
-100.000     p002 VISCOS
   0.00000     p003
   0.00000     p007 RHOCP
   1.00000     p008 CONDUCT
   0.00000     p009
   0.00000     p010 FINTIME
   100.000     p011 NSTEPS
 -0.100000E-02 p012 DT
   0.00000     p013 IOCOMM
   0.00000     p014 IOTIME
   20.0000     p015 IOSTEP
   0.00000     p016 PSSOLVER: 0=default
   0.100000E-05 p021 DIVERGENCE
   0.100000E-06 p022 HELMHOLTZ
```

Information of the computational mesh is given inside the `.rea` file , which can be found beneath the parameters. In the example case given below, 32000 is the number of spectral elements, followed by the Cartesian coordinate of each element.

```
  5.00000       5.00000      -2.75000      -2.75000     XFAC,YFAC,XZERO,YZERO
**MESH DATA** 6 lines are X,Y,Z;X,Y,Z. Columns corners 1-4;5-8
  32000   3       32000           NEL,NDIM,NELV
    ELEMENT           1 [    1A]    GROUP    0
0.877686E+00  0.923880E+00  0.707107E+00  0.671752E+00
0.363549E+00  0.382683E+00  0.707107E+00  0.671752E+00
0.000000E+00  0.000000E+00  0.000000E+00  0.000000E+00
0.877686E+00  0.923880E+00  0.707107E+00  0.671752E+00
0.363549E+00  0.382683E+00  0.707107E+00  0.671752E+00
0.375000E+00  0.375000E+00  0.375000E+00  0.375000E+00
```

To restart a simulation, the parameter `PRESOLVE/RESTART OPTIONS` must be changed from `0` to `1` and the name of the file should be mentioned below.

```
      1  PRESOLVE/RESTART OPTIONS
restart0.f00001
          7          INITIAL CONDITIONS
```

B.2 .usr file

The user file consist of the all the sub-routine, that can be modified to control the boundary condition, initial conditions, mesh deformation and processing of data. Sub-routine `usrchk()` is called at every time step of the simulation, it can used to monitor the convergence as well as the total energy. The example below is written to check constant mass flow at the inlet of the pipe and also to check convergence of the simulation.

```
subroutine userchk
     include 'SIZE'
     include 'TOTAL'
     integer e,eg,f
     real chi, omega
     real residu, H1, L2, SEMI, LINF
     parameter (lt=lx1*ly1*lz1*lelt)
     common /myoutflow/ d(lx1*ly1*lz1*lelt),w1(lx1*ly1*lz1*lelt)
     common /myjunk/ vort(lt,3),w11(lt),w21(lt)

     common /RESIDU_ARRAYS/ uo(lx1,ly1,lz1,lelt),
    $     vo(lx1,ly1,lz1,lelt),
    $     wo(lx1,ly1,lz1,lelt)

     n = nx1*ny1*nz1*nelv
     wmax = glmax(vz,n)

     ubar  = 0.
     uarea = 0.
     do e=1,nelv
     do f=1,2*ndim
        if (cbc(f,e,1).eq.'v  ') then
           call surface_int(uint,aint,vz,e,f)
           ubar  = ubar  + uint
           uarea = uarea + aint
        endif
     enddo
     enddo
```

```
      ubar  = glsum(ubar ,1)
      uarea = glsum(uarea,1)
      if (uarea.gt.0) ubar = ubar/uarea

      if (nid.eq.0) write(6,1) istep,time,uarea,ubar,wmax
    1 format(i9,1p4e12.4,' ubar')


      if(istep.EQ.0) then

         call rzero(uo,n)
         call rzero(vo,n)
         call rzero(wo,n)

         if(nid.EQ.0) open(unit=10,file='residu.dat')

      elseif(istep.GE.1) then
         call opsub2(uo,vo,wo,vx,vy,vz)
         call normvc(H1,SEMI,L2,LINF,uo,vo,wo)
         residu = L2/dt
         call opcopy(uo,vo,wo,vx,vy,vz)

         if(nid.EQ.0) write(10,*) istep, residu

         if(residu.LT.1e-9) then

            call outpost(vx,vy,vz,pr,t,'CONV_')
            call exitt

         endif

      elseif(istep.EQ.nsteps) then

         close(10)
      endif
```

The `userbc` sub-routine is shown below, it was written to impose a vortex perturbation at the inlet of the pipe, along with parabolic velocity profile.

```
subroutine userbc (ix,iy,iz,iside,ieg)
      include 'SIZE'
      include 'TOTAL'
      include 'NEKUSE'
      integer e,eg

      common /mygeom/ xmin,xmax,ymin,ymax

       delta = 0.5
       xd=x/delta
       yd=y/delta
       rr=xd*xd+yd*yd

       scale = 2*(0.5/delta)**2  ! Ubar = 1 in inlet pipe (r=0.5)
       xnot = 0
       ynot = -0.3
       R = 0.25
       del = 0.5
       pos = sqrt((xd-xnot)*(xd-xnot) + (yd-ynot)*(yd-ynot))
```

```
        if (pos.le.R/2) then
               omega = 1
        else if (pos.gt.R/2 .and. pos.le.R) then
               omega  =  2 * (R - pos)/R
        else
               omega = 0
        endif

        ux= del * omega * (-(yd-ynot))
        uy= del * omega * (xd-xnot)
        uz= scale*(1-rr)

        temp=0.0

        return
       end
```

The `setobj` subroutine is return to find the wall node points inside the computational domain to compute drag.

```
      subroutine set_obj  ! define objects for surface integrals

       include 'SIZE'
       include 'TOTAL'

       common /mygeom/ xmin,xmax,ymin,ymax

       integer e,f

c      Define new objects

       nobj = 1          ! for Periodic
       iobj = 0
       do ii=nhis+1,nhis+nobj
          iobj = iobj+1
          hcode(10,ii) = 'I'
          hcode( 1,ii) = 'F' ! 'F'
          hcode( 2,ii) = 'F' ! 'F'
          hcode( 3,ii) = 'F' ! 'F'
          lochis(1,ii) = iobj
       enddo
       nhis = nhis + nobj

       if (maxobj.lt.nobj) write(6,*) 'increase maxobj in SIZEu. rm *.o'
       if (maxobj.lt.nobj) call exitt

       nxyz = nx1*ny1*nz1*nelt

       do e=1,nxyz
       do f=1,2*ndim

          z = zm1(e,1,1,1)
          if (cbc(f,e,1).eq.'W  ' .and. z.gt.0) then
             iobj = 1

             if (iobj.gt.0) then
                nmember(iobj) = nmember(iobj) + 1
                mem = nmember(iobj)
```

```
               ieg = lglel(e)
               object(iobj,mem,1) = ieg
               object(iobj,mem,2) = f
               write(6,1) iobj,mem,f,ieg,e,nid,' OBJ'
    1          format(6i9,a4)
            endif

         endif
       enddo
       enddo

       return
       end
```

B.3 SIZE file

Parameters like polynomial order, elements per processors, number of objects inside the computational domain are controlled by this parameter.

```
       parameter (ldim=3)
       parameter (lx1=5,ly1=lx1,lz1=lx1,lelt=2000,lelv=lelt)
       parameter (lxd=8,lyd=lxd,lzd=lxd)
       parameter (lelx=1,lely=1,lelz=1)
       parameter (lzl=3 + 2*(ldim-3))
```

`ldim` is the dimension of the Navier-Stokes equation. `lx1` and `lxd` are the controls the polynomial order of the approximation and polynomial order of the integration for convective terms respectively. `lelt` determines the number element per processor.

B.4 launching a simulation

B.4.1 Step 1:

In order to launch a simulation, First change the parameters in the `Pipe.rea`, `Pipe.usr` and in the SIZE file accordingly, Copy the `makenek` file from the `neksvn` installation folder.

B.4.2 Step 2:

A `nek5000` file should be created. In the folder where `Pipe.rea` `Pipe.usr` `Pipe.map` and `SIZE` exists, executing the following command:

```
>> Module load openmpi    % only on CRIHAN
>> ./makenek Pipe
```

B.4.3 Step 3:

A `SESSION.NAME` file should be created for the code to access the working directory and the name of the file. It can be created executing the command:

```
>> echo Pipe        >  SESSION.NAME
>> echo `pwd``/' >>  SESSION.NAME
```

B.4.4 Step 4:

To launch the simulation on CRIHAN super computer facility, a batch file is created by the following shell script:

```
#!/bin/bash
#
# Job name
# @ job_name = ompi.run
# Batch output file
# @ output =  $(job_name).o$(jobid)
# Batch error file
# @ error  =  $(job_name).e$(jobid)

# Job type
# @ job_type = MPICH

# Job time (hh:mm:ss)
# @ wall_clock_limit = 24:00:00

# ---------------------
# MPI tasks number
# @ total_tasks = 1000

# MPI task maximum memory (mb, gb)
# @ data_limit = 3gb
# ----------------------
echo `pwd``/` > CURREN_DIR

# Input files directory
# @ cri_initialdir = /home/2015005/kselva02/pipes/pipe_5000
# Output files directory
# @ cri_finaldir = /home/2015005/kselva02/pipes/pipe_5000

# @ notification = complete
# User e-mail address
# @ notify_user = kamal.selvam@etu.univ-lehavre.fr
# @ queue

cd $LOCAL_WORK_DIR
touch Pipe.rea
rm -f logfile
rm -f ioinfo
mv Pipe.log.1000 Pipe.log1.1000
mv Pipe.sch Pipe.sch1
# User commands

# MPI code execution (binary linked with Open MPI)
mpirun.Ompi /home/2015005/kselva02/pipes/pipe_5000/nek5000 > lpipe.log

# Move output files to $LOCAL_SPOOL_DIR
# (before automatic copy to cri_finaldir)
mv *.res *.dat *.log *.f* *.out $LOCAL_SPOOL_DIR
```

Time for execution of the simulation can be modified in `wall_clock_limit` and the number of cores to run the simulation in `total_tasks`. The path of the folder should also be changed respectively. Save the file as `Pipe_run.batch`

B.4.5 Step 5:

Finally to launch the simulation on CRIHAN, the following command should be executed:

```
>> llsubmit Pipe_run.batch
```

To view the status of the simulation:

```
>> llq -u [username]
```

B.4.6 Step 6:

To visualise the simulated data, an open source data software called `VIsit` is used. To open a series of output files, a metadata file is needed. A sample metadata file is shown below called `Vis.nek5000`

```
NEK5000
version: 1.0
filetemplate: pipe%01d.f%05d
firsttimestep: 1
numtimesteps: 20
```

Bibliography

[1] O. Reynolds. An experimental investigation of the circumstances which determine whether the motion of water shall be direct or sinuous, and of the law of resistance in parallel channels. *Proc. roy. soc. lond.*, 35(224-226):84–99, 1883 (cited on pages 15, 71).

[2] W. Pfenninger. Boundary layer suction experiments with laminar flow at high reynolds numbers in the inlet length of a tube by various suction methods. In *Boundary layer and flow control*. G. V. Lachman, editor. Pergamon, 1961, pages 961–980 (cited on pages 17, 71).

[3] D. Barkley, B. Song, V. Mukund, G. Lemoult, M. Avila, and B. Hof. The rise of fully turbulent flow. *Nature*, 526(7574):550–553, 2015 (cited on pages 17, 57, 63, 65).

[4] Y. Duguet, A. P. Willis, and R. R. Kerswell. Slug genesis in cylindrical pipe flow. *J. fluid mech.*, 663:180–208, 2010 (cited on pages 18, 57, 65).

[5] I. J. Wygnanski and F. H. Champagne. On transition in a pipe. Part 1. The origin of puffs and slugs and the flow in a turbulent slug. *J. fluid mech.*, 59:281–335, 1973 (cited on pages 18, 19, 52, 57, 63, 71, 72).

[6] A. P. Willis and R. R. Kerswell. Coherent structures in localized and global pipe turbulence. *Phys. rev. lett.*, 100(124501), 2008 (cited on pages 18, 52, 57, 65).

[7] David Moxey and Dwight Barkley. Distinct large-scale turbulent-laminar states in transitional pipe flow. *Pnas*, 107(18):8091–8096, 2010 (cited on pages 18, 19, 57, 65).

[8] K. Avila, D. Moxey, A. de Lozar, M. Avila, D. Barkley, and B. Hof. The onset of turbulence in pipe flow. *Science*, 333(6039):192–196, 2011 (cited on pages 18, 19, 50, 57, 63, 65).

[9] M. Shimizu, P. Manneville, Y. Duguet, and G. Kawahara. Splitting of a turbulent puff in pipe flow. *Fluid dyn. res.*, 46(6):061403, 2014 (cited on pages 18, 50, 57, 65).

[10] J Nikuradse. Strömungsgesetze in rauen rohren. Technical report (361). VDI Forschungsheft, 1933 (cited on pages 19, 73).

[11] M. V. Zagarola and A. J. Smits. Mean-flow scaling of turbulent pipe flow. *J. fluid mech.*, 373:33–79, 1998 (cited on pages 19, 71, 74).

[12] F. Durst, S. Ray, B. Ünsal, and O. A. Bayoumi. The development lengths of laminar pipe and channel flows. *J. fluid eng.*, 127(6):1154–1160, 2005 (cited on pages 19, 71, 72).

[13] F. Durst and B. Ünsal. Forced laminar-to-turbulent transition of pipe flows. *J. fluid mech.*, 560:449–464, 2006 (cited on pages 19, 71).

[14] E.-S. Zanoun, M. Kito, and C. Egbers. A study on flow transition and development in circular and rectangular ducts. *J. fluid eng.*, 131(6):061204, 2009 (cited on pages 19, 71–74, 77).

[15] Xiaohua Wu, Parviz Moin, Ronald J Adrian, and Jon R Baltzer. Osborne reynolds pipe flow: direct simulation from laminar through gradual transition to fully developed turbulence. *Pnas*, 112(26):7920–7924, 2015 (cited on pages 19, 24, 54, 63, 65, 71, 74, 77).

[16] D. J. Latornell and A. Pollard. Some observations on the evolution of shear layer instabilities in laminar flow through axisymmetric sudden expansions. *Phys. fluids*, 29(9):2828–2835, 1986 (cited on pages 20, 43, 46, 53).

[17] K. R. Sreenivasan. Laminarescent, relaminarizing and retransitional flows. *Acta mec.*, 44(1-2):1–48, 1982 (cited on pages 20, 50).

[18] R. M. Fearn, T. Mullin, and K. A. Cliffe. Nonlinear flow phenomena in a symmetric sudden expansion. *J. fluid mech.*, 211:595–608, 1990 (cited on pages 20, 25, 31).

[19] T. Mullin, J. R. T. Seddon, M. D. Mantle, and A. J. Sederman. Bifurcation phenomena in the flow through a sudden expansion in a circular pipe. *Phys. fluids*, 21:014110, 2009 (cited on pages 20, 21, 23, 43, 46, 48, 52, 53).

[20] C. D. Cantwell, D. Barkley, and H. M. Blackburn. Transient growth analysis of flow through a sudden expansion in a circular pipe. *Phys. fluids*, 22(3):034101, 2010 (cited on pages 20, 21, 33, 46, 53, 56, 57).

[21] E Sanmiguel-Rojas, C Del Pino, and C Gutiérrez-Montes. Global mode analysis of a pipe flow through a 1:2 axisymmetric sudden expansion. *Phys. fluids*, 22(7):071702, 2010 (cited on pages 21, 43, 46, 49, 53, 54, 56, 57).

[22] E. Sanmiguel-Rojas and T. Mullin. Finite-amplitude solutions in flow through a sudden expansion in a circular pipe. *J. fluid mech.*, 691:201–213, 2012 (cited on pages 21, 22, 43, 49, 53).

[23] J. Peixinho and H. Besnard. Transition to turbulence in slowly divergent pipe flow. *Phys. fluids*, 25:111702, 2013 (cited on pages 21, 22, 46, 50, 52, 53).

[24] T. Mullin, S. Shipton, and S. J. Tavener. Flow in a symmetric channel with an expanded section. *Fluid dyn. res.*, 33(5-6):433, 2003 (cited on page 25).

[25] D. Drikakis. Bifurcation phenomena in incompressible sudden expansion flows. *Phys.fluids*, 9(1):76–87, 1997 (cited on page 25).

[26] Gayathri Swaminathan, Kirti Chandra Sahu, A. Sameen, and Rama Govindarajan. Global instabilities in diverging channel flows. *Theoretical and computational fluid dynamics*, 25(1):53–64, 2011 (cited on page 25).

[27] Mamta Jotkar, José Miguel Pérez, Vassilis Theofilis, and Rama Govindarajan. Instability mechanisms in straight-diverging-straight channels. *Procedia iutam*, 14:236–245, 2015 (cited on pages 25, 31).

[28] Flavio Giannetti and Paolo Luchini. Structural sensitivity of the first instability of the cylinder wake. *J. fluid mech.*, 581:167–197, 2007 (cited on pages 25, 28, 29).

[29] A. Fani, S. Camarri, and M. V. Salvetti. Stability analysis and control of the flow in a symmetric channel with a sudden expansion. *Phys. fluids*, 24(8), 2012 (cited on pages 25, 31, 33).

[30] P Assemat, D. Fabre, and J. Magnaudet. The onset of unsteadiness of two-dimensional bodies falling or rising freely in a viscous fluid: a linear study. *J. fluid mech.*, 690(173–202), 2012 (cited on page 29).

[31] S. Mittal and A Verma. A new unstable mode in the wake of a circular cylinder. *Phys. fluids*, 23:173–202, 2012 (cited on page 29).

[32] O. Marquet, D. Sipp, J.-M. Chomaz, and L. Jacquin. Amplifier and resonator dynamics of a low-Reynolds-number recirculation bubble in a global framework. *J. fluid mech.*, 605:429–443, 2008 (cited on pages 33, 49).

[33] D. Lanzerstorfer and H. C. Kuhlmann. Global stability of multiple solutions in plane sudden-expansion flow. *J. fluid mech.*, 702:378–402, 2012 (cited on page 33).

[34] Anthony T Patera. A spectral element method for fluid dynamics: laminar flow in a channel expansion. *Journal of computational physics*, 54(3):468–488, 1984. ISSN: 0021-9991 (cited on pages 35, 90).

[35] J. W. Lottes P. F. FischerF. Fischer and S. G. Kerkemeier. nek5000 Web page. http://nek5000.mcs.anl.gov. 2008 (cited on pages 35, 41).

[36] M.O. Deville, P.F. Fischer, and E.H. Mund. *High-order methods for incompressible fluid flow*. Of *Cambridge Monographs on Applied and Computational Mathematics*. Cambridge University Press, 2002. ISBN: 9780521453097 (cited on pages 38, 87, 88).

[37] C. Canuto, M.Y. Hussaini, A. Quarteroni, and T.A. Zang. *Spectral methods: fundamentals in single domains*. Of *Scientific Computation*. Springer Berlin Heidelberg, 2007. ISBN: 9783540307266 (cited on pages 38, 87, 88).

[38] K. R. Sreenivasan and P. J. Strykowski. An instability associated with a sudden expansion in a pipe flow. *Phys. fluids*, 26(10):2766–2768, 1983 (cited on pages 43, 46, 48, 49, 52, 53).

[39] K. J. Hammad, M. V. Ötügen, and E. B. Arik. A PIV study of the laminar axisymmetric sudden expansion flow. *Exp. fluids*, 26(3):266–272, 1999 (cited on pages 43, 46, 53).

[40] P. Fischer, J. Kruse, J. Mullen, H. Tufo, J. Lottes, and S. Kerkemeier. Nek5000: Open source spectral element CFD solver. *Http://nek5000.mcs.anl.gov*, 2008 (cited on page 45).

[41] D. Fabre, F. Auguste, and J. Magnaudet. Bifurcations and symmetry breaking in the wake of axisymmetric bodies. *Phys. fluids*, 20(5):051702, 2008 (cited on page 49).

[42] T. Bobinski, S. Goujon-Durand, and J. E. Wesfreid. Instabilities in the wake of a circular disk. *Phys. rev. e*, 89:053021, 5, 2014 (cited on pages 49, 53).

[43] U. Ehrenstein and F. Gallaire. Global low-frequency oscillations in a separating boundary-layer flow. English. *J. fluid mech.* IUTAM Bookseries 14:123–133, 2009. Marianna Braza and Kerry Hourigan, editors (cited on page 49).

[44] M. Sibulkin. Transition from turbulent to laminar pipe flow. *Phys. fluids*, 5(3):280–284, 1962 (cited on page 50).

[45] M. Shimizu and S. Kida. A driving mechanism of a turbulent puff in pipe flow. *Fluid dyn. res.*, 41(4):045501, 2009 (cited on pages 52, 65).

[46] Sonu S Varghese, Steven H Frankel, and Paul F Fischer. Direct numerical simulation of stenotic flows. part 1. steady flow. *J. fluid mech.*, 582:253–280, 2007 (cited on page 53).

[47] K. Selvam, J. Peixinho, and A. P. Willis. Localised turbulence in a circular pipe flow with gradual expansion. *J. fluid mech.*, 771:R2, 2015 (cited on pages 53, 54, 56, 57).

[48] Yohann Duguet. Pipe flow clogged with turbulence. *J. fluid mech.*, 776:1–4, 2015 (cited on page 53).

[49] E. Sanmiguel-Rojas, M. A. Burgos, C. Del Pino, and R. Fernandez-Feria. Three-dimensional structure of confined swirling jets at moderately large reynolds numbers. *Phys. fluids*, 20(4):044104, 2008 (cited on page 53).

[50] A Miranda-Barea, B Martìnez-Arias, L Parras, M. A. Burgos, and C del Pino. Experimental study of rotating hagen-poiseuille flow discharging into a 1: 8 sudden expansion. *Phys. fluids*, 27(3):034104, 2015 (cited on page 53).

[51] A. G. Darbyshire and T. Mullin. Transition to turbulence in constant-mass-flux pipe flow. *J. fluid mech.*, 289:83–114, 1995 (cited on page 54).

[52] J. Peixinho and T. Mullin. Finite-amplitude thresholds for transition in pipe flow. *J. fluid mech.*, 582:169–178, 2007 (cited on pages 54, 71).

[53] M. Nishi, B. Unsal, F. Durst, and G. Biswas. Laminar-to-turbulent transition of pipe flows through puffs and slugs. *J. fluid mech.*, 614:425–446, 2008 (cited on pages 54, 57, 71, 72).

[54] T. Mullin. Experimental studies of transition to turbulence in a pipe. *Annu. rev. fluid mech.*, 43:1–24, 2011 (cited on pages 54, 71).

[55] Fernando Mellibovsky and Alvaro Meseguer. Pipe flow transition threshold following localized impulsive perturbations. *Phys. fluids*, 19(4):044102, 2007 (cited on page 54).

[56] Per-Olov Åsén, Gunilla Kreiss, and Dietmar Rempfer. Direct numerical simulations of localized disturbances in pipe poiseuille flow. *Computers & fluids*, 39(6):926–935, 2010 (cited on page 54).

[57] Jean-Christophe Loiseau. Analyse de la stabilité globale et de la dynamique d'écoulements tridimensionnels. PhD thesis. ENSAM, Paris, 2014 (cited on page 54).

[58] Björn Hof, Alberto de Lozar, Marc Avila, Xiaoyun Tu, and Tobias M Schneider. Eliminating turbulence in spatially intermittent flows. *Science*, 327(5972):1491–1494, 2010 (cited on pages 57, 63).

[59] J. L. Lumley. The structure of inhomogeneous turbulent flows. *Atm. turb. and radio wave. prop., ed by am yaglom and vi tatarsky (nauka, moscow)*:166–178, 1967 (cited on page 59).

[60] Bernd R. Noack, Konstantin Afansiev, Marek Morzynski, Giled Tadmor, and Frank Thiele. A hierarchy of low-dimensional models for the transient and post-transient cylinder wake. *J. fluid mech.*, 497:335–363, December 2003. ISSN: 1469-7645 (cited on page 59).

[61] L. Sirovich. Turbulence and the dynamics of coherent structures. part i: coherent structures. part ii: symmetries and transformations. part iii: dynamics and scaling. *Quart. appl. math.*, 45:561–590, 1987 (cited on page 59).

[62] Knud Erik Meyer, Jakob M. Pedersen, and Oktay Ozcan. A turbulent jet in crossflow analysed with proper orthogonal decomposition. *J. fluid mech.*, 583:199–227, July 2007. ISSN: 1469-7645 (cited on page 59).

[63] Ashley P. Willis and Rich R. Kerswell. Turbulent dynamics of pipe flow captured in a reduced model: puff relaminarization and localized 'edge' states. *J. fluid mech.*, 619:213–233, 2009 (cited on page 65).

[64] F.T. Pinho and J.H. Whitelaw. Flow of non-newtonian fluids in a pipe. *J. of non-newtonian fluid mech.*, 34(2):129–144, 1990. ISSN: 0377-0257 (cited on page 67).

[65] T. Tatsumi. Stability of the laminar inlet-flow prior to the formation of Poiseuille regime, II. *J. phys. soc. jpn.*, 7(5):495–502, 1952 (cited on page 71).

[66] E. B. Christiansen and H. E. Lemmon. Entrance region flow. *Aiche j.*, 11(6):995–999, 1965 (cited on page 71).

[67] L. M. Huang and T. S. Chen. Stability of developing pipe flow subjected to non-axisymmetric disturbances. *J. fluid mech.*, 63(01):183–193, 1974 (cited on page 71).

[68] T. Sarpkaya. A note on the stability of developing laminar pipe flow subjected to axisymmetric and non-axisymmetric disturbances. *J. fluid mech.*, 68(2):345–351, 1975 (cited on page 71).

[69] S. C. Gupta and V. K. Garg. Effect of velocity distribution on the stability of developing flow in a pipe. *Phys. fluids*, 24(4):576–578, 1981 (cited on page 71).

[70] D. F. Da Silva and E. A. Moss. The stability of pipe entrance flows subjected to axisymmetric disturbances. *J. fluid eng.*, 116(1):61–65, 1994 (cited on page 71).

[71] P. W. Duck. Transient growth in developing plane and Hagen-Poiseuille flow. In *Proc. r. soc. lond. a.* Volume 461. (2057), 2005, pages 1311–1333 (cited on page 71).

[72] K. C. Sahu and R. Govindarajan. Linear instability of entry flow in a pipe. *J. fluid eng.*, 129(10):1277–1280, 2007 (cited on page 71).

[73] V. W. Ekman. On the change from steady to turbulent motion of liquids. *Ark. mat. astron. phy.*, 6:1–16, 1910 (cited on page 71).

[74] R. Comolet. Recherche sur la genèse de la turbulence dans les conduites en charge. PhD thesis. Publ. Sci. Tech. Minist. Air, Paris, 1950 (cited on page 71).

[75] E. R. Lindgren. The transition process and other phenomena in viscous flow. *Arkiv fysik*, 12, 1957 (cited on page 71).

[76] A. A. Draad, G. D. C. Kuiken, and F. T. M. Nieuwstadt. Laminar–turbulent transition in pipe flow for Newtonian and non-Newtonian fluids. *J. fluid mech.*, 377:267–312, 1998 (cited on page 71).

[77] F. König, E.-S. Zanoun, E. Öngüner, and C. Egbers. The CoLaPipe—The new Cottbus large pipe test facility at Brandenburg University of Technology Cottbus-Senftenberg. *Rev. sci. instrum.*, 85(7):075115, 2014 (cited on page 72).

[78] F. König. Investigations of high Reynolds number pipe flow. PhD thesis. Brandenburgischen Technischen Universität Cottbus-Senftenberg, 2015 (cited on page 72).

[79] J. Laufer. The structure of turbulence in fully developed pipe flow. Technical report (1174). NACA, 1954 (cited on page 72).

[80] A. E. Perry and C. J. Abell. Scaling laws for pipe-flow turbulence. *J. fluid mech.*, 67(02):257–271, 1975 (cited on page 72).

[81] R. Shaw. The influence of hole dimensions on static pressure measurements. *J. fluid mech.*, 7(04):550–564, 1960 (cited on page 73).

[82] B. J. McKeon and A. J. Smits. Static pressure correction in high Reynolds number fully developed turbulent pipe flow. *Meas. sci. technol.*, 13(10):1608, 2002 (cited on page 73).

[83] Y. Tsuji, J. H. M. Fransson, P. H. Alfredsson, and A. V. Johansson. Pressure statistics and their scaling in high-Reynolds-number turbulent boundary layers. *J. fluid mech.*, 585:1–40, 2007 (cited on pages 73, 74, 77).

[84] H. Blasius. Boundary layer in fluids with little friction. *Zeitschrift für mathematik und physik*, 56:1–37, 1908 (cited on page 74).

[85] A. Pollard, A. M. Savill, and H. Thomann. Turbulent pipe flow manipulation: some experimental and computational results for single manipulator rings. *Applied scientific research*, 46(3):281–290, 1989 (cited on page 77).

[86] P. Schlatter and R. Örlü. Turbulent boundary layers at moderate Reynolds numbers: inflow length and tripping effects. *J. fluid mech.*, 710:5–34, 2012 (cited on page 77).

[87] Y. Naka, M. Stanislas, J.-M. Foucaut, S. Coudert, J.-P. Laval, and S. Obi. Space–time pressure–velocity correlations in a turbulent boundary layer. *J. fluid mech.*, 771:624–675, 2015 (cited on page 77).

[88] J. M. Clinch. Measurements of the wall pressure field at the surface of a smooth-walled pipe containing turbulent water flow. *J. sound vib.*, 9(3):398–419, 1969 (cited on page 77).

[89] T. M. Farabee and M. J. Casarella. Spectral features of wall pressure fluctuations beneath turbulent boundary layers. *Phys. fluids*, 3(10):2410–2420, 1991 (cited on page 77).

[90] N. K. Agarwal. The sound field in fully developed turbulent pipe flow due to internal flow separation, part i: wall-pressure fluctuations. *J. sound vib.*, 169(1):89–109, 1994 (cited on page 77).

[91] L. W. B. Browne and A. Dinkelacker. Turbulent pipe flow: pressures and velocities. *Fluid dyn. res.*, 15(3):177–204, 1995 (cited on page 77).

[92] C. Durant, G. Robert, P. J. T. Filippi, and P.-O. Mattei. Vibroacoustic response of a thin cylindrical shell excited by a turbulent internal flow: comparison between numerical prediction and experimentation. *J. sound vib.*, 229(5):1115–1155, 2000 (cited on page 77).

[93] A. O. Borisyuk. Experimental study of wall pressure fluctuations in rigid and elastic pipes behind an axisymmetric narrowing. *J. fluids struct.*, 26(4):658–674, 2010 (cited on page 77).

[94] F.N. van de Vosse and P.D. Minev. *Spectral element methods: theory and applications*. Eindhoven University of Technology, Faculty of Mechanical Engineering, 1996. ISBN: 9789038603186 (cited on pages 86, 87).

Abstract

This thesis deals with numerical and experimental investigations of flow through circular pipes with smaller inlet and larger outlet diameter, also known as expansion pipes. The hydrodynamic expansion pipe flow is globally stable for high Reynolds number. In order to numerically simulate these type of flows, large computational domains that could accommodate the linearly growing symmetric recirculation region is needed. This in turn increases the computational cost. Moreover, experimental studies of expansion pipe flows indicate that the transition occurs at lower Reynolds number than predicted by the linear stability theory. The reason for early transition is due to the presence of imperfections in the experimental setup, that acts as a finite-amplitude perturbation of the flow. Three dimensional direct numerical simulations of the Navier-Stokes equations with two different types of perturbations (i) the tilt and (ii) the vortex are investigated. First, the tilt perturbation, which applied at the inlet, creates an asymmetric recirculation region and then breaks to form localised turbulence downstream the expansion section. Second, the vortex perturbation, which satisfies the continuity boundary condition at the wall, creates structures that looks like lower order azimuthal mode, resembles an optimally amplified perturbation. It grows due to convective instability mechanism and then breaks to form localised turbulence. Spatial correlation and the proper orthogonal decomposition reveal that this localised turbulence gains it energy from the core flow coming out of the inlet pipe. Applying vortex perturbation to straight pipe flow also triggers turbulence. Additional measurements and simulations on the development length of the fully developed turbulence reveals that the fluctuations become statistically invariant after a critical axial position. The pressure fluctuations grow exponentially and then saturates, indicating the region of fully developed turbulent pipe flow.

Keywords: Transition to turbulence, pipe flow, expansion flow, localised turbulence, fully developed turbulence, pressure measurements

Resumé

Cette thèse traite de recherches numériques et expérimentales sur l'écoulement à traves des conduites circulaires ou des tubes avec une petite entrée et un diamètre de sortie plus grand, parfois appelées élargissement ou divergents. L'écoulement dans un élargissement est globalement stable pour des nombres de Reynolds élevés. Ainsi la simulation numérique de ce type d'écoulement nécessite de grands domaines de calcul contenant la zone de recirculation, qui croît linéairement. En outre, les études expérimentales dans les élargissements brusques indiquent que la transition se produit à des nombres de Reynolds plus faibles que prévue par la théorie linéaire de stabilité. La raison pour cette transition précoce est due à la présence d'imperfections dans le dispositif expérimental, qui agit comme une perturbation d'amplitude finie de l'écoulement. Des simulations numériques directes des équations de Navier-Stokes ont été réalisés avec deux types différents de perturbations (i) l'inclinations et (ii) le vortex. Tout d'abord, la perturbation de type inclinaison, qui est appliqué à l'entrée, crée une zone de recirculation asymétrique, puis se casse pour former une turbulence localisée en aval de l'expansion. Deuxièmement, la perturbation de type vortex, qui satisfait la condition de continuité à la paroi, crée des structures qui ressemblent à un mode azimutal d'ordre inférieur, déjà identifié comme une perturbation optimale amplifiée. Il croît en raison de l'instabilité convective, puis forme une tâche de turbulence localisée. Enfin, la corrélation spatiale et la décomposition en modes propres révèlent que cette turbulence localisée obtient son énergie de l'écoulement d'entrée. La perturbation vortex déclenche également la turbulence dans des conduites de section constante. Des mesures et des simulations supplémentaires sur la longueur de développement de la turbulence développée révèlent que les variations des propriétés de l'écoulement (vitesse er pression) deviennent statistiquement invariantes après une position axiale critique. Les fluctuations de pression se développent de façon exponentielle puis saturent, indiquant la région d'écoulement turbulent pleinement développé.

Mots clés: Transition à la turbulence, écoulement dans une conduite, écoulement dans une élargissement, turbulence localisée, turbulence développée, des mesures de pression